University of Texas at El Paso
DigitalCommons@UTEP

Open Access Theses & Dissertations

2014-01-01

# Effect Of Rhenium On Short Term Oxidation Of Niobium Based Alloys For High Temperature Applications

Ruth M. Sierra
*University of Texas at El Paso*, rmdasary@miners.utep.edu

Follow this and additional works at: https://digitalcommons.utep.edu/open_etd

 Part of the Materials Science and Engineering Commons, and the Mechanics of Materials Commons

Recommended Citation
Sierra, Ruth M., "Effect Of Rhenium On Short Term Oxidation Of Niobium Based Alloys For High Temperature Applications" (2014). *Open Access Theses & Dissertations*. 1350.
https://digitalcommons.utep.edu/open_etd/1350

This is brought to you for free and open access by DigitalCommons@UTEP. It has been accepted for inclusion in Open Access Theses & Dissertations by an authorized administrator of DigitalCommons@UTEP. For more information, please contact lweber@utep.edu.

# EFFECT OF RHENIUM ON SHORT TERM OXIDATION OF NIOBIUM BASED ALLOYS FOR HIGH TEMPERATURE APPLICATIONS

RUTH M. SIERRA

Materials Science and Engineering

APPROVED:

Shailendra K. Varma, Ph.D., Chair

Lawrence E. Murr, Ph.D.

Felicia S. Manciu, Ph.D.

Russell R. Chianelli, Ph.D.

Bess Sirmon-Taylor, Ph.D.
Interm Dean of the Graduate School

Copyright ©

by

Ruth M. Sierra

2014

# Dedication

## To God, Almighty

**“I CAN DO ALL THINGS THROUGH HIM WHO STRENGTHENS ME”**

**PHILIPPIANS 4:13**

# EFFECT OF RHENIUM ON SHORT TERM OXIDATION OF NIOBIUM BASED ALLOYS FOR HIGH TEMPERATURE APPLICATIONS

by

RUTH M. SIERRA, B.Tech, M.Phil.

DISSERTATION

Presented to the Faculty of the Graduate School of

The University of Texas at El Paso

in Partial Fulfillment

of the Requirements

for the Degree of

DOCTOR OF PHILOSOPHY

Materials Science and Engineering

THE UNIVERSITY OF TEXAS AT EL PASO

May 2014

## Acknowledgements

I would like to acknowledge the guidance and support the faculty of the Materials and Science Engineering program has provided me while I pursed my degree at UTEP. I would also like to acknowledge the financial support of the Office of Naval Research through the grant number N00014-08-1-0506 and Dr. Todd Leonhardt, Rhenium Alloys Inc. for providing us with Rhenium for our initial study.

I am also grateful for the support my family has rendered throughout the period of my education in the Unites States, without which I would not have known this day.

## Abstract

The effect of adding Re to Nb-based alloys and is intended to analyze in depth the microstructures of Nb based alloys with Re, Si and Cr additions, in atomic percentages. The binary alloys (Nb-5Re, Nb-5Si and Nb-5Cr) reveal the formation of a single phase, $Nb_{SS,}$ $Nb_{SS}$+ $Nb_3Si$ and $Nb_{SS}$+$NbCr_2$ respectively. The formation of the single phase was confirmed by TEM studies for the Nb-5Re alloy. Addition of Re to form ternary alloys, has helped in the formation of $Nb_5Si_3$ and (Nb, Re) $Cr_{2,}$ in Nb-5Re-5Si and Nb-5Re-5Cr respectively. Quaternary alloy Nb-5Re-5Si-5Cr has $Nb_5Si_3$, $NbCr_2$ and $Nb_{SS}$. The oxidation behavior has been studied and the formation of the oxides has been characterized using XRD, SEM, EDS.

Nb-Re-Si-Cr–X (Al, B, W) alloy system has been examined at temperatures between 700 and 1400°C in air. The continued work was to develop and discover a new materials system capable of replacing nickel based super alloys. Additions of aluminum were found to provide limited oxidation resistance. A discontinuous layer of $Al_2O_3$ and $SiO_2$ was observed to form at all temperatures adapted for this study. Alloy containing aluminum additions were observed to suffer from pest oxidation at intermediate temperatures due to the development of $Nb_2O_5$. Poor oxidation resistance at intermediate temperatures for alloys with aluminum additions was attributed to a transformation in the structure of $Nb_2O_5$ formed. Pesting was observed at 900oC, consuming the metal completely. Additions of chromium were observed to increase oxidation resistance through the development of a layered oxide structure containing $SiO_2$ and $CrNbO_4$. Internal oxidation layer was observed to develop oxides in the midst of the phases formed.

Boron addition has helped in the formation of the 3, 5 silicides, $Nb_{SS}$, and Laves phase. The combination of oxides of $Nb_2O_5$, $CrNbO_4$ and $SiO_2$ has helped improve the oxidation resistance of the alloy. Rhenium in this alloy has been a major element in terms of forming Re-oxides which has resulted in the negative weight gain. Alloys with this type of weight gain is advantageous as it refers to nullifying

the formation of bulky $Nb_2O_5$. There was no metal left at 1400oC. Pesting was no observed at low temperature range. However, spalling was noticed at 1200 and 1300$^o$C.

Tungsten additions have helped in the formation of $Nb_5Si_3$, $Cr_2Re_3$, $NbCr_2$, and $Nb_{SS}$. All the phases formed were intermetallics, except the solid solution. These high temperature phases have helped to resist oxidation to an extent. The formation of a $CrNbO_4$ and $SiO_2$ has helped in lowering the oxidation kinetics. No pesting was observed, spalling of the oxide was noticed only at 1300$^o$C. Oxidation behavior of these alloys were characterized by the weight change per unit surface area method. Oxidation products were characterized by x-ray diffraction and scanning electron microscopy in several modes including backscatter imaging, secondary imaging, energy dispersive x-ray spectroscopy, and x-ray mapping.

## Table of Contents

## List of Figures

## List of Tables

# Chapter 1- Introduction

Discovering and developing materials systems capable of offering high strength and stiffness at the highest temperatures possible has always been a fundamental concern of the materials science community. Specifically in the aerospace industry in which current nickel based super alloys are operating within 200°C of their melting points. This has been made possible by advances in both process and design technologies. Such advances have led to the development of internally cooled single crystal components within turbines which are protected by advanced ceramic thermal barrier coatings [1]. A trend can be observed in the contributions each development has made in terms of power produced and turbine rotor inlet temperature as shown in Figure 1.1 [2]. Turbine rotor inlet temperature is the hottest part of the turbine where combustion occurs. A few initial observations can be made from Figure 1.1 which indicate that despite an increase in turbine rotor inlet temperature the amount of specific core power increased deviates farther from the ideal gas-turbine engine relationship leading to lower efficiency, hence the need for advanced high temperature materials systems.

There are many constraints that guide the search for new materials such as melting point, cost, and density to list a few. However, two prevalent approaches can be observed in the studies conducted in the search for these high temperature materials that involve developing either high temperature creep resistance and other related mechanical properties or high temperature oxidation resistance. The latter of which is very important in developing alloys from niobium and molybdenum. Systems that incorporate these two metals potentially represent the next generation of high temperature materials given their high melting points and comparable density

to nickel. Unfortunately like most of other refractory metals niobium suffers from catastrophic oxidation at elevated temperatures. Molybdenum also suffers from catastrophic oxidation. However, volatilization of oxides also leads to mass loss issues.

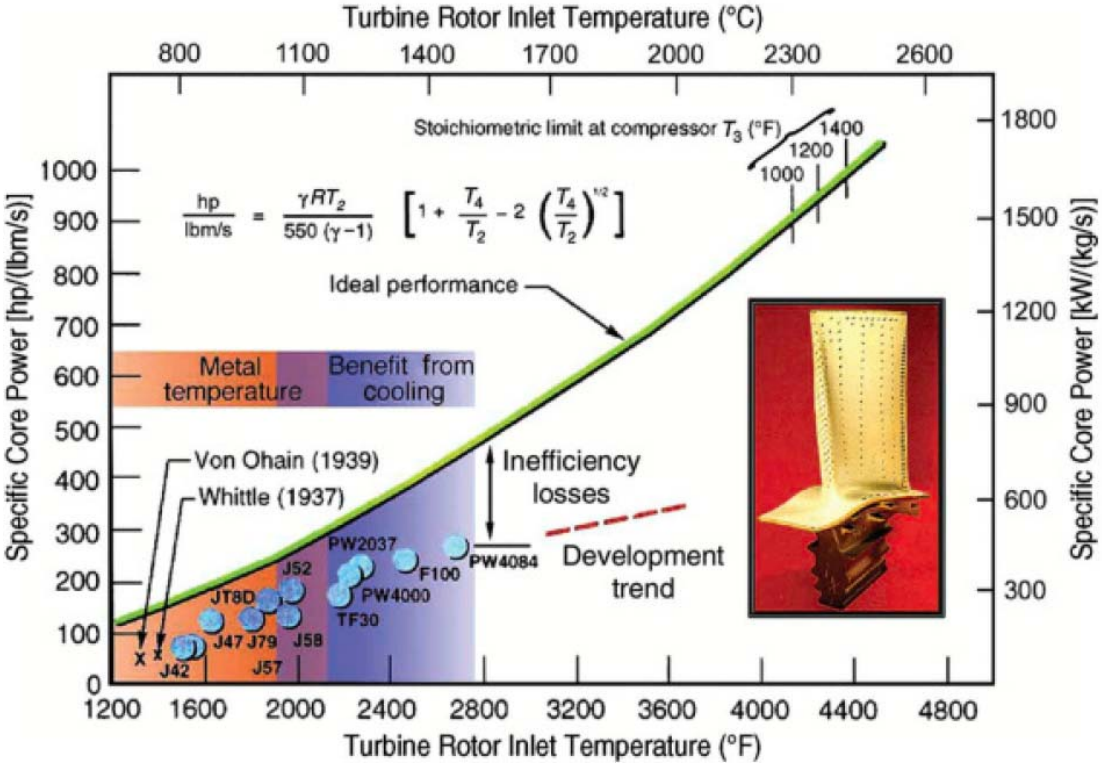


Figure 1.1 Specific power as a function of temperature. Ideal gas-turbine relationship T2- turbine rotor inlet temperature, T4-turbine exhaust gas temperature, and T-3 represents stoichiometric temperatures, adopted from [2]

Other requirements that need to be satisfied include high melting points, comparable density to that of nickel, and several mechanical properties such as creep resistance and fracture toughness at ambient temperature. Niobium based refractory metal matrix composites are prime candidates to fill this need due to their comparable density to nickel alloys (density of Ni = 8.912g/cm3 and Nb = 8.57g/cm3) and high melting points [3]. However niobium based alloys typically suffer from catastrophic oxidation at high temperatures and pest oxidation at intermediate temperatures [4-6].

Over the years many approaches have been taken to overcome this issue such as alloying niobium to alter oxidation kinetics. Other avenues of research involved the development of complex microstructures with high volume fractions of intermetallic compounds and silicides.

Development of refractory niobium based alloys can be traced as far back as the early 1950s, granting some perspective on the complexity of problems that have been encountered. Despite these short comings the development of refractory metal alloys capable of operating in aggressive oxidizing environments at temperatures exceeding the operational limit of nickel based super alloys (1150°C) is still needed. Specifically in the aerospace industry where the development of an alloy capable of operating at 1300°C without any auxiliary cooling equipment could result in 50% more power output form turbo jet engines [7]. The schematis in Figure 1.2 shows the functional design of a gas turbine.

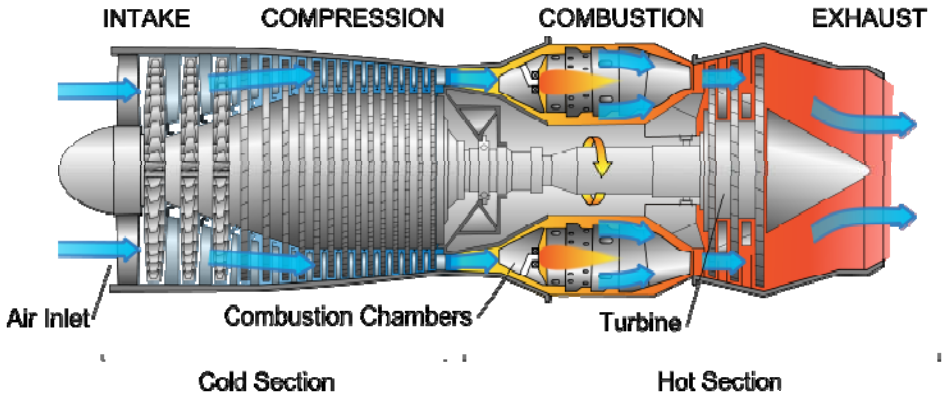


Figure1.2: Functional design of a gas turbine.

Advanced studies have been concentrated in the development of Niobium systems with Al, Cr, Ge, Hf, Si, and Ti additions; often referred to as Refractory Metal-Intermetallic Composites (RMICs). These niobium alloys contain multiphase microstructures comprised of silicides, Laves phase and Nb solid solution [7-14]. The Nb $Cr_2$ laves phase is of particular

interest because it has high melting point (1730$^{o}$C), reasonable density (7.7 g/cm3), high strength, excellent creep behavior and good oxidation resistance. However, this phase exhibits brittleness and limited fracture toughness at low and intermediate temperatures [13, 14].

The multiphase approach has lead to the study of materials with microstructures composed of a dispersion of hard intermetallic particles in a refractory, but, relatively more ductile and solid solution matrix. Thus allows a more favorable balance of high temperature strength and good oxidation resistance.

The addition of Rhenium is considered to impart "*Rhenium-Effect*" in terms of mechanical properties. "*The Rhenium Effect*", is defined as the contribution to an overall improvement of strength, plasticity, weldability, lower ductile to brittle transition temperature and reduced degree of recrystallization embrittlement.[15] The binary alloy system Nb-5at.%Re had a catastrophic failure in terms of oxidation resistance. Higher amounts of Rhenium were added to study the benefits of the rhenium in combination with other alloying elements. The research carried out in this study has been a challenge due to the following reasons:

(1) lack of basic experimental data on thermodynamic, mechanical and physical properties,

(2) difficulties associated with the processing of the alloys, and

(3) scarce information on the conditions required for the formation of a protective oxide scale.

Improvements have been made by adding alloying elements such as Si, Cr, Mo, Ti to study the microstructural constituents and their advantages. [9]

## 1.1 JUSTIFICATION

Addition of Si to niobium based alloys is to produce intermetallics such as $Nb_3Si$, $Nb_5Si_3$. These phases are highly desirable because of their high temperature capabilities and creep resistant properties. Addition of Si to Nb-Re alloy, rhenium-silicides are formed which is forms a protective layer, thus preventing oxidation. Three main rhenium based silicides which are highly desirable are $Re_2Si$ which forms at 1710°C, ReSi which forms at 1880°C and $ReSi_{1.8}$ forms at 1940°C [16].

The addition of Cr enhances in the formation of the Chi-phase (a cubic laves phase, an intermetallic compound), which is very stable and desirable due to its high hardness, which changes the properties of the ternary system on a major scale. Nb $(Cr/Re)_2$ – The new ternary laves phase with hexagonal structure is found to be very advantageous due to its high temperature. The overall ductility is increased by the addition Re in Nb-Cr system. When Re is added >25%, a phase transformation in the Cr rich region is reported. This phase begins to form above 300 °C. [17,18].

The ternary alloy Nb-Re-Si-Al is studied because when Al is added it prevents the metal loss in the Nb-Re-Si system. Between 20 and 40Al, the formation of inter metallic compounds as Re $Al_2$ and Re $Al_4$ form which are stable compound and is resistant to high temperatures. Apart from these the tri Aluminides are also found and known for their high temperature and good oxidation resistant properties. In the Nb-Re-W system the Chi- phase forms when rhenium is added greater than 15%. The formation of beta-oxide (beta –tungsten oxide) is formed when W is added between 5-20%. [19]

Addition of Boron is mainly to produce an oxide rich layer. In the presence of Si, boron form a boro-silicate layer which has good oxidation and high strengths properties which enhances the properties of the alloy. The $B_2O_3$ phase controls the oxidation process of the alloy at early stages, when the Boron content is less than 10%. With additions of Boron to the Nb-Mo-Si , the oxidation resistance is improve, by forming a boro-silicaite layer which acts as a barrier for the oxygen flow into the material [20, 21] Formation of 3 $Nb_2O_5.B_2O_3$ is formed, and an evaporation stage of $B_2O_3$ controlling the oxidation process has been proved by Jing Chang Cheng [15]

## 1.2 STATEMENT OF THE PROBLEM

Although Nickel based alloys have served a prolonged duration in most applications, the need for replacement has occurred due to its density factors. Also Ni based alloy systems have limitations operating in aggressive oxidizing environments, exceeding the operational limit of 1150°C. Aerospace industry demands and develops alloys capable of operating at 1300°C without any auxiliary cooling equipment could result in 50% more power output form turbo jet engines [1]. Thus the need to develop another base metal to form an alloy Niobium, can be suitable base metal for replacement as its refractory metal matrix composites are prime candidates to sustain the operational limits due to the comparable density to that of nickel alloys (density of Ni = 8.912g/cm$^3$ and Nb = 8.57g/cm$^3$) and high melting points. (of Ni is 1455$^o$C and Nb is 2477$^o$C). Few other requirements that need to be satisfied include mechanical properties such as creep resistance and fracture toughness at ambient temperature.

The main drawback of niobium based alloys is that they typically suffer from catastrophic oxidation at high temperatures and pest oxidation at intermediate temperatures. Started back in 1950's, the development of these alloys has never been stopped. Over the years many approaches have been taken to overcome this issue such as alloying niobium to alter oxidation kinetics. Other avenues of research involved the development of complex microstructures with high volume fractions of intermetallic compounds and silicides. Presently, development has improved to a point where alloying has been become very critical. In other words studies are conducted in altering minute amounts of elements to see the variations and to get a balanced and well proportion Nb based alloy.

## Chapter 2 - Background

The studies on Niobium based alloys have undergone a vast improvement in order to determine a balance between chemical and physical properties needed for the use of such alloys in the aggressive environment of turbine engines. After discovering that silicide phases would be desirable from a mechanical standpoint, the focus of many studies have been to increase the oxidation resistance of niobium based alloys. In the further part of this study, it will be very evident that the oxidation properties of pure niobium are very pure. To over this problem alloying elements are added, not only to improve the oxidation properties but also mechanical properties. Few vastly used alloying elements are Al, B, Cr, Hf, Mo, Re, Si, W, Zr.[7-12] Niobium on its own due to its lack of oxidation resistance is one of the most limiting factors for any Nb based system. A few elements considered in this study and their properties are shown in the Table 2.1.

| Element | Nb | Re | Cr | Si | Al | B | W |
|---|---|---|---|---|---|---|---|
| Atomic Number | 41 | 75 | 24 | 14 | 13 | 9 | 74 |
| Density($g/cm^3$) | 8.60 | 21.20 | 7.19 | 2.33 | 2.37 | 2.60 | 19.25 |
| Melting Point (°C) | 2468 | 3186 | 1860 | 1412 | 660 | 2300 | 3422 |
| Crystal Structure | BCC | HCP | BCC | SC | FCC | R | BCC |
| Coefficient of Thermal Expansion (μm/m-°C) | 7.1 | 6.2 | 6.20 | 2.49 | 2.3 | 8.20 | 4.5 |

Table 2.1 Properties of elements used in this study.

## 2.1 Oxidation Mechanisms and Kinetics

The oxidation of metals is a process of corrosion, which takes place at room temperature for all metals or alloys. But, as the temperature of the system is raised the rate of the reaction will increase rapidly to the point where only a few minutes are required to consume the complete metal. At equilibrium conditions, the oxide-metal reaction is highly likely to occur and thus the focus turns to determining the rates of a reaction. The basic chemical formula for the oxidation reaction is:

$$xM + \frac{1}{2}yO_2 \leftrightarrow M_xO_y$$

The driving force ΔG or Gibbs free energy change for the reactions to occur can be calculated using the chemical activity of the reactants and products from the chemical equation, such that:

$$\Delta G = \Delta G^{\circ} + RT\ln\left(\frac{a_{M_xO_y}}{(a_M)^x(a_{O_2})^{\frac{y}{2}}}\right)$$

When, ΔG<0 the reaction will occur spontaneously, if ΔG=0 the system is in equilibrium, and if ΔG>0 the reaction is thermodynamically unfavorable. A generally assumption is made that the activities of the metals and the oxide are equal to 1 and the partial pressure of oxygen ($p_{O_2}$) can be substituted for the activity of oxygen allowing the equilibrium equation to be written as:

$$\Delta G = RT\ln p_{O_2}$$

$$p_{O_2} = \exp\left(\frac{G}{RT}\right)$$

Ellingham diagram are useful in determining which reaction is more favorable, even if the diagrams generally involve only the oxidation of pure elements. However, for alloy systems the activity of the element under consideration is reduced and the associated free energy of the

reaction will change, which in-turn alters the existence and develops a change in the necessary partial pressure of oxygen required for the reaction.

The gas-solid reaction occurs in several steps as Kofstad proposed and is illustrated in Figure 2.1. The Figure 2.1 illustrates that the oxygen within the atmosphere is first adsorbed on the metal surface. Then, oxide nuclei develop on the surface grow laterally across the surface in thermodynamically favorable locations. As the film develops the diffusion of oxygen proceeds through the scale unless a barrier to the penetration is developed, some classic examples of barrier or passive oxides are $Cr_2O_3$, $Al_2O_3$, and $SiO_2$. The depth of oxygen penetration into the base metal can develop internal oxidation if the activation energies of the metal components are low enough. Concurrently the metal ions will diffuse towards the surface of the developing scale, during this period they may combine with the inwardly diffusing oxygen. The oxides that are formed in this period may be stable or may volatize to form internal pores within the scale. The stresses developed in the scale by either differences in coefficients of thermal expansion between oxides or the oxide-metal interface and the pressure exerted by gas filled pores can cause cracking in the scale yielding a path for direct interaction between the atmospheric oxygen and the heated metal surface. [27]

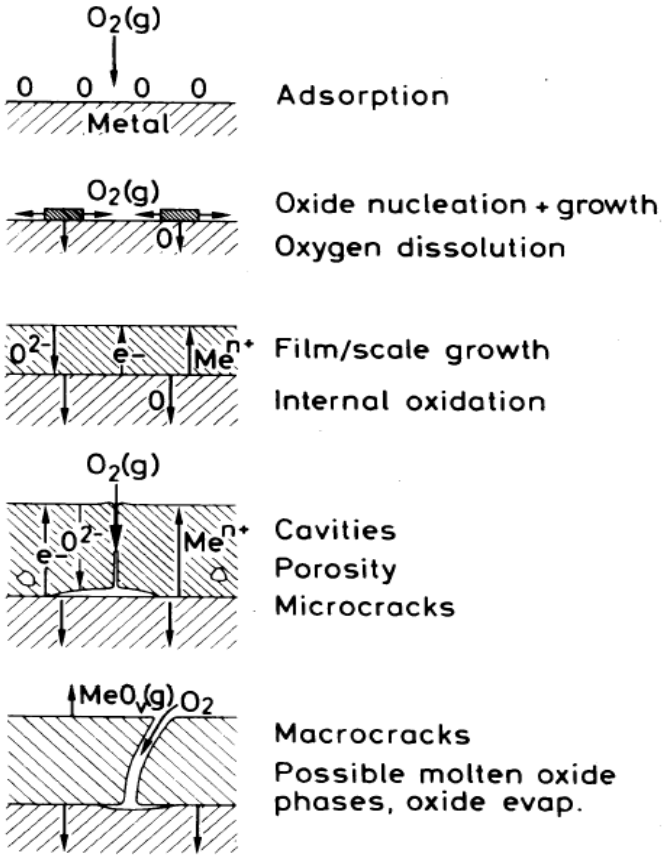


Figure 2.1 - Schematic of metal-oxygen reaction.

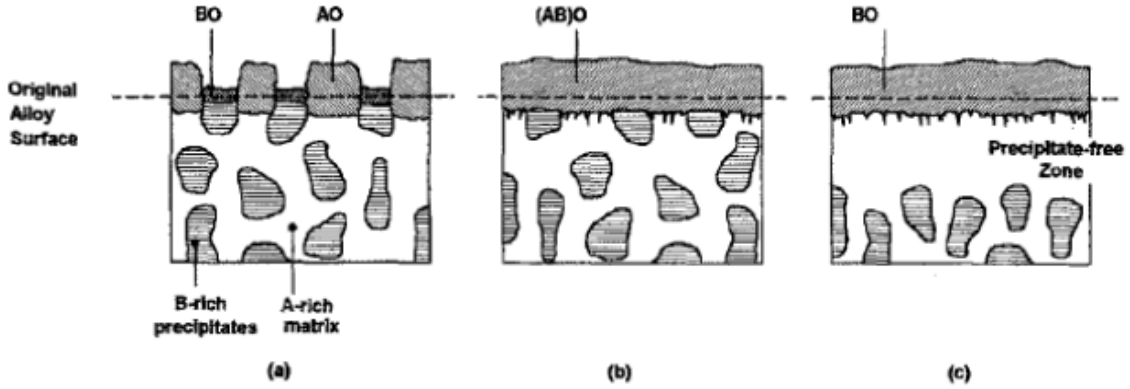


Figure 2.2 -Oxidation behavior observed in two phase alloys (a) independent oxidation forming a non-uniform scale, (b) cooperative oxidation forming a uniform scale, and (c) solute rich phase acts a reservoir for growth of solute scale.

As a general rule of thumb that can determine whether the oxide will be protective or not is the Pilling-Bedworth Ratio. The ratio compares the atomic weight and density of the oxide to the substrate and can be simplified to a comparison of the volumes.

$$P-B\ Ratio = \frac{A_o \cdot \rho_m}{n \cdot A_m \cdot \rho_o} = \frac{V_m}{V_o}$$

The Pilling-Bedworth ratio for a protective oxide is approximately 1. For values less than one a porous scale is developed and for those that exceed a value of 2 the oxide will flake away, or spall off. The consideration of the volumes of the substrate and the oxide lead to the need for similar coefficients of thermal expansion which would prevent large changes in volume to cause stress formation at interfaces. [29]

To describe the behavior of alloy oxidation there are three rate laws that can be described: linear, parabolic, and logarithmic. A schematic of the behaviors has been adopted in Figure 2.3 to detail the differences in behaviors graphically. In detail discussion of PB ratio is reported further in the study.

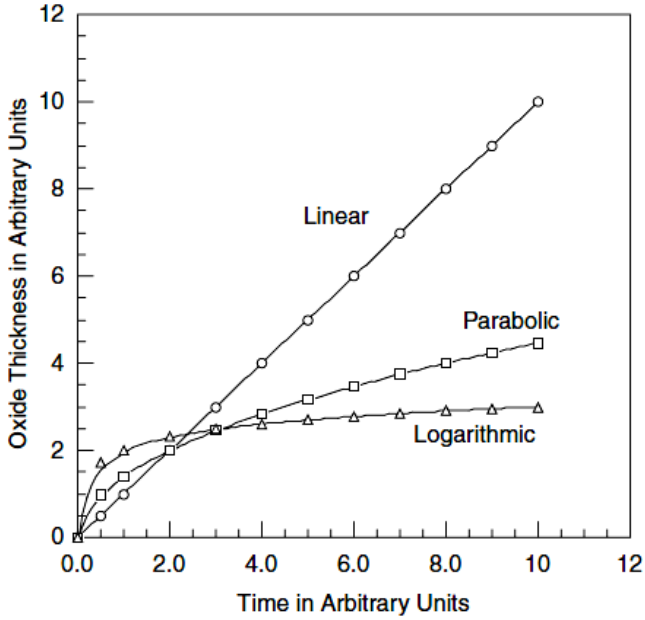

Figure 2.3 - Graphical representation of the three rate laws in arbitrary units, adapted from [29].

If an oxide follows the linear rate law of behavior, the scale is considered un-protective as this suggests continuous contact between the substrate and the reactant (air) through either cracks or pores in the film. The rate of oxidation is constant and is related to the thickness of the oxide versus the time of exposure such that:

$$\frac{dx}{dt} = k$$

The integration of the equation results in the simple linear equation:

$$x = kt + const$$

Where the constant can be calculated from experiments, where a clean surface will have x=0 at t=0. If the thickness is changed to weight through the oxide density, the equation has the same form:

$$w = k't + const$$

$$k' = k\rho_a$$

The parabolic behavior can be described as the mechanism during which oxygen diffusion to the substrate is reduced as the oxide layer increases or more simply as the scale thickness increases the oxidation rate decreases. The equation to describe this behavior is given:

$$\frac{dx}{dt} = \frac{k'_p}{x}$$

Where $k'_p$ is the parabolic constant, the equation can be integrated such that:

$$x^2 = \frac{k'_p}{2} + const$$

Where x is the thickness of the oxide and t is the time of oxidation. This is the rate law that corresponds to the development of protective oxides and suggests that the controlling method is through the diffusion of ions/electrons through the scale.

For very thin scales ($t \leq 1{,}000\text{Å}$) or at lower temperatures the logarithmic rate law is utilized to describe oxidation. In this case it is generally thought that the rate is controlled by electron transfer across the film.

$$y = k''\log(ct + 1)$$

In addition to the energy of formation the oxidation rate constant is also temperature dependant, following an Arrhenius-type equation:

$$k = k_o \exp\left(\frac{Q}{RT}\right)$$

However, simply the change in activation energy is not sufficient to explain the change in oxidation mechanisms, as other time/temperature mechanisms may be involved, such as self-diffusion of ions within the oxide scale.

As can be gathered from the requirement of different laws to explain general behavior, there are many considerations involved to completely describe oxidation mechanisms in alloys. The complexities of alloy oxidation stem from a variety of topics, such as the differing activation energy of the elements, various diffusivities of the alloying elements, and the existence of ternary or complex oxide, to name a few. There have been several models proposed for alloy oxidation, in the case of single-phase alloys Wagner's model has sufficed. However, for multi-phase alloys there must be some extension of the theory. Theoretical studies [30- 33] have focused on the treatment of an alloy consisting of two phases, an oxide forming element M rich matrix and an M rich precipitate. Gesmundo *et al.* summarized the findings and presented the various forms that the corrosion of two-phase alloys may take according to the findings presented. [34]

## 2.2 Thermodynamic Considerations:

The driving force for metal-oxygen reactions is the Gibbs freeenergy change, ΔG. Since the conditions most often encountered in high temperature reactions are constant temperature and pressure, ΔG is described by the second law of thermodynamics as:

$$\Delta G = \Delta H - T.\Delta S$$

where ΔH is the enthalpy of reaction, ΔS is the entropy change, T is the absolute temperature. An oxidation reaction will occur spontaneously if ΔG<0, if ΔG=0, the system is at equilibrium, and if ΔG>0 the reaction is thermodynamically unfavorable.

The driving force ΔG for the oxidation reaction in Equation 2.1 can be expressed as:

$$\Delta G = \Delta G^{o} + RT\ln\left(\frac{a_{M_xO_y}}{(a_M)^x\left(a_{O_2}^{\frac{y}{2}}\right)}\right)$$

where the chemical activity, $a$ , of each reactant or product is raised to the power of its stoichiometric coefficient,$\Delta G^{o}$ is the standard free energy of formation and R is the gas constant.

Generally, the activities of the metals and the oxide are considered to be equal to 1, and the oxygen partial pressure is used for the activity of the oxygen. Therefore at equilibrium Equation 2.3 can be written as:

$$\Delta G = RT\ln p_{O_2}$$

$$p_{O_2} = \exp\left(\frac{g}{RT}\right)$$

where, $Po_2$ is the partial pressure of oxygen. Equation 5 is used to determine the partial pressure of oxygen in equilibrium with the oxide from the standard free energy of formation. Thermodynamically the oxide will form only if the oxygen potential in the environment is larger than the oxygen partial pressure in equilibrium with the oxide.

A plot of the standard free energy of formation of metal oxides as a function of temperature and the corresponding dissociation pressures of the oxides is known as Ellingham diagram Figure 2.4. These diagrams are used to get information about the partial pressure of oxygen required for any metal to form oxides at different temperatures. The stabilities of various oxides may be compared directly, the lower the position of the line on the diagram, the more stable is the oxide [35].

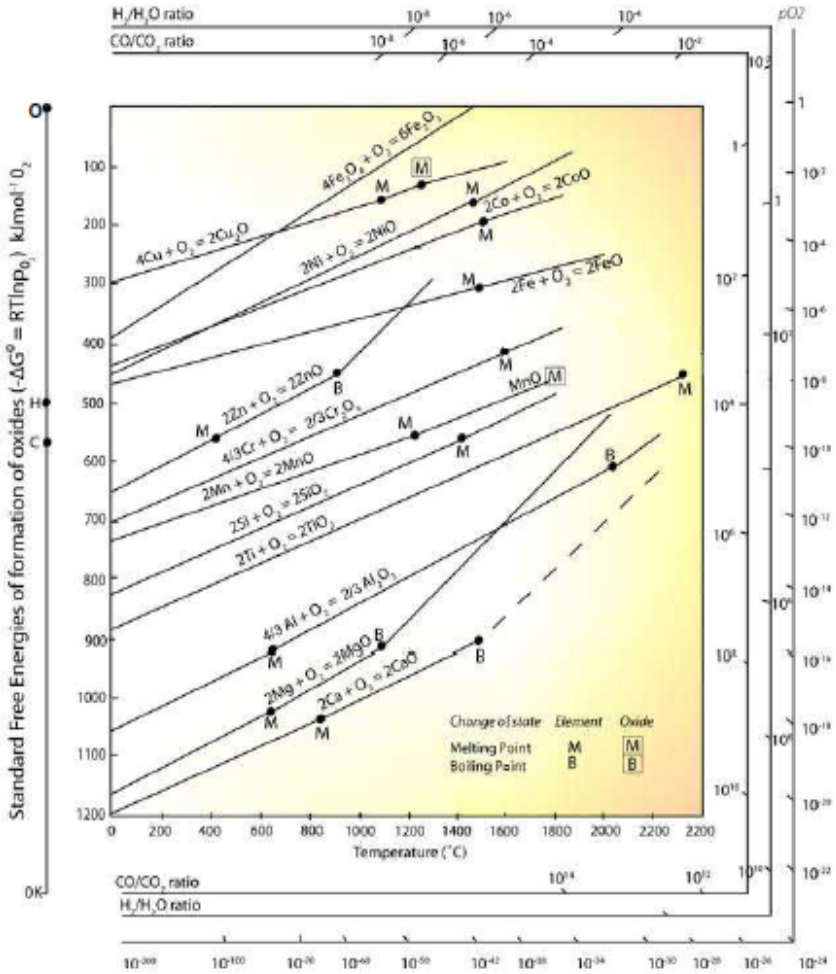


Figure 2.4: Ellingham diagram - Standard Gibbs energies of formation of selected oxides as a function of temperature.

**Pilling-Bedworth Ratio (PBR)**

The resistance of a metal to high temperature oxidation requires the formation of a protective barrier and the maintenance of this protection is required in order to achieve continuous resistance. The characteristics of the oxide scales formed play an important role in the oxidation process of any metal. As oxide scales grow, stress generation may cause scale cracking and spallation. The stresses developed during scale formation are usually classified as: growth stresses, transformation stresses which occur when a crystallographic phase transformation takes place, and thermal stresses due to the thermal expansion between oxide and metal. Although the precise origin of the growth stress is complex and not fully understood, it is believed that it is strongly affected by the volumes of metal and oxide; the crystal structures of oxide and metal, and the oxide growth mechanism [37].

In 1923 Pilling and Bedworth [38] classified oxide scales into two main classes according to the protective properties of the scales; those which form protective oxides, and those which cannot. The type of oxide scales that form is dependent on the relative volumes of both the metal and the resulting oxide. The ratio of these volumes is the Pilling-Bedworth ratio:

$$PBR = \frac{V_{ox}}{V_m} \tag{2.6}$$

where, $V_{ox}$ and $V_m$ are the volume of the oxide and the metal respectively.

PBR values determine the type of oxide formation. It could be concluded that, the oxide scale is porous and un-protective, when PBR value is lower than 1. When PBR is equal or greater than 1, a protective scale is formed and the oxidation can proceed only by solid-state diffusion. As PBR deviates from 1, the growth stress rises. But for PBR greater than 2, greater compressive stresses induce causing the scale to crack and/or flake off. During this process, it is

important to note that each time the oxide layer flakes off, a fresh unprotected metal surface is exposed and so the process continues.

Although this theory is considered and counted, many exceptions to this philosophy (PBR rules) are also considered. Most of which are attributed to the mechanism of the oxide growth. Since the PBR theory is based on the assumption that oxygen needs to diffuse through the oxide layer to the metal surface. But in reality, it is often the metal ion that diffuses to the air-oxide interface. Nevertheless, Pilling and Bedworth made the first step in achieving understanding of the metal-gases reaction process. The volume ratio, as a rough rule-of-thumb, is usually correct [39]. Table 2.2 lists the PBRs for some common oxides.

Table 2.2: Pilling-Bedworth Ratio for some common oxides

| Oxide | Volume Ratio |
|---|---|
| $Al_2O_3$ | 1.28 |
| $Cr_2O_3$ | 2.07 |
| $\alpha\ Fe_2O_3$ | 2.15 |
| $Nb_2O_5$ | 2.68 |
| $SiO_2$ | 2.15 |
| $TiO_2$ | 1.76 |
| $WO_3$ | 3.30 |

## 2.3 Niobium and Rhenium as High Temperature Materials

In comparison, niobium and its alloys exhibit properties that provide technological capabilities of great importance among the refractory metals. Niobium was discovered more than

two hundred years ago. Not until the 20th century, Nb was used commercially. Brazil is the leading producer of niobium and ferroniobium, an alloy of niobium and iron. Niobium is used in the field of oil and gas transportation, aircraft engines, automotive industry, nuclear industry, construction, jewelry and in magnetic applications such as medical diagnosis devices. The low neutron capture cross-section make it suitable for nuclear energy applications. Nb is resistant to some types of chemical attack. Its melting point, density and high melting oxide make it an attractive candidate as a base metal for high temperature structural materials. Approximately 95% of all niobium is used as alloy additions in steel and nickel alloys. Only 1-2% of niobium is used as pure niobium metal or for niobium-based alloys [40].

Appreciable amounts of the element are used in nickel-, cobalt-, and iron-based superalloys for such applications as jet engine components, gas turbines, rocket subassemblies, and heat resisting and combustion equipment. One example of a nickel-based niobium-containing superalloy is Inconel 718, which consists of approximately 53% Ni, 19% Cr, 18.5% Fe, 5% Nb, 3% Mo, 0.9% Ti, and 0.5% Al [41]. Even the most advanced superalloys cannot meet the challenges imposed by the performance requirements of power generation systems because of the melting temperature of nickel.

The advantages of niobium as compared with other refractory metals can be summarized as follows:

a. Least dense and most ductile of all refractory metals.
b. strength can be improved by alloying
c. Superior to molybdenum and its alloys (the closest rival for high-temperature uses).

However, the main disadvantage of Nb is its poor oxidation resistance at moderate and high temperatures. A protective oxide layer may help improve the alloys oxidation resistance, by decreasing the flow of oxygen into the alloy system. Their refractory metal intermetallic composites depend on an intermetallic phase to provide high temperature oxidation resistance [2].

Rhenium standing alone results in pesting at lower temperatures and therefore adding elements such at Si and Cr would improve the properties and also produce mutual solubility of rhenium and chromium disilicides. The system Re − Cr − Si results in micro-structural constituents such as rhenium and chromium disilicides are promising for development of resistive materials with high electrical resistivity and low temperature coefficient of resistance. The presence of silicon in the alloy decreases the lattice parameter for chromium, due to silicon dissolving in it. This mechanism indicates higher diffusional mobility for the latter in the low temperature region. [42]

**2.4 Oxidation of Niobium**

Explaining the process of oxidation of niobium is complex. Many factors affect the oxidation mechanism. Depending upon temperature, oxygen pressure and oxidation time the oxidation patterns can be parabolic or linear. Hurlen [43] performed an extensive study of the reaction of niobium with oxygen at different pressures and temperatures from 150ºC-1000ºC. According to this study, the sequential stages in the oxidation of Nb are: linear (I), parabolic (II), a rate increasing transition, linear (III), parabolic (IV) and parabolic (V). Kubaschewski and Hopkins presented a review of the oxidation kinetics of niobium. [44]

The sequential steps in the oxidation mechanism can be described as:

(a) Parabolic growth of a dense oxide scale surface from 300ºC to 500ºC.

(b) Linear growth rate from 500ºC to 1000ºC caused by cracking and spalling of the dense layer.

(c) Accelerated oxidation from 1100ºC to 1250ºC.

(d) Extremely rapid oxidation at temperatures above 1300ºC.

As oxygen dissolves interstitially, the niobium lattice expands as oxygen is dissolved. Brauer [45] estimated that the solubility limit of oxygen in niobium to be less than 4.7 at% at 1600ºC-1700ºC. Seybolt [46] reported values of 1.4 at% at 775ºC and 5.5 at% at 1100ºC. Bryant [47] has determined that the solubility ranges from 0.7 at% at 750ºC to 5.5 at% at 1540ºC. According to Elliot [48] the oxygen solubility rises from 1.4 at% at 500ºC to 3.9 at% at 1800ºC.

Brauer [49] identified NbO, $NbO_2$, and $Nb_2O_5$, as the only equilibrium oxides of niobium, with $Nb_2O_5$ having three polymorphs. The main features of the Nb-O diagram have been established by Elliot [50]. The solubility of oxygen in α-Nb varies from 1.4 at% at 500ºC to 4.0 at% at 1915ºC. $NbO_2$ and NbO melt congruently at 1915ºC and 1945ºC respectively, while $Nb_2O_5$ melts at 1495ºC [50,51]. The phase diagram for the Nb-O system is presented in Figure 2.5 [52]

The polymorphism of niobium pentoxide throughout the process of oxidation has three different forms and each of them is identified with a unique prefix. Classification of the modifications of $Nb_2O_5$ is unique and sometimes confusing due to the uncorrelated nomenclature

used to designate the polymorphs. These three modifications with respect to nomenclature and at the temperature it forms:

• T-$Nb_2O_5$ (low temperature) stable up to 900ºC.

• M-$Nb_2O_5$ (medium temperature) stable between 900ºC and 1100ºC

• H-$Nb_2O_5$ (high temperature) stable at temperatures above 1100ºC. [46]

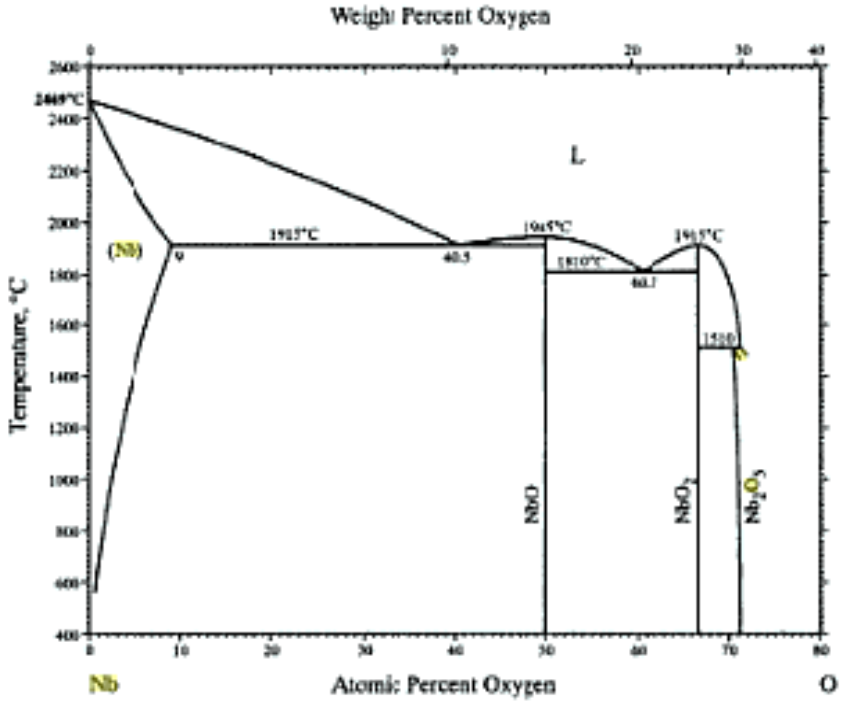


Figure 2.5 The phase diagram of Nb – O

Also, Goldschmidt [52] re-investigated the polymorphic forms, reporting two other modifications:

•α-$Nb_2O_5$ (Orthorhombic): It is also called "low temperature" modification, is metastable and transforms spontaneously to β-$Nb_2O_5$.

• β-$Nb_2O_5$ (Base centered monoclinic): It is also called "mid- temperature" modification and is the stable form between 900- 1100ºC.

- β-$Nb_2O_5$ (Monoclinic): It is also called "high - temperature" modification and is the stable above 1100$^oC$.

Many other modifications have been found and numerous observations have been made with respect to the modes of formation, structure and stabilities. A comprehensive review and classification of the modifications of niobium pentoxide was made by Schäfer et al. [53].

**2.5 Oxidation of Rhenium**

Rhenium is known to form eight different oxides under oxidizing atmospheres. However $Re_2O_7$ (g), $ReO_3$ (g), and $Re_2O_6$ (g) are three principle oxides. The principal reactions are:

2 Re(s) + 7/2 $O_2$ (g) = $Re_2O_7$ (g)

Re(s) + 3/2 $O_2$ (g) = $ReO_3$ (g)

2 Re(s) + 3 $O_2$(g) = $Re_2O_6$(g)

These oxides are very volatile. This high volatility is responsible for the rather poor oxidation properties of rhenium at high temperature, as it prevents the formation of any protective oxide layer on the metal surface. The first oxide has been studied extensively, less is known about the second, and relatively little is known about the third. [54]

Lavrenko [55] studied the oxidation of Re from 350 to 750°C in air, finding linear reaction rates, representing a steady loss of metal and volatilization of the oxides. Gulbransen and Brassart [56] examined the oxidation of Re in flowing oxygen from 600 to 1400°C in oxygen from 1 to 10 Torr (0.0013–0.013 bar). This study resulted in a controlled process of chemical reaction at the interface at lower temperatures; at higher temperatures the process was controlled by gas-phase diffusion to the sample.

Rosner and Allendorf [57] examined the oxidation of rhenium ribbons at surface temperatures of 973 to 3273°C under conditions intended to minimize diffusion limitations. Their data suggest complex reaction kinetics, which are highly dependent on temperature. More recently, Alnot and Ehrhardt [58] examined the oxidation of Re at 427°C and 1 Torr of oxygen with X-ray photoelectron spectroscopy (XPS) and ultraviolet photoelectron spectroscopy (UPS). They found traces of $ReO_2$, $ReO_3$, and $Re_2O_7$ on the surface of samples.

### 2.6 Oxidation of Nb based alloys

Vast amount of research has been carried out on the oxidation characteristics of Nb-based alloys and not a permanent solution has been discovered yet to eradicate the problem. However, methods have been discovered to control the process of oxidation. One of such discoveries is the formation of protective oxide layer. Published research has shown that the scale formed on niobium above and about $600^{o}$ C is porous and not protective [59] which increases the kinetics of oxidation. The first goal of the alloying addition is to provide a scale that is tight and adherent, and whose rate of growth is diffusion-controlled. Additionally, alloying may alter the rate of growth of this scale.

The majority of the initial research was focused on alloying Nb with different elements to either reduce or control oxidation kinetics. These studies, reviewed extensively by Stringer [60], indicated that the formation of $Nb_2O_5$ was too dominant to be altered by the alloying additions [19].

Studies were conducted to understand the oxidation characteristics of Nb-Al alloys. The aim to consider this alloy was to achieve the formation of a protective $Al_2O_3$ scale. Nb-Al system has three intermetallics, $Nb_3Al$, $Nb_2Al$, and $NbAl_3$, all three are considered to be highly

advantageous. The oxidation characteristics of the phase $NbAl_3$ have been studied by several researchers since it is the only intermetallic phase that forms $Al_2O_3$ when oxidized at high temperatures (above 1000$^o$C) [62-64]. However, this phase cannot sustain the growth of a protective oxide layer. The selective oxidation of the aluminum results in the surface stabilization of the non-protective niobium oxides [64-66]. The oxidation resistance of Nb-Al alloys may be increased by adding elements that decrease the diffusivity of oxygen and increase that of aluminum in the metal matrix. Additions of Ti, V, Cr have been used for this purpose. However these elements also decrease the melting point and have negative effects on the mechanical properties [66].

A study of NbAlCrY alloys performed by Hebsur et al. was oriented to improve the oxidation behavior of Nb-$Al_3$ based alloys [67]. The intent was to expand the $NbAl_3$ phase field to lower aluminum levels such that oxidation to form $Al_2O_3$ would delay the eventual formation of the $Nb_2Al$ in the alloys. The oxidation behavior of the alloys was improved; however, the protective scale formation appeared to be related to the Cr-rich intermetallic grain boundary phases rather than the $NbAl_3$-base matrix [61].

Further studies performed on two-phase Nb-$Nb_5Si_3$ system indicated that the alloys from this system have an attractive balance of high and low temperature mechanical properties. Unfortunately, the composites from binary Nb-Si alloys still suffer from catastrophic oxidation upon exposure to air at temperatures above 500$^o$C [11,13]. The Nb-$Nb_5Si_3$ alloys oxidize mainly by oxygen diffusion, with the rapid formation of stratified and porous layers, which spall off. [9]. The studies performed on this system have evolved gradually from a binary model system to a multiphase, multi-component system of Nb with the additions of Ti, Al, Hf and Al [2, 3, 11, 13, 67-69] Subramanian el al. [69] examined the oxidation behavior of Nb-(10-20)Si alloys with

ternary Mo, W, V, Ti, Zr, and Ru additions as well as quaternary Nb-Si-Ti-Al alloys. The study showed that the most promising alloys systems were those with Ti and Al additions to Nb-Si alloys.

Menon et al. [70] reported the oxidation behavior of several Nb-Si with different alloying elements. The oxidation products observed include $TiNb_2O_7$, $CrNbO_4$, $SiO_2$, $3Nb_2O_5 \cdot TiO_2$, and $Nb_2O_5$. The results also indicated that the Nb solid solution phase oxidizes selectively.

The oxidative instability of Nb-Si alloys led the researchers to add small amount of boron to imitate the Mo-Si-B system to form a protective borosilicate glass layer. Studies performed by Murakami et al. [71] indicated that the scale formed consisted of $Nb_2O_5$, $SiO_2$ and a large number of pores and no continuous glass layer was observed. Liu et al. and Behrani et al. [7, 51] also studied the oxidation properties of Nb-Si-B alloys and reported that the oxidation behavior of alloys from this system is inferior to that of the Mo-Si-B system. The difference in oxidation stability of boron modified Mo-Si and Nb-Si may be attributed to the non-volatile nature of the oxide formed and the high porosity of the scale on Nb-Si-B alloys [7].

Refractory metals and their alloys can suffer from pest damage at intermediate temperatures (<850$^{o}$C) [71]. Niobium has a high solubility for oxygen, and its silicides also suffer from pest oxidation [67,68]. Additions of Al and Hf are known to reduce the pesting susceptibility of Nb-based alloys, but some Nb-silicide based composites can still be attacked [10]. Bewlay et al. reported that alloying with Sn has been really effective in managing pesting damage [13]. Studies performed by Geng et al. revealed that additions of 5at.% can significantly control pest oxidation behavior [14]. The addition of Cr has been found to improve the oxidation resistance which has been attributed to the stabilization of the $NbCr_2$ Laves phase [10].

Cyclic oxidation studies performed by Chan [17, 19] on multiphase alloys, containing silicide, Laves and Nb solid solution phases, indicated that the oxidation products are mainly $CrNbO_4$, $Nb_2O_5$, and $Nb_2O_5 \cdot TiO_2$. The oxidation resistance was improved when $CrNbO_4$ formed instead of Nb2O5. The oxidation resistance of multiphase Nb-based alloys is substantially better than that of niobium and conventional Nb alloys; and it is comparable to that of Ni-based superalloys at 1000ºC. The numerous studies performed provide evidence that these alloys could meet the required oxidation resistance goal for a metal surface temperature at 1315ºC. The short-term goal is for a loss of <200 μm in 10 hours at 1370 °C. The long-term goal is for a loss <25 μm in 100 hours at 1315 °C [3, 72]. This is derived from the requirement of achieving the oxidation life at 1315°C that the 2GSX nickel-based superalloys presently exhibit at 1150°C.

An attempt was made to study the oxidation behavior of the alloys from Nb-Si-B system to determine whether $Nb_5Si_xB_x$ phases may offer oxidation resistance to niobium based alloys. Oxidation resistance of $Nb_5Si_3B_2$ was found to be superior to undoped $Nb_5Si_3$ as reported by Murakami et al. [71] Upon addition of boron, $Nb_5Si_xB_x$ type silicides, develops a continuous borosilicate glass layer from $Nb_5Si_3B$. But practical studies conducted found that it not possible due to the development of non-volatile $Nb_2O_5$. On a side note Behrani et al. attempted to promote the volatilization of $Nb_2O_5$ through a chlorination treatment to develop a continuous layer of borosilicate glass [27]. Also, studies by T.Murakami, confirmed that the short-duration oxidation experiment shows that $Nb_5Si_3B_2$ is superior to $Nb_5Si_3$ in oxidation resistance. However, the oxidation resistance of $Nb_5Si_3B_2$ is extremely poorer than that of $NbSi_2$. From studies conducted by Yu.B.Kuzma, the studies of Nb-Re-B, $Re_3B$ and $ReB_3$ dissolve up to 5 at.% Nb, as a result of which their lattice constants increase with no solubility of Nb in $ReB_2$ was

detected. The solubility of niobium in this phase was 5 at.% Re are Nb B and $Nb_3B$. A ternanry compound was also detected at 40 at.% B section, which is $Nb_3Re_3B_4$. [72] All the oxidation studies conducted with boron additions, are mainly to observe a continuous layer of boro-silicate. However, the best results were observed in Mo-Si-B alloy where this layer was found almost continuous and definitely, improving the oxidation properties. [73]

The alloys Nb-20W-5Cr and Nb-20W-10Cr showed complete powder formation after oxidation at 800°C and 900°C. This may be attributed to the large differences in the linear thermal expansion of the oxides, particularly $WO_3$. The change in coloration of the powders at different temperatures is likely due to the various amounts of the alloys Nb-20W-5Cr and Nb-20W-10Cr showed complete powder formation after oxidation at 800°C and 900°C. This may be attributed to the large differences in the linear thermal expansion of the oxides, particularly WO3. The change in coloration of the powders at different temperatures is likely due to the various amounts of oxides present.

Oxidation resistance increases with an increase in temperature from 1,200°C to 1,400°C, likely due to the higher solubility of oxygen in niobium resulting in the declaration of a non-protective layer of $Nb_2O_5$. The presence of $NbO_2$, $Nb_2O_5$, $WO_2$, $WO_3$, $Cr_2O_3$, and $NbCrO_4$ has are the oxides detected form Nb-Cr-W alloys. Studies by Maria D. Moricca and S.K. Varma on High-temperature oxidation characteristics of alloys from the Nb-W-Cr system with C additions, proved to improve the oxidation properties over the alloy with C modifiers, than the one without. Although they found pesting at lower and m id temperature range, the alloys were stable at 1200-1400$^{o}$C. [74, 75]

## 2.8 Preliminary studies of Nb-Re based alloys:

Alloys with binary, ternary and quaternary compositions were developed as a preliminary study to understand the formation of phases and oxidation resistance of these alloys. The binary alloys (Nb-5Re, Nb-5Si and Nb-5Cr) reveal the formation of a single phase, $Nb_{SS,}$ $Nb_{SS}$+ $Nb_3Si$ and $Nb_{SS}$+$NbCr_2$ respectively. Addition of Re to form ternary alloys, has helped in the formation of $Nb_5Si_3$ and (Nb, Re) $Cr_{2,}$ in Nb-5Re-5Si and Nb-5Re-5Cr respectively. Quaternary alloy Nb-5Re-5Si-5Cr has $Nb_5Si_3$, $NbCr_2$ and $Nb_{SS}$. Conclusion from this study were made as follows:

1. Rhenium has helped in the formation of 3,5 silicide in the Nb-5Re-5Si alloy. Whereas in the binary alloy, it was observed that the formation of 1,3 silicide. 3,5 silicides are preferred because of their high temperature and better creep resistance.
2. Oxidation resulted in pesting at all temperatures (700-1000$^{o}$C). Large amount of niobium solid solution has led to form Nb based oxides resulting in powdered oxidation products.
3. Mass loss for alloys is due to the volatile rhenium and chromium oxides, and the weight gain at for alloys is due to the formation of $Nb_2O_5$ bulky oxides. XRD confirms these observations. The development of these alloys is shown in the Figure below.

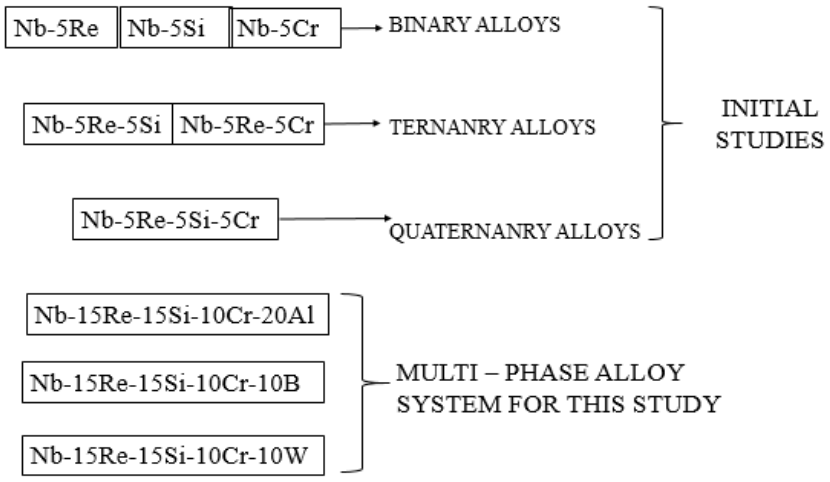


Figure 2.6: Development of alloys in this study

Studies from Ti additions (Nb-15Re-15Si-20Cr-15Ti) resulted in $Nb_5Si_3$, $Cr_2Re_3$, Nb solid solution and Laves phases. The combinations of these phases have drastically improved the oxidation properties. $Cr_2Re_3$ is considered as a high temperature component, therefore it is understood that this phase might help in improving the overall oxidation properties. Formation of $Nb_2O_5$, $CrNbO_4$ and $SiO_2$ were found to be advantageous. β-$Nb_2O_5$ has been observed at 700 and 800$^oC$, monoclinic form of $Nb_2O_5$ and $CrNbO_4$ starts to form at 900$^oC$. The improved oxidation resistance of the alloy can be attributed to the formation of $CrNbO_4$ which starts to form at 900$^oC$. The formation of internal oxidation was the disadvantage in this alloy. However, this effect was not noticed until 1200$^oC$. About 70% of the metal was left at the end of a 24 hour cycle at 1400$^oC$. [76]

Nb-15Re-15Si-10Cr-20Mo alloy studies showed the formation of $Re_2Si$, $(Nb,Mo)_5Si_3$, $NbCr_2$ and α-solid solution. $Re_2Si$, formed around the solid solution and proved to prevent the infusion of oxygen when subjected to the oxidation process. The Laves phase was formed in limited amounts, on a relative scale, throughout the structure. The important aspect is to understand how rhenium silicide layer can act as a protective barrier preventing the diffusivity of oxygen into the metal. Oxide products were subjected to X-ray diffraction to characterize the oxide products. Trends of the samples vary accordingly between low (700-900$^oC$), mid (1000 and 1100$^oC$) and high temperature ranges (1200-1400$^oC$). $Nb_2O_5$ and $SiO_2$ have been detected, from 700 – 1300$^oC$ at all temperatures. However the forms of $Nb_2O_5$ were different. At 900$^oC$, the set of $Nb_2O_5$ peaks seems to slightly shift to the left indicating the change in the form, compared to the peaks obtained at 700$^oC$. Also a noticeable increase in the intensity has been

observed. Starting from 900oC, $CrNbO_4$ starts to form along with the formation of $Nb_2O_5$ and $SiO_2$. Molybdenum oxide rich zone ($MoO_3$ or other forms of $Mo_xO_{3x}$) was formed at 1400$^oC$ [77]

## Chapter 3 – Experimental Details

### 3.1 Sample Preparation

Alloys with composition of Nb-15Re-15Si-(20Al,10W) (in atomic percent) were fabricated by the Ames Laboratory of Iowa State University using an arc melt process in a high purity argon atmosphere. Buttons of the alloys were re-melted several times to ensure homogeneity. Electric discharge machining (EDM) was used to cut the alloy into 5 mm cubes. The nominal compositions of the alloys used in this study are given in Table 3.1. As-received samples were polished to a 600 grit finish to remove surface contamination from the machining process and then ultra-sonically cleaned in methanol before oxidation experiments. Samples were weighed and surface area was calculated prior to oxidation experiments.

Table 3.1 Compositions of the alloys used in this study

| Alloy Identification | Composition (at %) Nb | Re | Si | Cr | X |
|---|---|---|---|---|---|
| Nb-5Re, Nb-5Si, Nb-5Cr | 95 | 5 | 5 | 5 | |
| Nb-5Re-5Si, Nb-5Re-5Cr | 90 | 5 | 5 | 5 | |
| Nb-5Re-5Si-5Cr | 85 | 5 | 5 | 5 | |
| Nb-15Re-15Si-10Cr-20Al | 40 | 15 | 15 | 10 | 20 |
| Nb-15Re-15Si-10Cr-10W | 50 | 15 | 15 | 10 | 10 |

### 3.2 Short Term Oxidation (STO) Experiments:

Oxidation was carried out in standard lab air at temperatures of 700-1400°C representative of low (700-900°C), mid (900-1100°C) and high (1200-1400°C) temperature ranges. Furnaces were computer controlled with a ramp rate of 10°/min and all samples were furnace cooled. Samples were weighed after cooling. The three new alloys were exposed to a single 24 hour static to study the oxidation behavior. Similar analysis of the oxide products and any microstructural changes were studied.

### 3.3 X-ray Diffraction Analysis

Samples were characterized by X-ray Diffraction in a Bruker D8 Discovery using CuKα radiation. The parameters for the scans included a 5°/min scan rate, 0.05 measurement increments, use of the 0.8mm slit on the x-ray source, and 8mm slit on the detector. The scans were performed on the surface of the resultant oxide scales as removal of the scale without damage to the base metal was not possible. The scans were characterized by pattern comparison with the JCDPS card database.

### 3.4 Scanning Electron Microscopy

Samples were mounted in an epoxy resin, sectioned, and polished to a 1200 grit finish to examine the scale cross section. Oxide metal interfaces were characterized by secondary electron microscopy (SE), backscatter electron microscopy (BSE), Energy Dispersive X-Ray Spectroscopy (EDS), and x-ray mapping in a Hitachi S-4800 UHR FE-SEM. After sectioning and polishing the oxide samples, the un-oxidized metal remaining for the samples was estimated by comparing the resultant cross-sectional area of the metal to the original cross-sectional area of the samples. For the samples involved in the three-week exposure experiment the samples were viewed using the SEM prior to mounting to view the surface features of the developed oxides.

The samples were directly mounted on the stage using carbon tape, the face that was adhered to the stage was the face chosen to be polished away.

### 3.5 Image Analysis

In order to determine the phase fractions of the alloys image analysis was carried out on the as cast microstructures to determine the phase fractions. Calculations are based on the contrast of each phase present in the as-cast condition at suitable magnifications of backscatter, secondary electron imaging (as when needed, the adjustments were made).

## Chapter 4 – Results and Discussion

**4.1 Binary Alloys:** The binary alloys with additions of 5%Re, 5%Si, 5%Cr to Nb, resulted in the formation of the $Nb_{SS,}$ $Nb_{SS}$ + $Nb_3Si$, $Nb_{SS}$ + $NbCr_2$ respectively. This is in agreement with the formation of the phases which are calculated by the PANDAT$^{TM}$ software, except Nb-5Si. For this alloy, PANDAT$^{TM}$ predicts the formation of $Nb_5Si_3$. However the SEM and XRD data depicts $Nb_3Si$. Figure 4.1 shows the binary phase diagrams for Nb-5Re, Nb-5Si and Nb-5Cr alloys constructed by using PANDAT$^{TM}$.

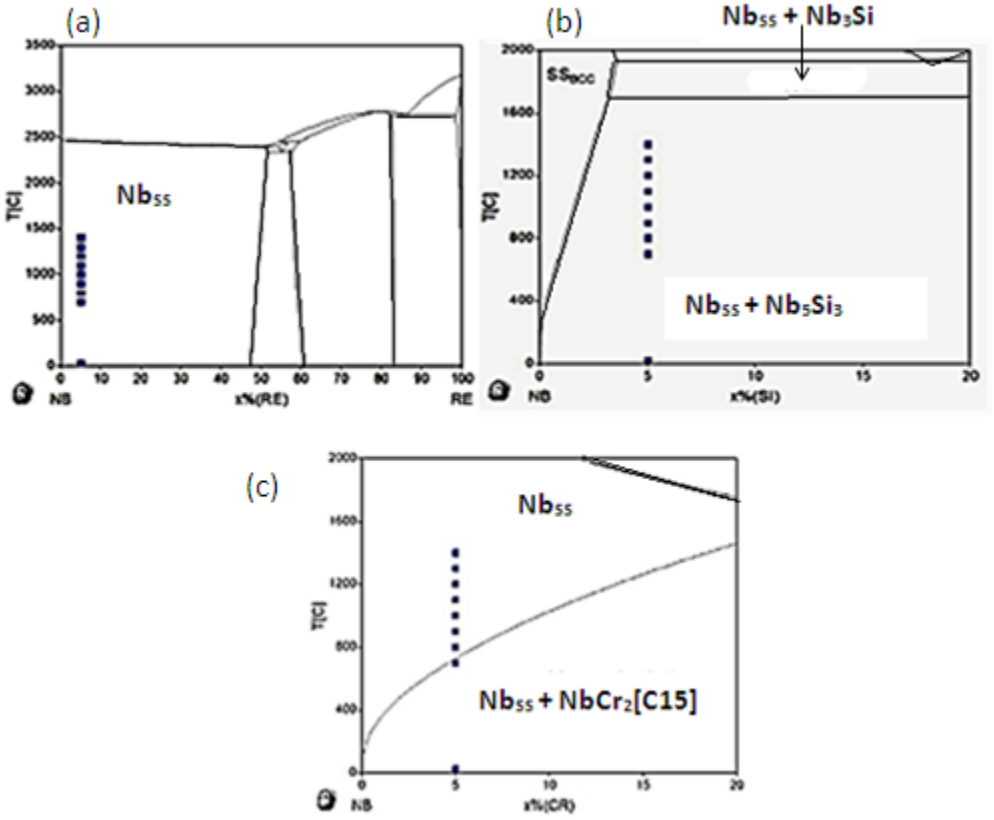


Figure 4.1: Phase Diagrams for Nb-5Re (a), Nb-5Si (b) and Nb-5Cr (c) alloys at RT and temperature-range between 700- 1400$^{o}$C, using PANDAT$^{TM}$.

The as-cast microstructure of Nb-5Re shows a single phase, which is the solid solution, shown in Figure 4.2. The reason no other phase was formed, was due to the high solubility of Re in Nb and thus leading to a single phase.

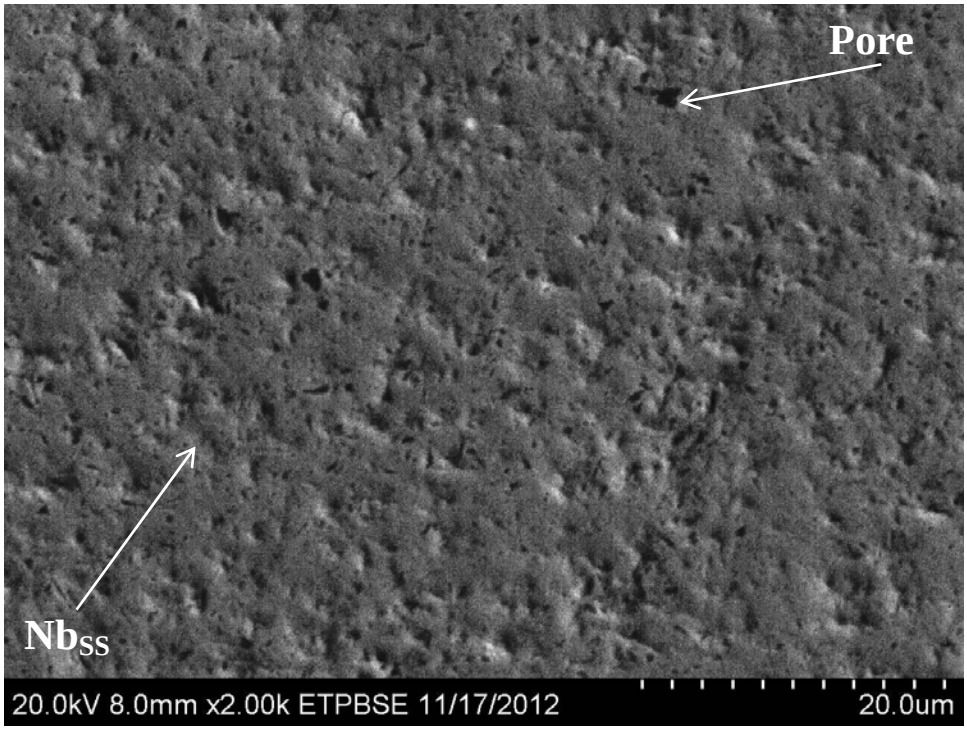

Figure 4.2: SEM image of Nb 5Re alloy

To confirm the formation of the single phase, the alloy was analyzed using TEM. In the first sample (Figure 4.3) TEM image shows formation of only solid solution, as shown in Figure 3(a). The elemental distribution of Nb and Re conclude that there is a larger amount of Nb than Re.

The diffraction pattern (b) shows the BCC arrangement of the atoms, just as Nb, which has BCC structure. The elemental composition shown in (e) quantifies 92.4% of Nb and 7.6% of Re, by EDAX analysis. The EDAX pattern is also included in the Figure 3(d) to show the peaks of Nb and Re, contributing to the formation of the single phase. The SEM, X-ray mapping, elemental distribution and EDAX scans conclude that there has been no other phase formed in this alloy.

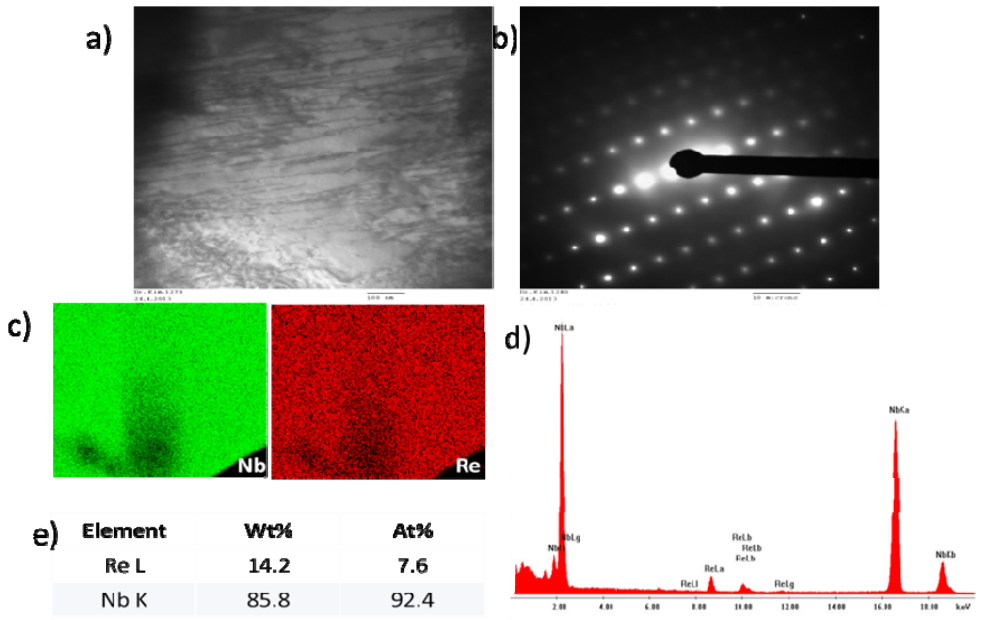


Figure 4.3: TEM image of Nb 5Re alloy

The X-Ray diffraction pattern shown in Figure 4.4 shows the as-cast XRD patterns of pure Nb and Nb-5Re alloy. The patterns for Nb-5Re show the peaks for only Nb. This peak is arranged against the pure Nb peak for analysis purpose. From the peaks it can be understood that the peaks in Nb-5Re alloy, are moved to the right by ½ a degree and also the peak is being widen. While the pure niobium peak forms at $2\theta = 37\text{-}39^{o}$, is more intense. The results can be interpreted that displacement, shortening and broadening of the peak is due to the alloying element which has a higher atomic number (Z=75 for Re).

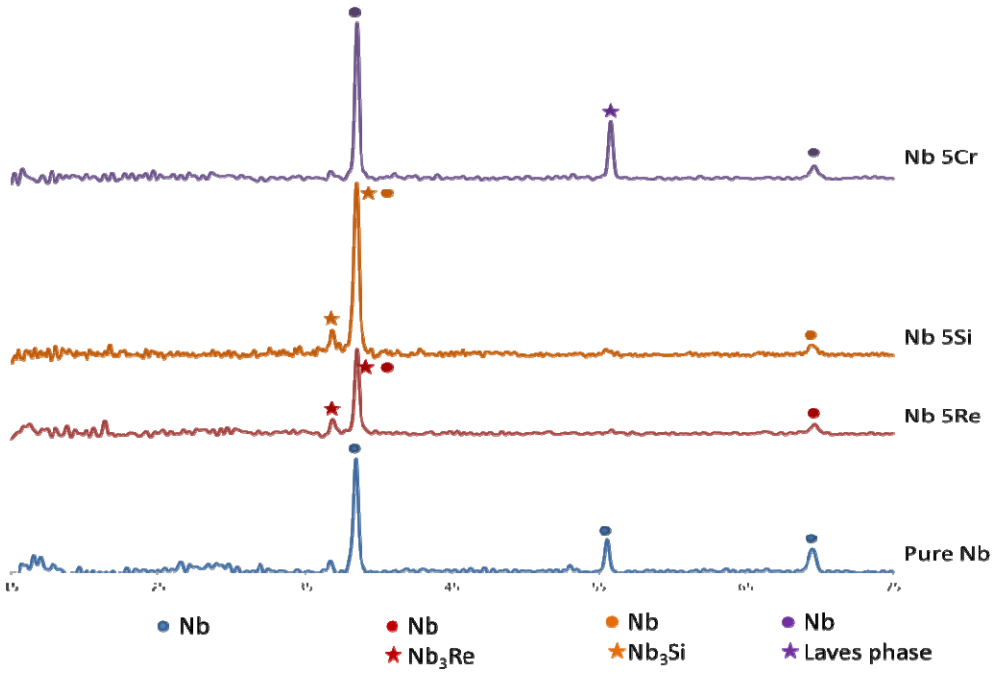


Figure 4.4: XRD date for pure Nb, Nb 5Re, Nb 5Si and Nb 5Cr alloy

In Nb-5Si alloy, the formation of 3, 5 silicides (according to binary phase diagrams from PADNAT$^{TM}$) is substituted by 1, 3 silicides as studied from SEM and XRD data. The microstructure from SEM is shown in Figure 4.5. In the enlarged images (a) show a eutectic between the solid solution and $Nb_3Si$, and (b) shows the $Nb_{SS}$. It can be explained that the deviations between the software and the studied information is due to the fact that the PANDAT$^{TM}$ phase diagrams and isothermal sections are built for equilibrium conditions. However, the phases formed are highly dependent on variables such as temperature, atmosphere, atmospheric pressure and kinetics. Often these deviations from Pandat$^{TM}$ are explained due to such differences. The XRD data, shown in Figure 4.4, shows the peaks for $Nb_3Si$ and $Nb_{SS}$ confirming the data from the SEM.

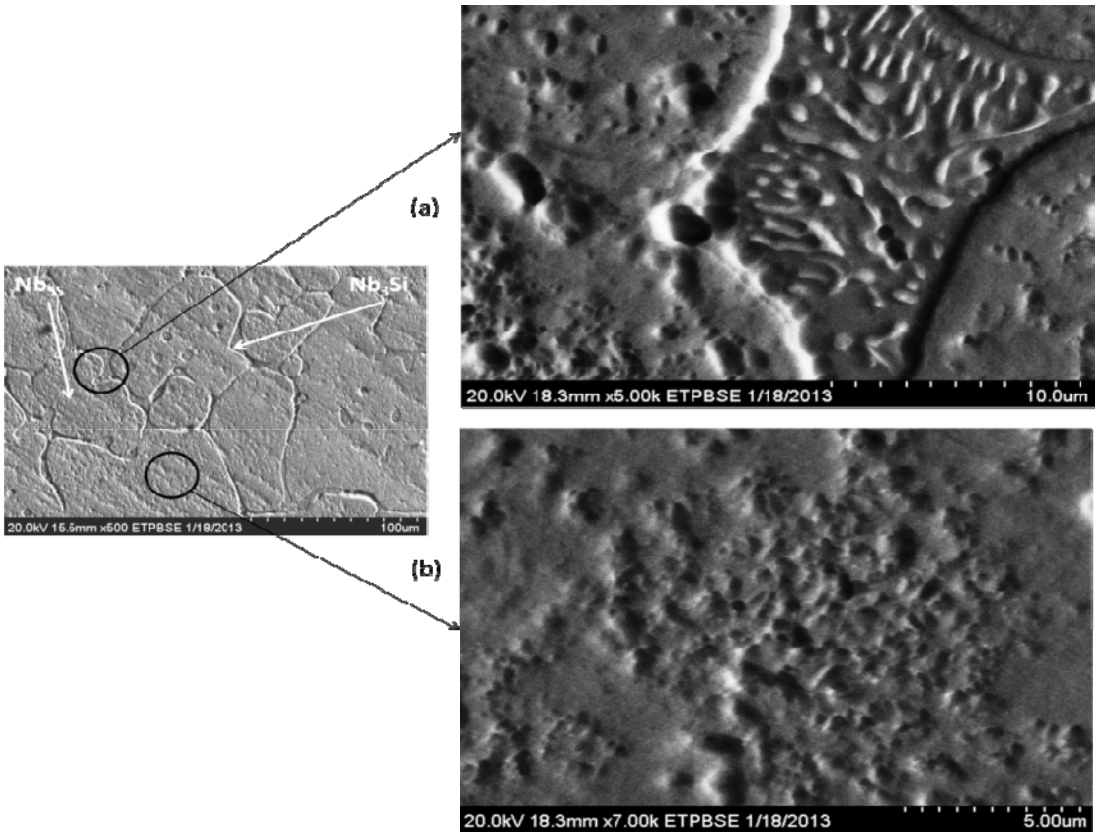

Figure 4.5: SEM image of Nb 5Si alloy, (a) showing the eutectic and (b) showing the solid solution.

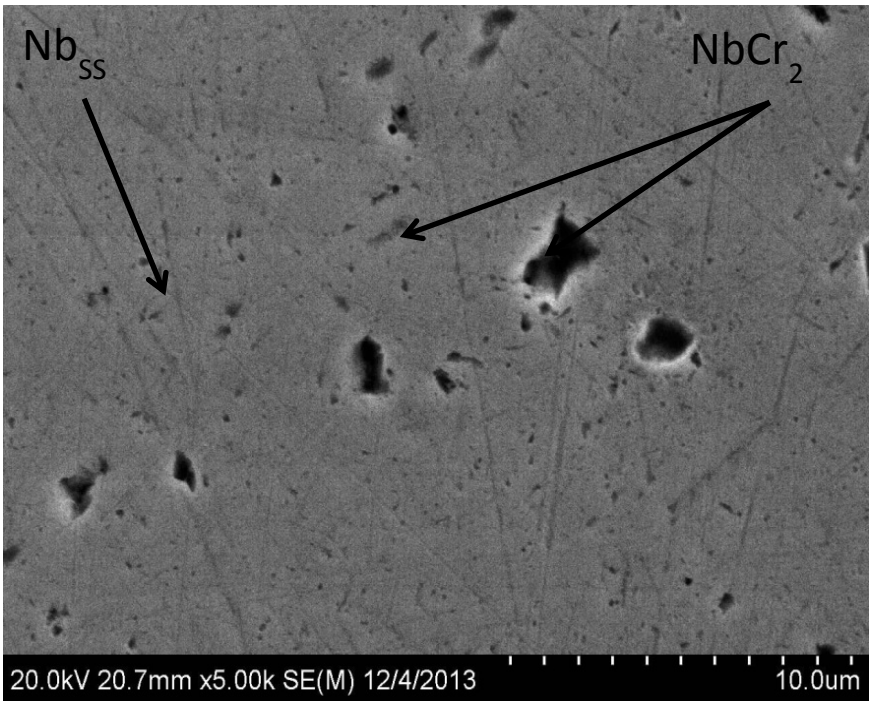

Figure 4.6: SEM image of Nb 5Cr alloy

For the Nb-5Cr binary alloy, phases predicted by PANDAT$^{TM}$ were $Nb_{SS}$ and $NbCr_2$. The SEM/XRD data reveals the same phases. The SEM images shown in Figure 4.6, reveals $Nb_{SS}$ and $NbCr_2$ phases, which is in agreement with the XRD, shown in Figure 4.4.

Considering the PANDAT$^{TM}$ phase diagrams (Figure 4.1) between 700 – 1400$^{o}$C of Nb-5Re, Nb-5Si, Nb-5Cr, explains the formation of phases formed for each alloy with respect to temperature. In each case it is understood that $Nb_{SS}$ is the most dominant phase. To better understand, phase fractions for the alloys were constructed in the temperature range of 700 – 1400$^{o}$C, Figure 4.7. These graphs interpret that the most dominant phase in all the three alloys is the $Nb_{SS,}$ and is constant at 1, throughout the temperature range (700-1400$^{o}$C), for Nb-5Re and Nb-5Cr. For Nb-5Si alloy there is an increase of the fraction of $Nb_{SS}$, gradually increasing from 0.89 to 0.95 with in the temperature range. Also the phase fraction for Nb-5Si shows a gradual decrease in 3, 5 silicide. For Nb-5Cr alloy, the phase fractions show that $NbCr_2$ is not formed beyond 700$^{o}$C.Computational information, such as this, is very helpful when alloys are subjected to any kind of heat-treatments, therefore estimation can be made.

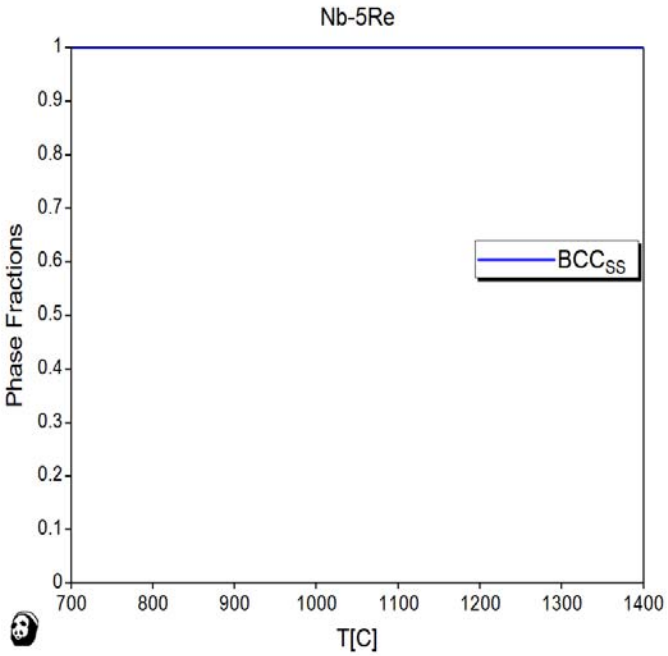

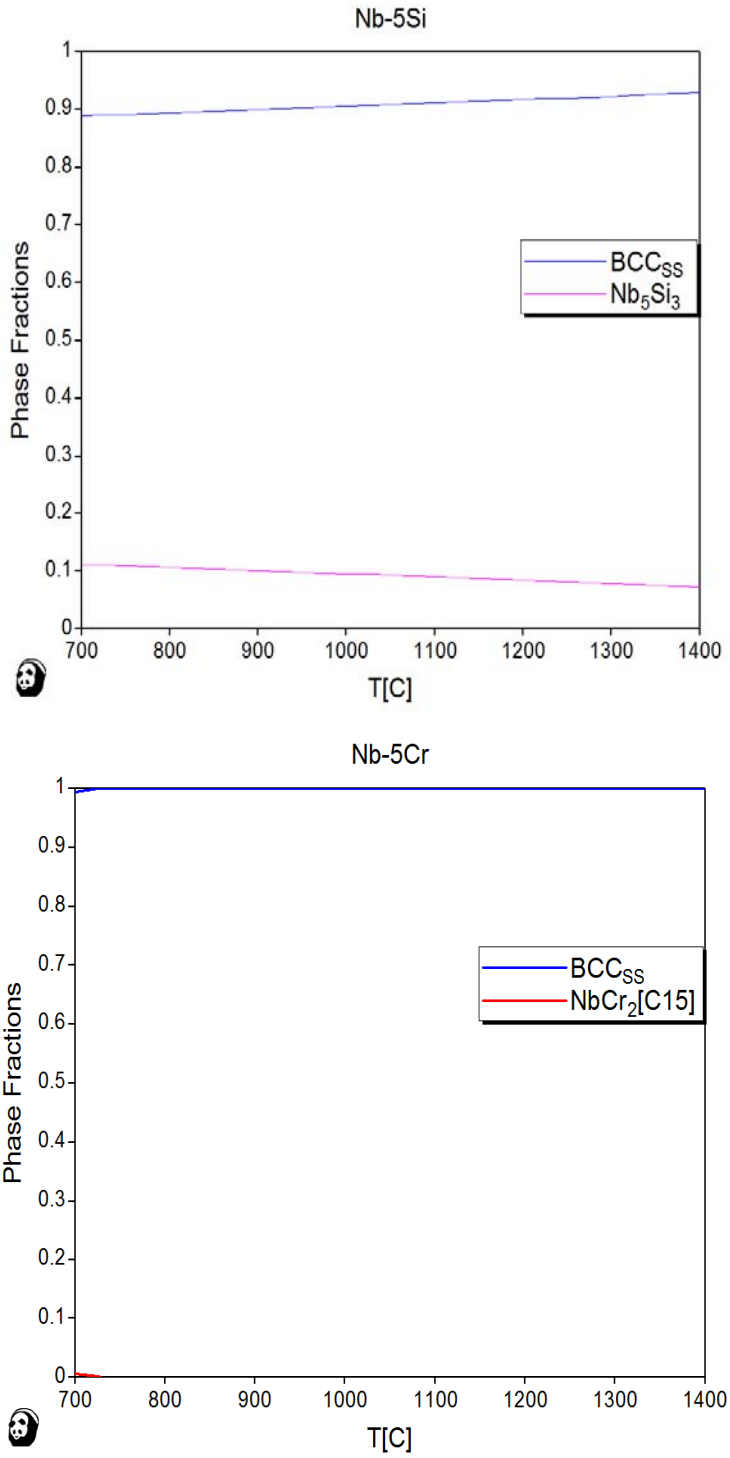


Figure 4.7: Phase fractions for Nb 5Re, Nb 5Si, Nb 5Cr

Although the phase diagrams from PANDAT$^{TM}$ can provide us with decent information on the relevance of phase formation, comprehending them with combined information (from SEM, XRD, EDS) helps often to make the analysis more logical and explainable.

## 4.2 Ternary alloys

**4.2.1 Nb-5Re-5Si:** Due to the lack of literature on the Nb-Re-Si ternary system, combined studies of the individual phase diagrams of Nb-Si and Re-Si was considered. These studies clearly interpret that there is a possibility of the formation of rhenium-silicides $ReSi_2$, $ReSi_{1.8,}$ $Re_2Si$, $Nb_5Si_3$ along with $Nb_{SS}$. [2,8]

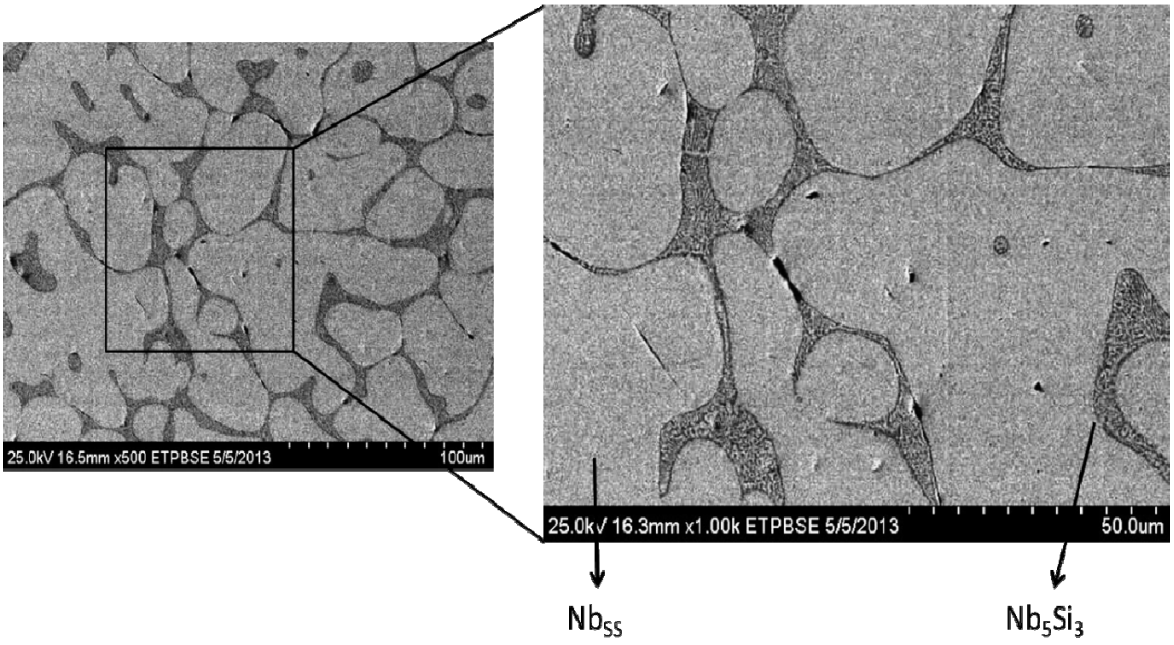


Figure 4.8: SEM image of Nb 5Re 5Si alloy

The SEM and XRD analysis reveal the formation of $Nb_{SS}$, $Nb_5Si_{3.}$ There is also a eutectic between the solid solution and $Nb_5Si_3$. The SEM image of Nb-5Re-5Si is shown in Figure 4.8. It is understood that Re has promoted the formation of the 3,5 silicides, unlike in the binary alloys Nb-5Si, where 1,3 silicide was observed. The 3,5 silicides are more desirable due to its higher melting temperature.

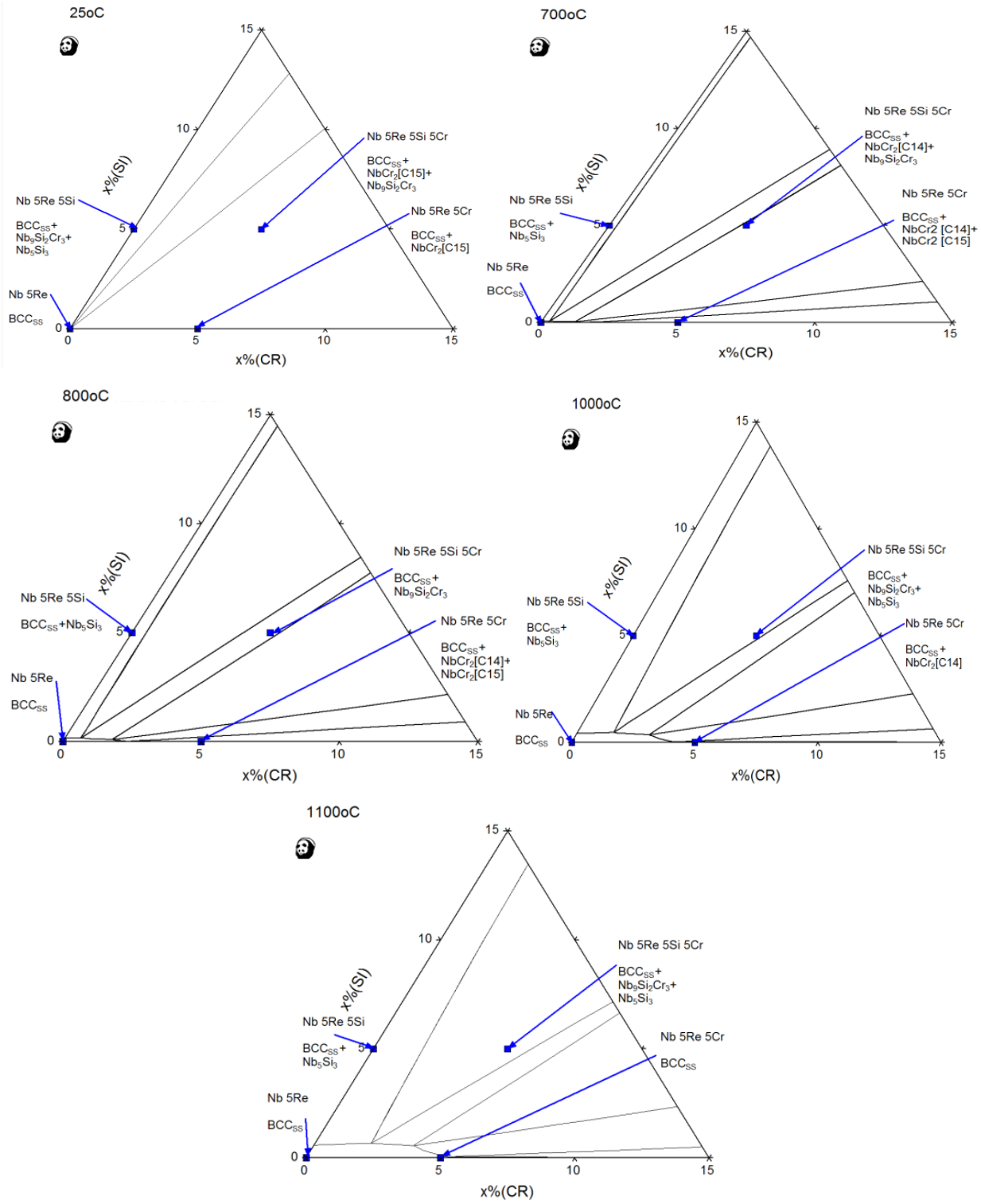


Figure 4.9: Isothermal sections for Nb 5Re, Nb 5Re 5Si, Nb 5Re 5Cr and Nb 5Re 5Si 5Cr, at RT, 700, 800, 1000 and 1100$^{o}$C.

However, PANDAT isothermal section for this alloy reveals the formation of $Nb_{SS}$, $Nb_9Si_2Cr_3$ and $Nb_5Si_3$, shown in Figure 4.9. The deviations are explained as follows:

(a) $Nb_9Si_2Cr_3$ is considered to form at higher temperatures along with $Nb_5Si_3$, and as cooling occurs the formation of $Nb_5Si_3$ becomes more dominant.

(b) Another critical issue could be the insufficient times of cooling. If the alloy were to be given a significant time, and under equilibrium conditions $Nb_9Si_2Cr_3$ could have been a dominant phase as PANDAT$^{TM}$ depicts.

The phase fraction calculations of the alloy show that at temperatures starting 700$^{o}$C, the amounts of $Nb_5Si_3$ is decreased as $Nb_{SS}$ increase, as shown in Figure 4.10. From this we can understand that although there are other phases in the alloy, the solid solution is the most prominent phase, because of the high content of Nb.

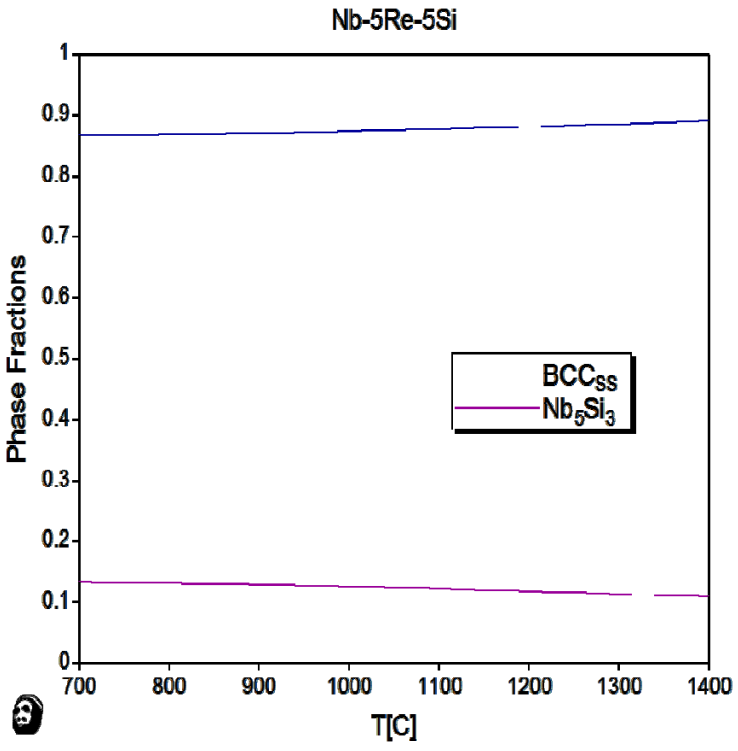


Figure 4.10: Phase fractions for Nb-5Re-5Si

### 4.2.2 Ternary alloys - Nb-5Re-5Cr:

Previously constructed phase diagrams from other sources have considered the studies with Re and Cr concentrations greater than 40 at.%, for annealing. The structures formed were $NbCr_2$ [C14 and C15] along with $Cr_2Re_3$. However lower concentrations of either Re or Cr were not analyzed. [10,11,12]

The microstructures for Nb 5Re 5Cr reveal the formation of Laves phase (C15) and Nb-solid solution, Figure 4.11. The isothermal sections constructed for this alloy depicts formation of $Nb_{SS}$ and $NbCr_2$ [C15], Figure 4.9. Information from Pandat$^{TM}$, SEM/XRD reveals similar results. $ReCr_2$ was also detected from the SEM images.

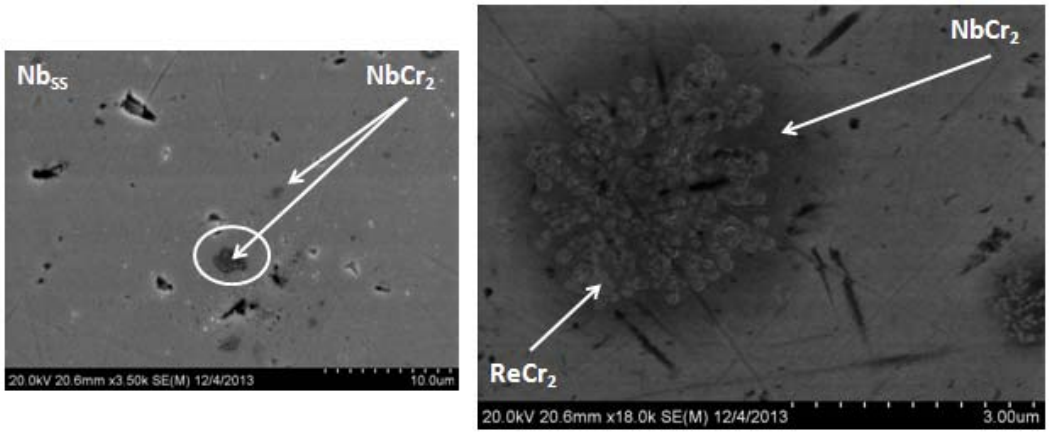


Figure 4.11: SEM image of Nb 5Re 5Cr alloy

From the phase fraction variations for this alloy, it can be understood that at elevated temperatures above 1100$^{o}$C, the formation of $NbCr_2$ is negligible. This is compensated with the alloy enrichment with solid solution. The phase fractions of Nb-5Re-5Cr are shown in 4.12. The XRD data is shown in Figure 4.13.

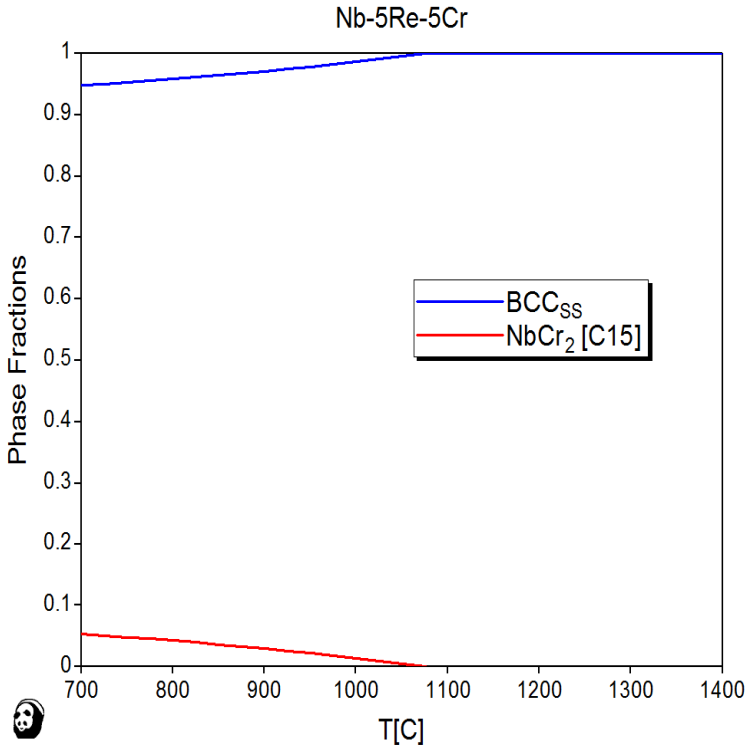


Figure 4.12: Phase fractions for Nb-5Re-5Cr

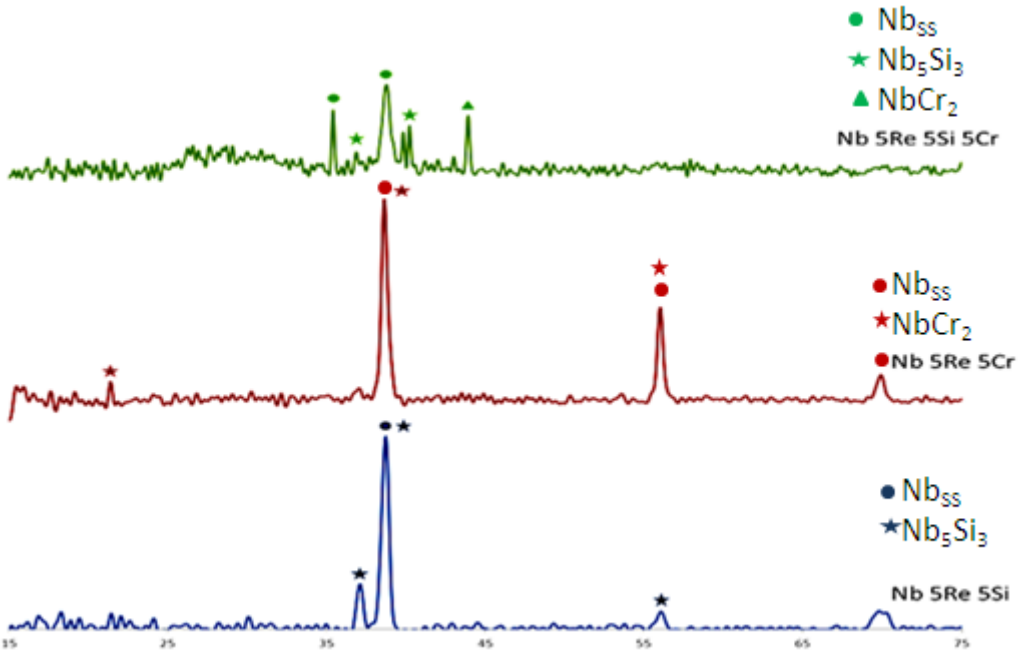


Figure 4.13: XRD date plots for Nb-5Re-5Si, Nb-5Re-5Cr and Nb-5Re-5Si-5Cr alloy

**4.3 Quaternary alloy – Nb-5Re-5Si-5Cr:** From the isothermal sections, the phases formed are $Nb_{SS}$, $Nb_9Si_2Cr_3$ and $NbCr_2$ [C15], Figure 4.9. However the studies form the SEM (Figure 4.14) and XRD (Figure 4.13) show the formation of $Nb_5Si_3$, Laves phase and $Nb_{SS}$.

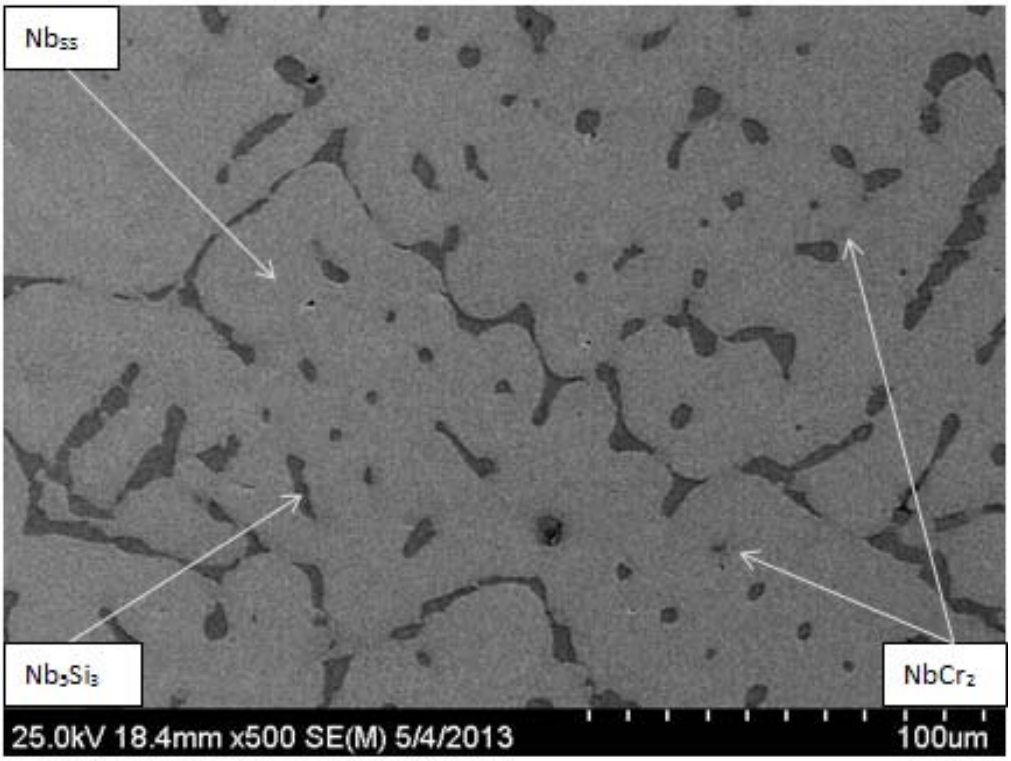

Figure 4.14: SEM image Nb 5Re 5Si 5Cr alloy

To understand this deviation a phase fraction vs temperature graph was constructed between 500 – 2500$^{o}$C, to analyses the phases formed beyond this study limits, shown in Figure 15. In this construction, the crucial points to be noted are:

(a) The dominant phase constituent is $Nb_{SS}$.

(b) Due to the alloy cooling under non-equilibrium conditions, the solidification reactions after the alloys had completely formed into a solid (below 1800$^{o}$C); and therefore there is insufficient time to transform into an additional phase, which is $Nb_9Si_2Cr_3$ in the alloy microstructure.

(c) The significant drop in the $Nb_9Si_2Cr_3$ phase occurs between temperature ranges of 1000 – 1500°C, beginning at 1000°C. This explains the missing phase in this study.

(d) If these alloys (Nb 5Re 5Si and Nb 5Re 5Si 5Cr) were held for a significant period of time, for example at 1000°C, the microstructure would transform to exhibit $Nb_{SS,}$ the 3, 5 silicide and the 9-3-2 silicide in their equilibrium fractions).

Apart from these main reasons few other worth mentioning are, the cooling rates for the diffusion to occur to form the equilibrium phases and low amounts of Re.

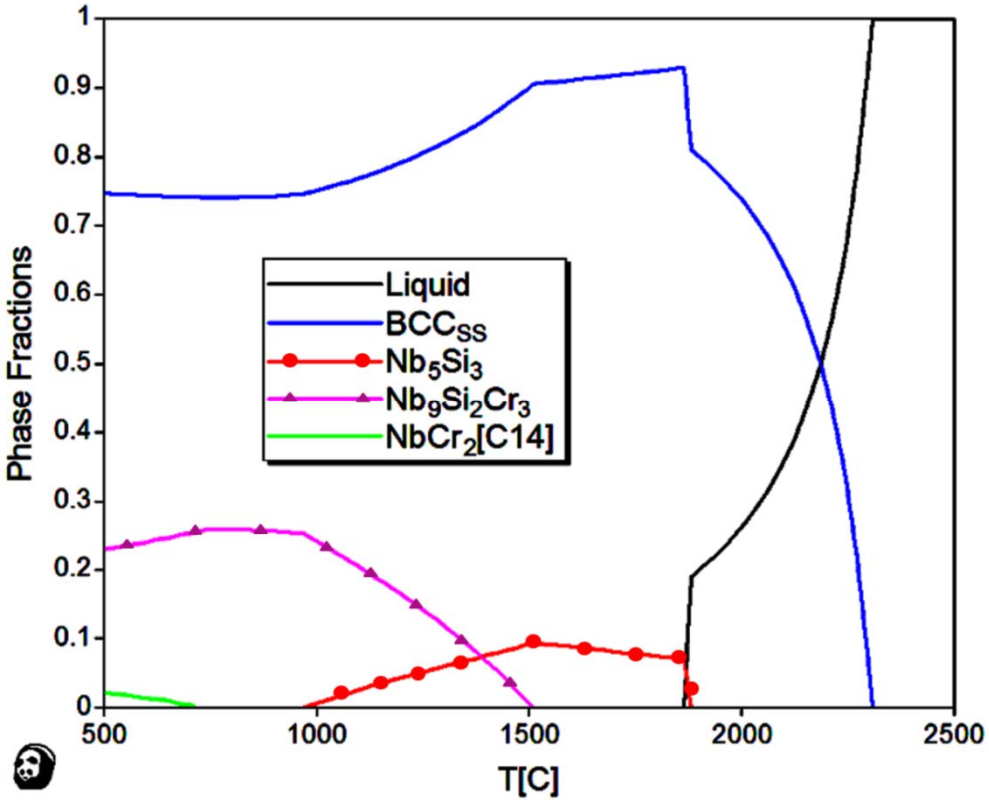


Figure 4.15: Phase fractions for Nb 5Re 5Si 5Cr between 500 – 2000°C.

**4.4 Oxidation Results for binary, ternary and quaternary alloys:**

The curves in Figure 16 (a, b, c) show the weight gain per unit area as a function oxidation temperature for binary, ternary and quaternary alloys. The curves for binary alloys 16 (a) show that the highest weight loss was recorded for Nb-5Cr alloy. This is due to the formation

of Rhenium and Chromium volatile oxides. Rhenium forms $ReO_2$ and Chromium forms $Cr_2O_3$, which are volatile between 800 and 1000°C. Nb-5Re shows a weight loss between 800 and 900°C. At a 1000°C, rhenium form $Re_3O_{10}$, which is not a volatile oxide and thus contributes to the weight of the oxide product. Considering the Nb-5Si curve, there is very little variation in terms of weight gain or weight loss.

The curves for ternary alloy 16 (b) shows that the highest weight loss was recorded for Nb-5Re-5Si alloy. The weight gain was observed for Nb-5Re-5Cr alloy. Although both volatile oxides are formed, there is still a weight gain for this alloy. This is because there are additional oxides which are formed, that is β-$Nb_2O_5$ and $CrNbO_4$, which significantly add to the weight of the alloy. For the quaternary alloy (curve shown in 16(c)), depicts the highest weight gain at 800oC. This behavior is due to the formation of orthorhombic $Nb_2O_5$ along with $CrNbO_4$. All the samples suffered pest oxidation at all temperatures. (700-1000°C). A list of oxides formed for all the alloys considered in this study have been summarized in Table 1, as detected by XRD.

A)

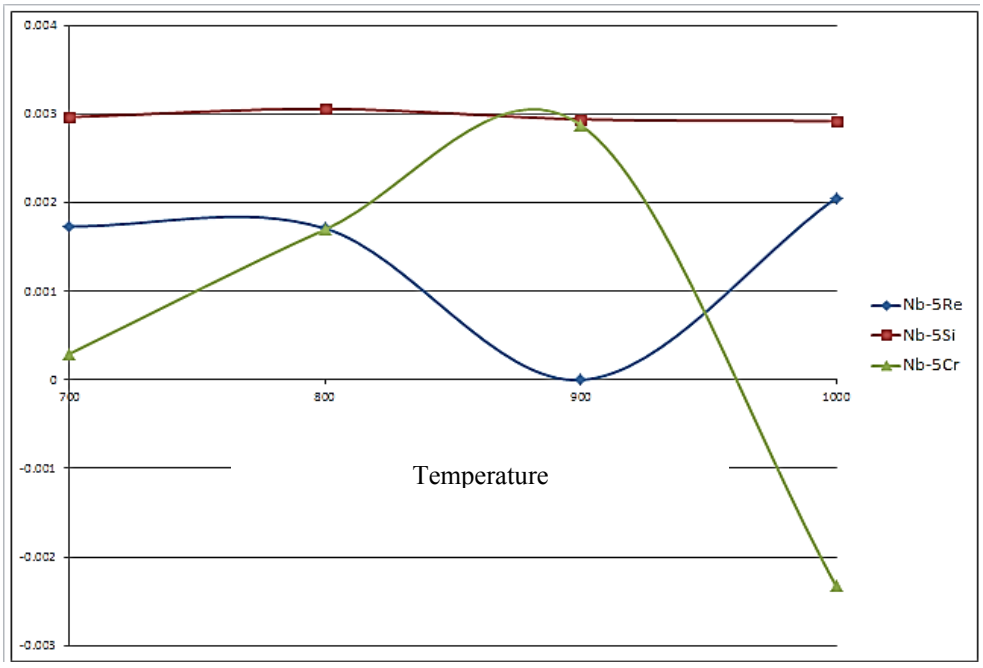

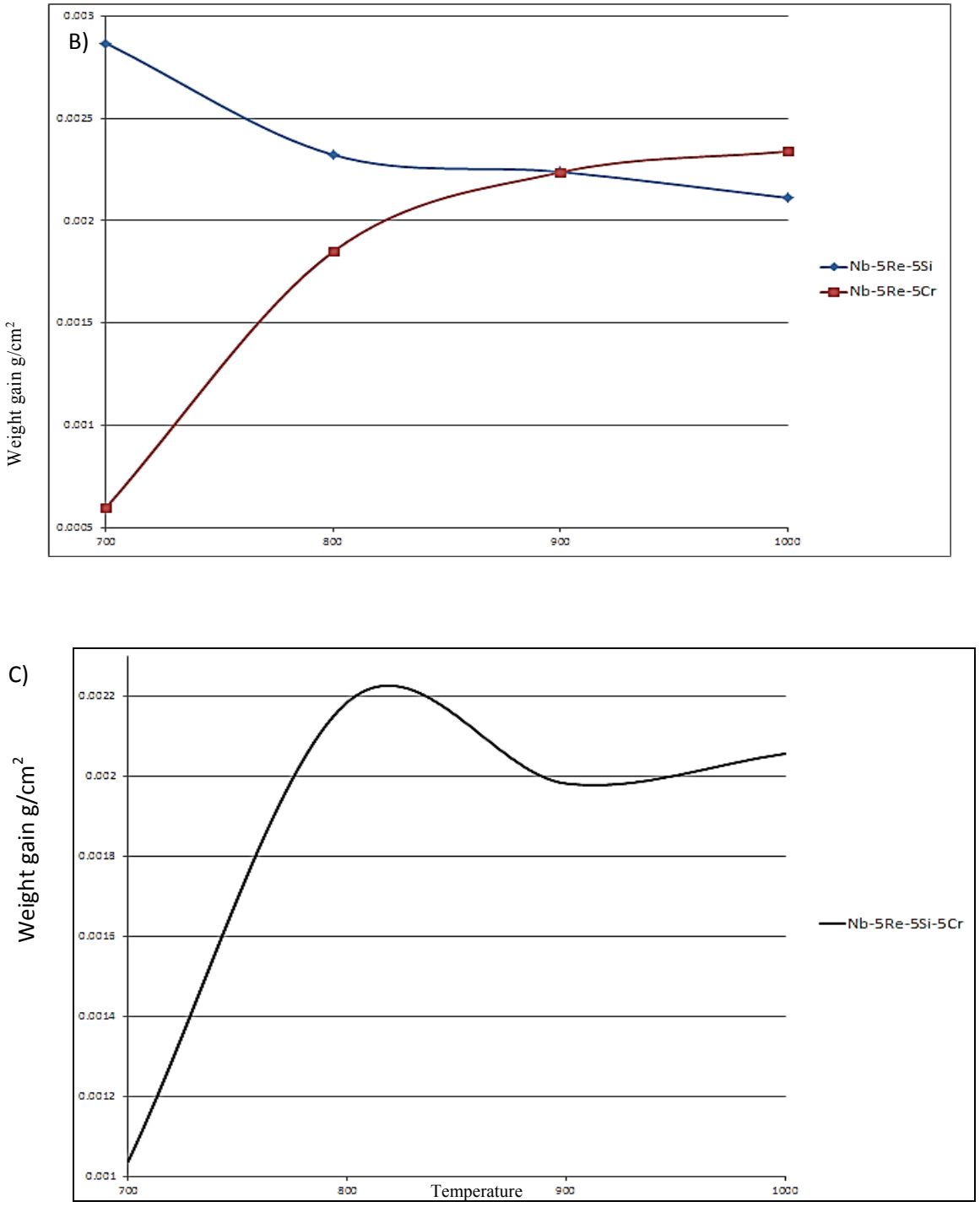


Figure 4.16: Wt. gain/loss per unit area as a function of temperature – For Binary alloys, Ternary alloys and quaternary alloy.

## 4.5 Nb-15Re-15Si-10Cr-20Al

**4.5.1 As-cast:** Pandat$^{TM,}$ thermodynamic modeling software, developed by CompuTherm LLC, was used to study the isothermal sections for temperature range used in this study. The isothermal sections were calculated by holding the Rhenium and Silicon content at 15 atomic percentages shown in Figure 4.17.

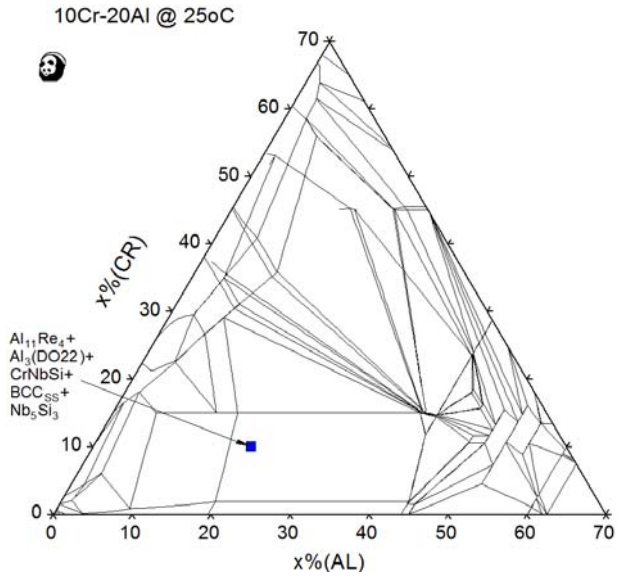


Figure 4.17: Calculated isothermal section of Nb- Re-Si-Cr-Al using Pandat$^{TM}$

Calculated isothermal section reveals the formation of phases as: $BCC_{SS,}$ $Nb_5Si_{3,}$ CrNbSi, $Al_3$ (Do22) and $Al_{11}Re_{4.}$ Both Al- compounds are highly desirable due to their high temperature and good oxidation resistant capabilities. $Al_3$ (Do22) is a niobium based tri-aluminide with a tetragonal Do22 crystal structures and are calculated for $MAl_3$ compounds, where M is a group III, IV or V transition metal. [78]

The BSE as-cast microstructure of the alloy reveals the formation of $BCC_{SS}$, $Nb_5Si_3$and $Al_3Nb$, shown in Figure 4.18. The Laves phase was not formed as expected. The most obvious reason can be that the formation of tri-aluminide has hindered the process of formation of the

Laves phase. XRD data for the alloy also depict the formation of solid solution, $Nb_5Si_3$ and Nb tri-aluminide phases.

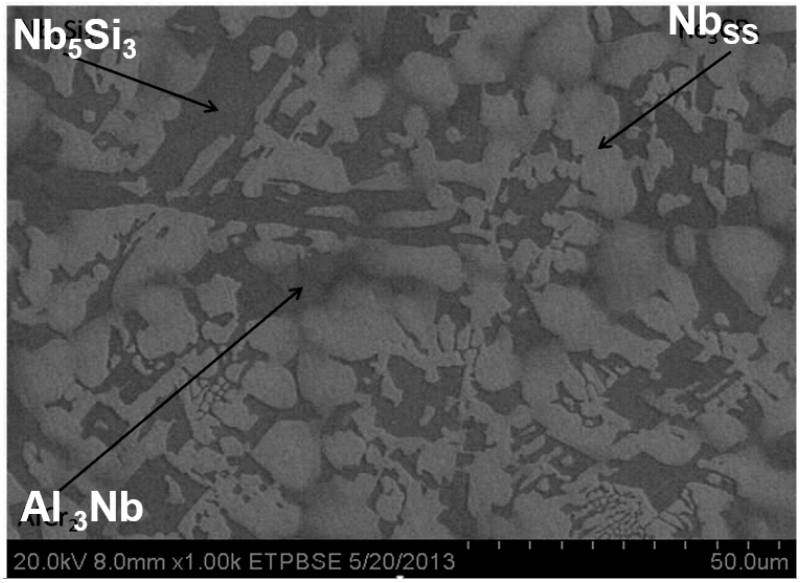


Figure 4.18: BSE micrograph of the alloy Nb-15Re-15Si-10Cr-20Al

**4.5.2 Evolution of Microstructure between temperature range 700 – 1400$^o$C: (**Figure 4.19)

At 700$^o$C, the phases from the as-cast continue, which are $BCC_{SS}$, $Nb_5Si_3$and $Al_3Nb$. The samples when subjected to oxidation produced a lot of cracks. This has enabled the flow of oxygen into the metal and has results in the formation of $Nb_2O_5$, $Al_2O_3$ and $SiO_2$, internally, amongst the phases. Thus we can conclude that internal oxidation has started at a very early stage. An elemental X-ray mapping is shown in Figure 4.20 to confirm internal oxidation. At 800$^o$C, the phase were observed to remain the same, however a eutectic between the solid solution and the 3,5 silicides was noticed and is shown in the Figure 4.19. Internal oxidation is continued at 800$^o$C.

At 900$^o$C, the metal suffered pest oxidation. It is important to mention the porosity of the alloy, and thus the rapid oxidation has led to pesting. Internal oxidation, followed by pesting has produced orthorhombic form of $Nb_2O_5$ and $CrNbO_4$ along with other oxides such as $Al_2O_3$ and

$SiO_2$. All these oxides were analyzed by XRD, refer Figure 4.8. No metal was found to analyze the formation of phases at 900°C. But an estimation can be made considering the Pandat™ isothermal section at 900°C, the phases formed were $BCC_{SS,}$ $Nb_5Si_{3,}$ CrNbSi, $Al_3$(Do22), same as 700°C. No to forget that there is a very high probability, that the phases depicted through SEM and EDS would have been the same (that if there was any metal left), which are $BCC_{SS}$, $Nb_5Si_3$and $Al_3Nb$.

Starting at 1000°C, the microstructure reveals $Nb_5Si_3$, $Al_3Nb$, $Nb_{SS}$ phases. In addition, cracks were observed more intensely, at the corner of the metal eventually vanishing towards the center of the metal. It can be said that the cracks produced oxidation, forming $CrNbO_{4,}$ $AlNbO_4$, $Al_2O_{3,}$ and $SiO_2$ decreasing the oxidation kinetics. The formation of these oxides has been depicted by XRD, which confirms the same. At 1100 and 1200°C, the micrographs show eutectic regions of $Nb_{SS}$ and $Nb_5Si_3$. The phases formed between 1100-1400°C are the same. At 1300°C, the cracks are minimized to a large extent, when compared to the cracks and pores formed at previous temperatures. The alloys at temperature 1100 – 1400°C suffered no spallation, as the formation of oxides has hindered the flow of oxygen into the metal, shown in Figure 4.3.

At 1400°C, the microstructure constituents were $Nb_5Si_3$, $Al_3Nb$, $Nb_{SS.}$ Also revealed were the formation of oxides (due to internal oxidation) $CrNbO_4$, $Nb_2O_5$, $Al_2O_3$, and $SiO_2$. The oxide grew in to the sample along the cracks, almost closing the cracks. Although the porosity could not be eliminated most of the pores were filled by $Al_2O_3$ and $SiO_2$. Figure 4.3. Thus oxide rich intermediate layer was produced.

Comparing the alloy at different temperatures (in terms of internal oxidation), it was observed that oxidation was intense at 700, 900 and 1400°C, from the microscopy and weight gain data analysis, which is discussed further in this paper.

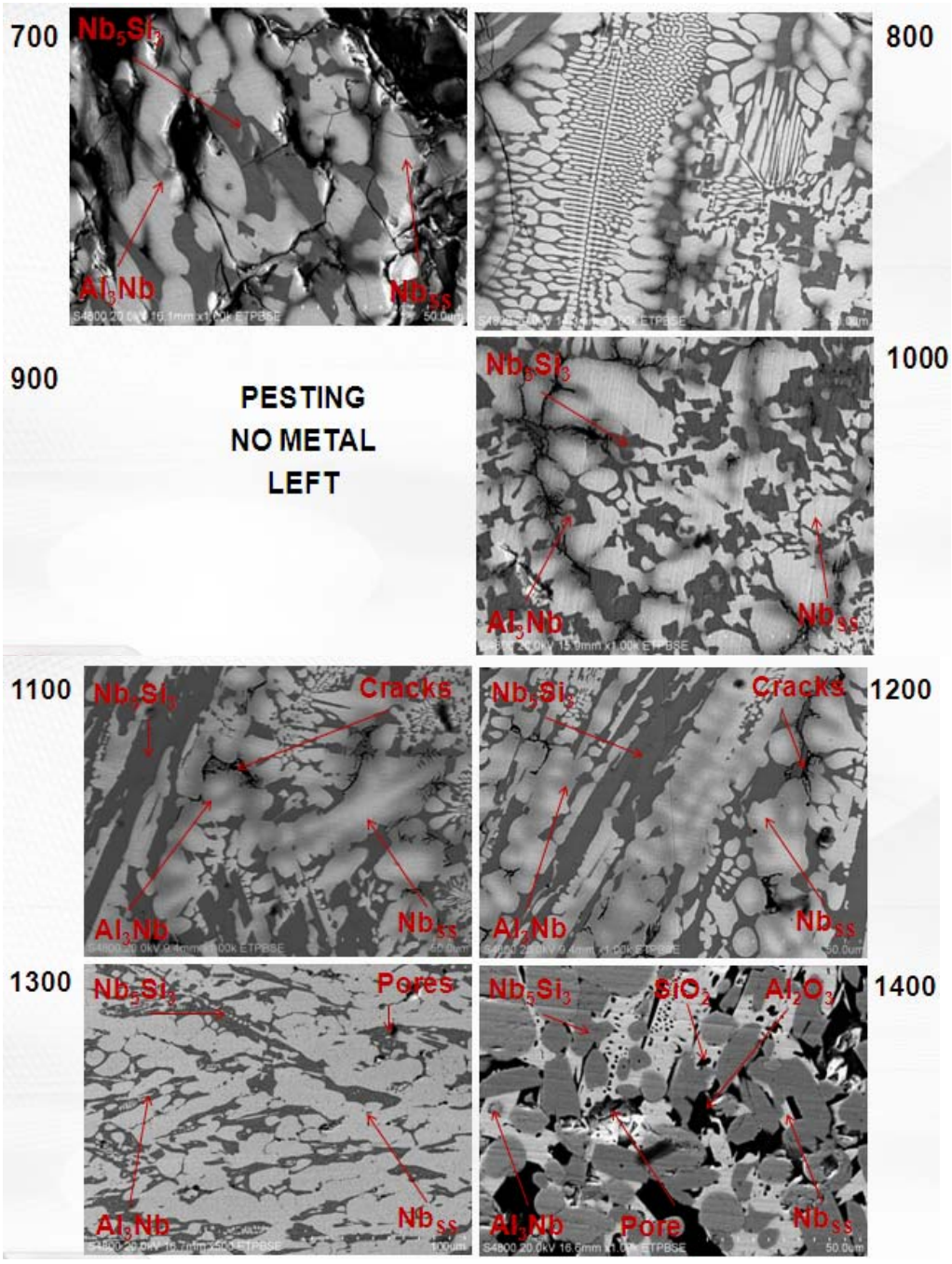


Figure 4.19: Micro structures of remaining metal 700 - 1400°C

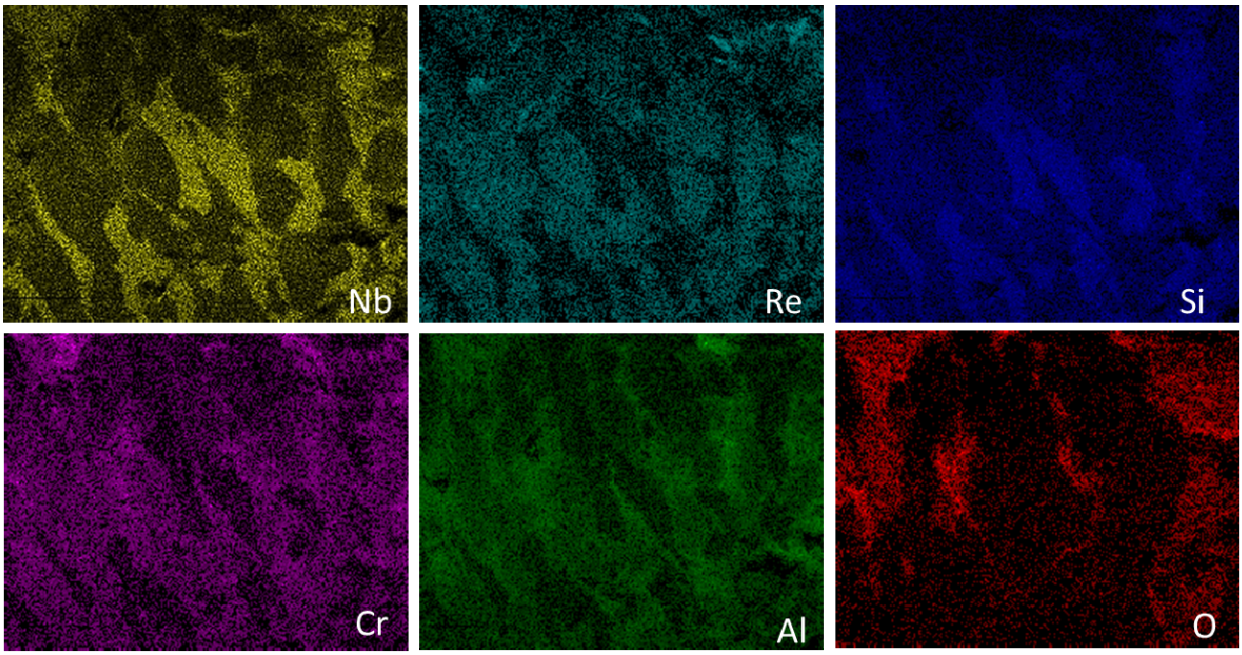


Figure 4.20: Elemental X-Ray mapping of the internal oxidation at 700°C, showing formation of $Nb_2O_5$, $Al_2O_3$ and $SiO_2$.

The variations in the calculation of phases by Pandat™, has changed from $BCC_{SS,}$ $Nb_5Si_{3,}$ CrNbSi, $Al_3$ (Do22) at 700°C to $BCC_{SS,}$ $Nb_5Si_3$ at 1400°C. The phases formed between 700 and 1300°C are the same phases as the phases formed at 700°C, shown in Figure 4.21.

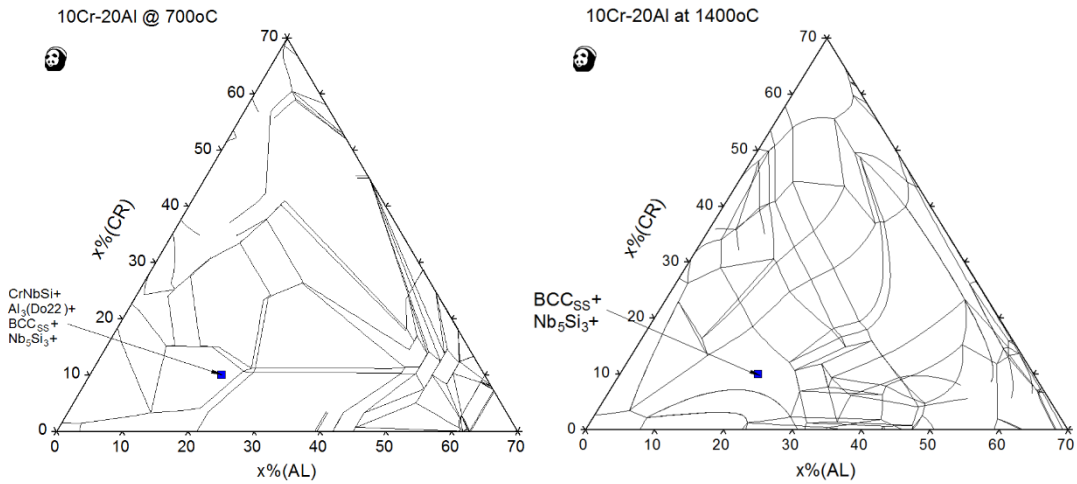


Figure 4.21: Isothermal sections of Nb- Re-Si-Cr-Al at 700 and 1400°C, where change in the calculations were noticed.

### 4.5.3 Internal Oxidation of the alloy between 700-1400$^{o}$C:

The internal oxidation can be attributed to the initial porosity of the alloy. This has developed a noticeable increase in the kinetics of oxidation. At 700$^{o}$C, large amounts of cracks were observed and therefore the flow of oxygen into the cracks has produced internal oxidation forming oxides such as $Nb_2O_5$, $Al_2O_3$ and $SiO_2$. A combination of $Al_2O_3$ and $SiO_2$ oxides are preferable to lower the oxidation kinetics, as these oxides individually act as protective oxide layer and are highly considerable. In this case, the alloys have produced large cracks causing the metal to split into many pieces. At 800$^{o}$C, the effect of internal oxidation was very similar and the oxides formed were $Nb_2O_5$, $CrNbO_4$, $Al_2O_3$ and $SiO_2$. At 900$^{o}$C, the alloy has suffered pesting resulting in powdered oxide. The formation of the cracks at 700 and 800$^{o}$C, clearly explains that the resultant oxide product could be a powder form. The formation of orthorhombic form $Nb_2O_5$ adds to the highest amount of weight gain for this alloy. The internal oxidation for 700, 1000 and 1400$^{o}$C is shown in Figure 4.22.

Starting from 1100$^{o}$C, the cracks are found to be much finer, when compared to the cracks at 700,800 and 1000$^{o}$C. The internal oxidation has been minimized for the same reason. At 1400$^{o}$C the formation of $Al_2O_3$ and $SiO_2$ were found to be formed in a discontinuous format, in the intermediate oxide layer, shown in 4.23 (A). The elemental X-ray mapping is the same is shown in 4.23(B). The alloy was found to be in one piece without any spallation. The discontinuous layer has been definitely advantageous for two reasons. Firstly, the negative weight loss and less loss of metal. The metal remaining after the oxidation process was approximately 70% and without any spalling.

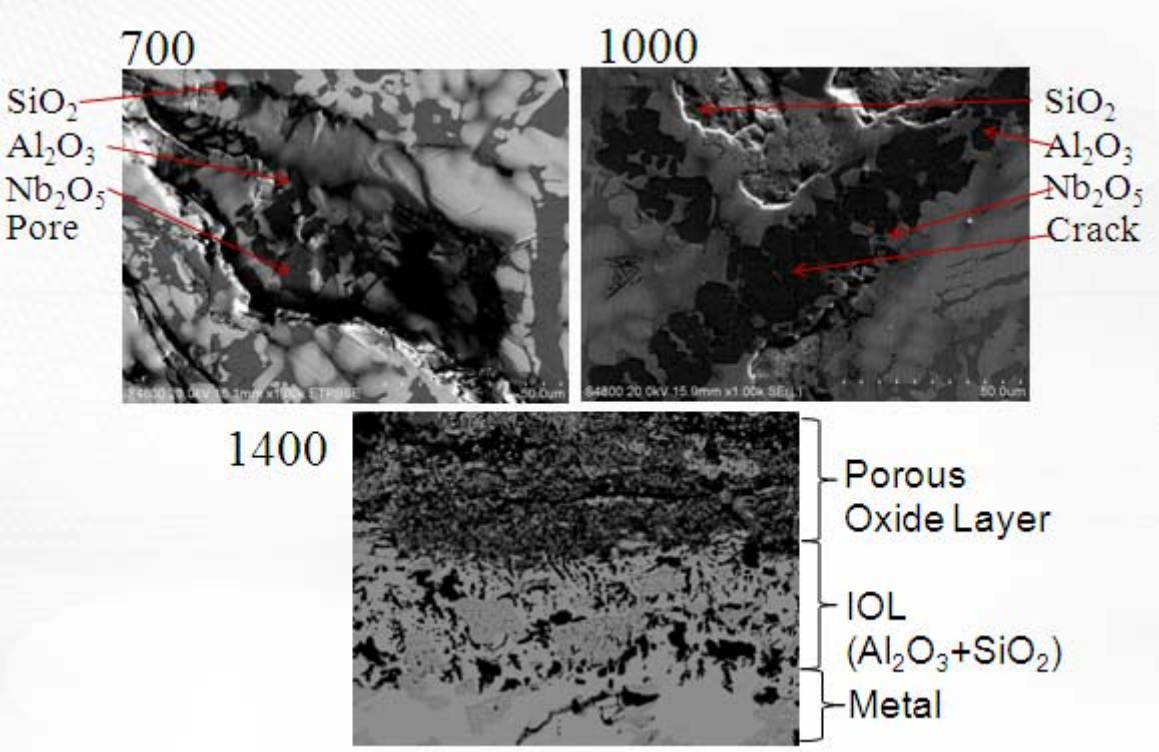


Figure 4.22: Micro structures of oxide-metal interfaces of the alloy at 700°C, 1000°C and 1400°C

A)

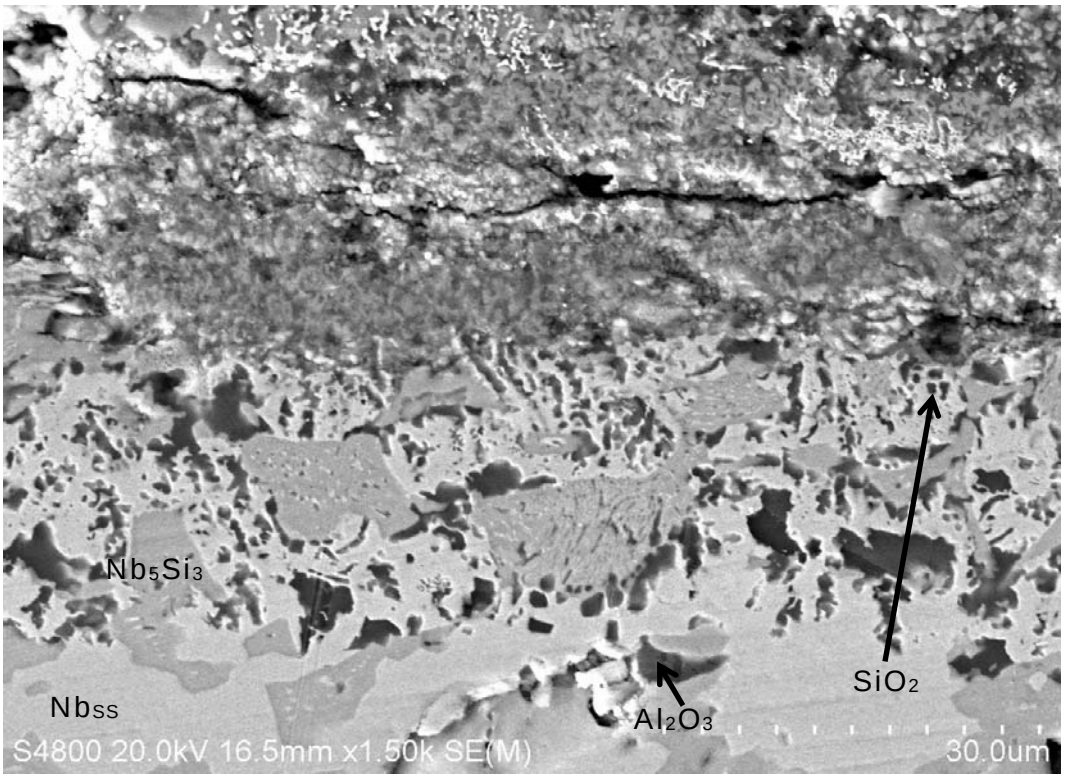

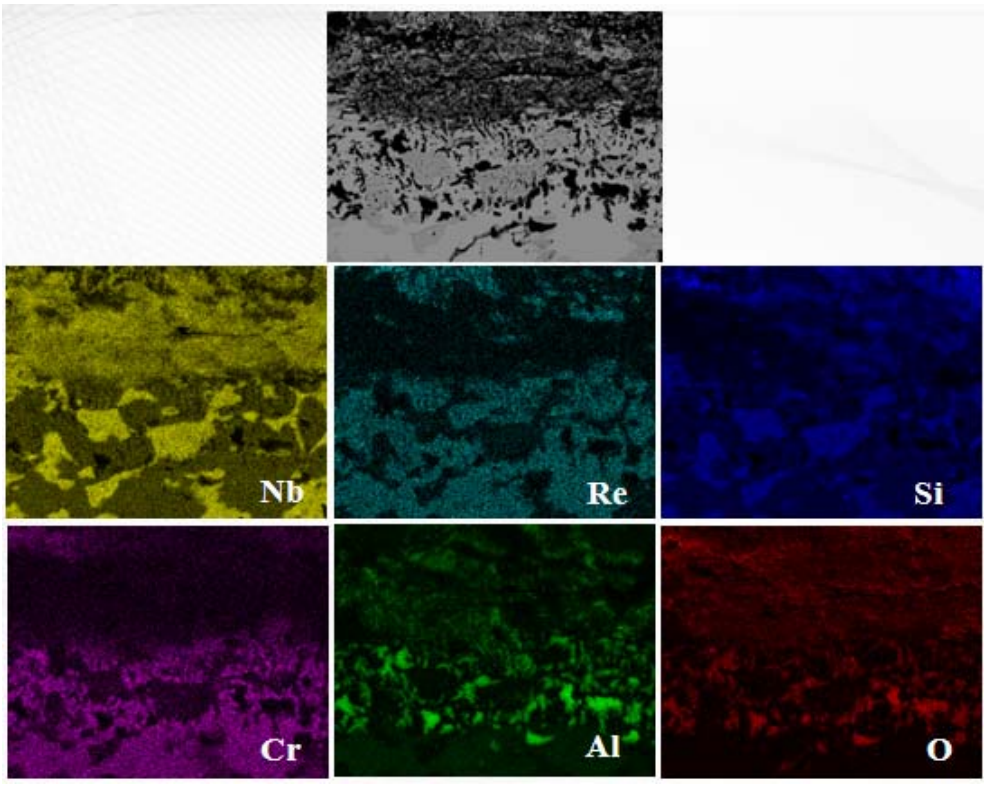

Figure 4.23: (A) shows the IOL of the alloy at 1400$^{o}$C and (B) shows the Elemental X-Ray mapping of the IOL at 1400$^{o}$C, showing formation of an alternation $Al_2O_3$ and $SiO_2$.

### 4.5.4 Oxide Surface analysis:

Observing the oxide surfaces, the light grey regions indicate $Nb_2O_5$ and the dark grey regions $CrNbO_4$. The very dark regions (pitch black) indicate $SiO_2$/ $Al_2O_3$ or a pore. It is very difficult to identify the difference between these three. However, when a oxide is formed ($Al_2O_3$/$SiO_2$) the dark region forms a concave surface, indicating the formation of an oxide. It is understood that the porosity in the oxide layer is maximized at 700 and 1400$^{o}$C. Although the oxides formed at all temperatures (700-1400$^{o}$C) were same ($Nb_2O_5$, $CrNbO_4$, $Al_2O_3$, $SiO_2$), $CrNbO_4$ was observed to increase between the 1000 - 1400$^{o}$C. This can be concluded because of the limited formation of cracks and less penetration of oxygen into the metal, causing the product to split in to many segments. Because, $CrNbO_4$, $SiO_2$ and $Al_2O_3$ help in lowering the kinetics of oxidation, by formation a barrier between the environment and the metal. Although a Cr oxide

layer would have been advantageous and was expected to form ( as Cr of the outward diffusion), none of the cr-oxides were formed. Cr has helped in the formation of $CrNbO_4$ in this alloy, at all temperatures.

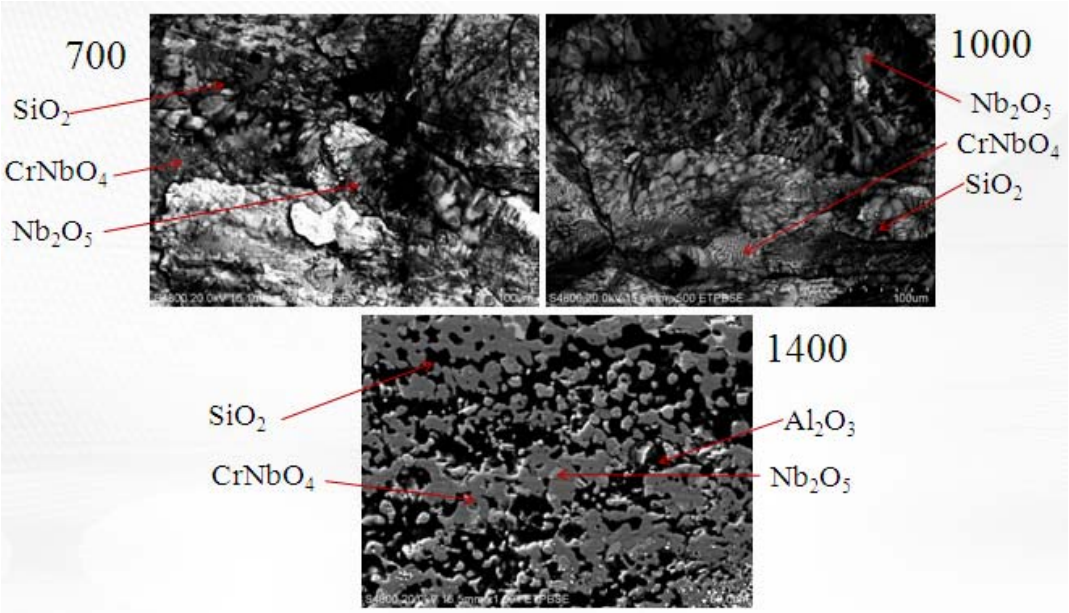


Figure 4.24: Micro structures of oxide surface at 700°C, 1000°C and 1400°C

The oxides formed between 1100-1300$^{o}$C were $Nb_2O_5$, $CrNbO_4$, $SiO_2$ and $Al_2O_3$. Although the oxides were found to be the same throughout the study, Nb2O5 oxide converts from Tetragonal $Nb_2O_5$ to Orthorhombic $Nb_2O_5$ at 900$^{o}$C and at 1400$^{o}$C, again converts to Monoclinic $Nb_2O_5$. Thus it can be said that $Nb_2O_5$ is consistent throughout with a variation in the forms. These variations in $Nb_2O_5$ were characterized by using XRD. At 1400$^{o}$C, the oxidation procedure has yielded to the formation of an intermediate layer which shows the formation of a combination of $Al_2O_3$ and $SiO_2$ alternatively. It is understood that this oxide layer has helped in controlling the flow of oxygen, acting as a barrier. Considering the outer most oxide layer which is a dense combination of $CrNbO_4$, $Nb_2O_5$ and $SiO_2$, with large amounts of porosity, the oxygen would have intensified the effect of consuming the metal. However, this has not occurred as the

IOL had an alternating series of $Al_2O_3$ and $SiO_2$. The X-Ray mapping of the oxide Intermediate layer is collected to prove the formation of $Al_2O_3$ and $SiO_2$.

The oxide products were subjected to X-ray diffraction to characterize the oxide products formed as shown in Figure 4.25. The formation of oxides at all temperatures was found to be very similar. The XRD analysis does not reflect the formation of $Cr_2NbO_4$, at 700°C and 800°C, however this phases becomes more predominant between 900 – 1400°C. As mentioned previously, the formation of $Al_2O_3$+$SiO_2$ was observed in a discontinues layer 1200°C in SEM images.

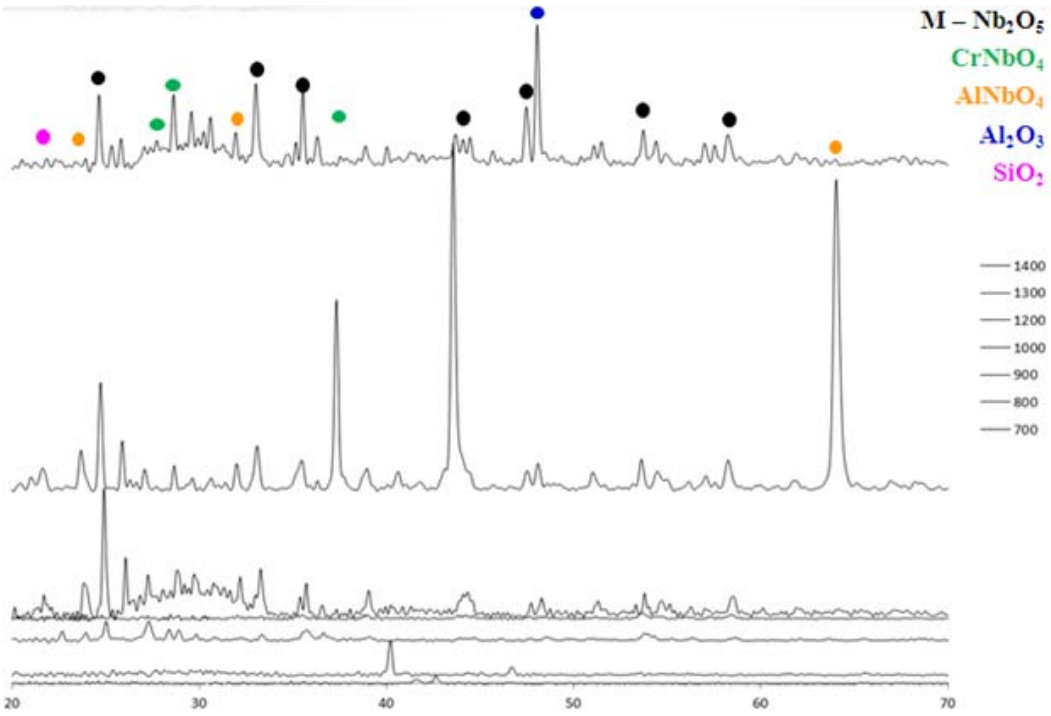


Figure 4.25: XRD analysis of oxide products of the alloy Nb-15Re-15Si-10Cr-20Al

### 4.5.5 Alloy Oxidation measurements as function of temperature:

The weight gain per unit area as a function temperature, is plotted to analyze the weight gain and loss at each temperature, shown in Figure 4.26. This curve shows that there has been a

negative weight gain at 800, 1000- 1300°C. The negative weight loss is studied as the lowering of the metal as the temperature increased. The amount of metal significantly decreased from approximately 60% at 1000°C to approximately 40% at 1300°C. Also the formation of $Nb_2O_5$ is decreased, making $CrNbO_4$, the dominant oxide. The weight gain at 900°C attributed to the formation of $Nb_2O_5$, and presence of a combination of oxides such as $Nb_2O_5$, $CrNbO_4$, $Al_2O_3$ and $SiO_2$ attribute to the mass-gain. Not to forget the internal oxidation also contributes to the weight gain. The metal remaining after the oxidation was approximately 40-60%, except at 900°C, the metal suffered pest oxidation, leaving no metal. For all other temperatures, the metal-oxide interface was fairly intact for 1000 – 1300°C. The metal was split in to two or more pieces during the oxidation at temperatures 700°C.

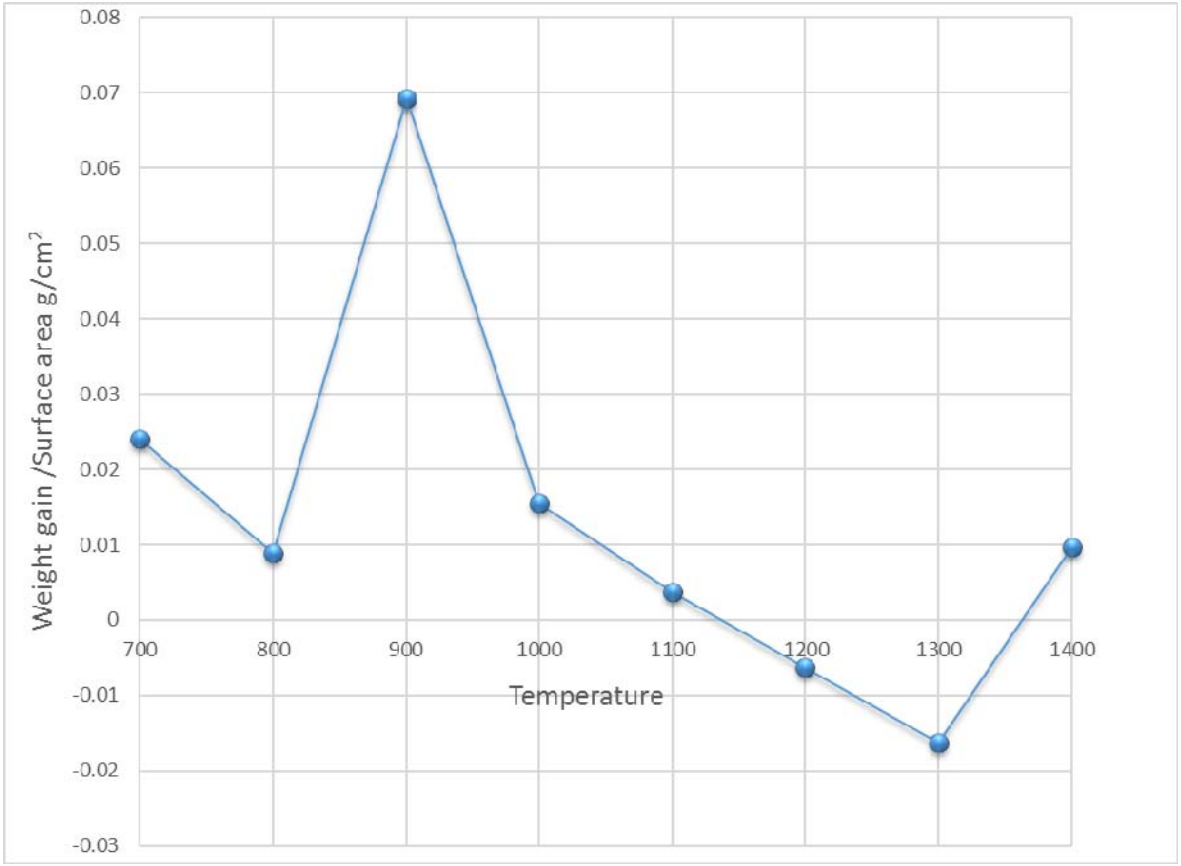


Figure 4.26: Short term oxidation weight gain/loss curves of the alloy Nb-15Re-15Si-10Cr-20Al

## 4.6 Nb-15Re-15Si-10Cr-10W

### 4.6.1 As-cast Microstructure:

Isothermal sections from the Nb-15Re-15Si-10Cr-10W system were calculated by holding rhenium and silicon constant at 15 at. pct using a thermodynamic modeling software, Pandat, developed by CompuTherm LLC for the entire temperature range of this alloy in an effort to determine phase transformations. The presence of stable phases as solid solution (BCC), $Nb_5Si_3$, NbCrSi and sigma phase were predicted at room temperature. Shown in Figure 4.27 are the calculated phase information from Pandat.

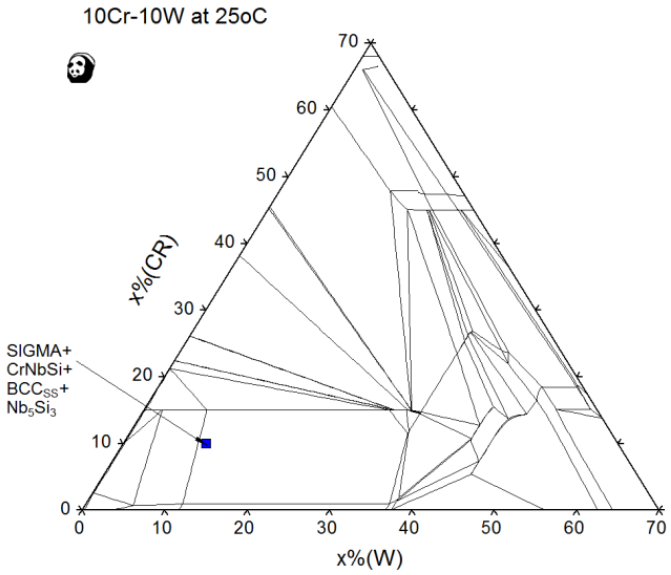


Figure 4.27 Isothermal section of Nb- Re-Si-Cr-W

However, the as-cast microstructure of the alloy as shown in Figure 4.28 depicts the presence of $Cr_2Re_3$ (very bright areas), $Nb_5Si_3$ (very dark areas), $NbCr_2$ (Medium grey areas) and solid solution (medium bright areas). The presence of rhenium, which has a higher atomic number, makes the phase brighter than any other phase. The heavier the element, when scanned in a SE or BS mode appears to be the brightest phase. $Cr_2Re_3$ is considered as high temperature

component, therefore it is understood that this phase might help in improving the overall oxidation properties. Laves phase was formed, and was found to be in medium dark blotchy patches, which was found to be in very limited concentrations when compared to the concentrations found at other temperature. X-Ray mapping of the as-cast structure is shown in Figure 4.29.

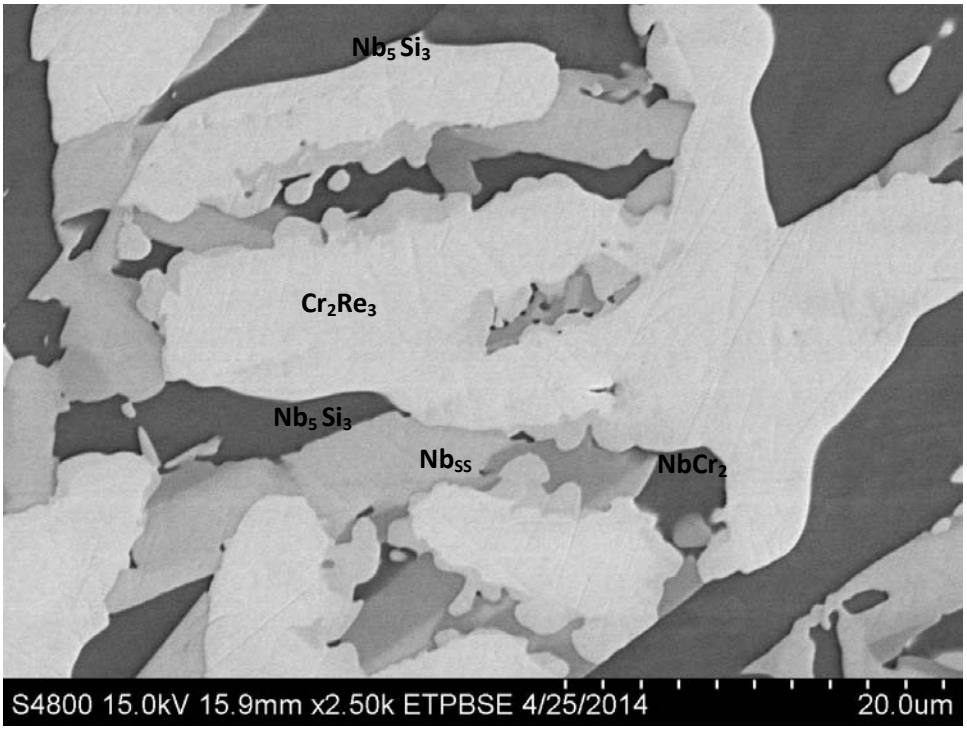

Figure 4.28: As cast micrograph of the alloy Nb 15Re 15Si 10Cr 10W

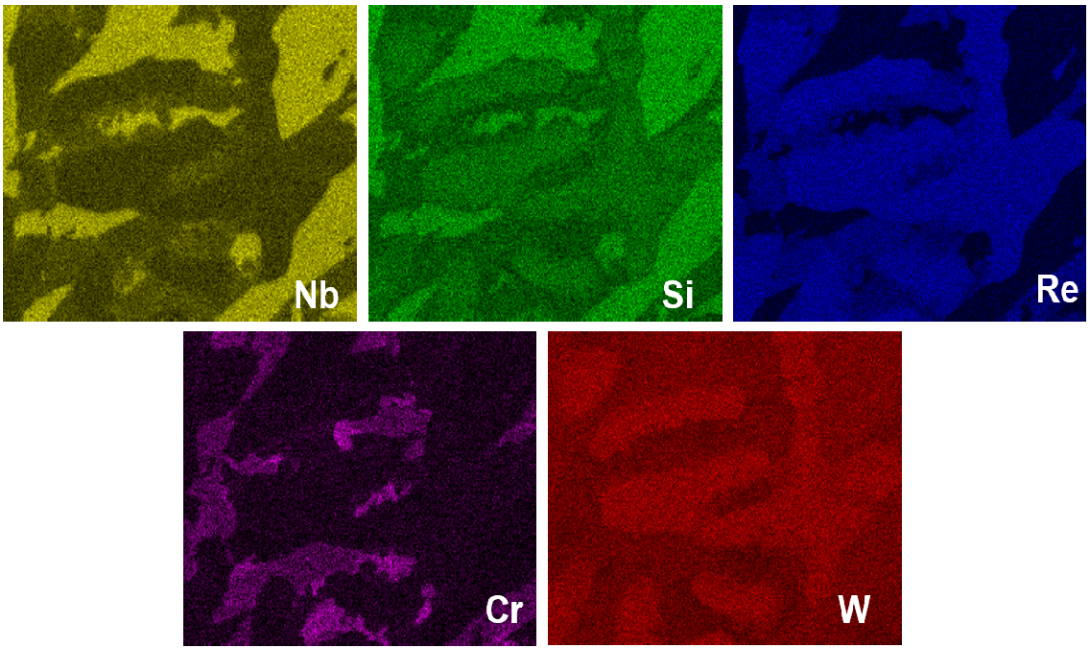


Figure 4.29 – As cast micrograph of the alloy X-Ray Mapping of the alloy (in reference to Figure 4.28).

### 4.6.2 Evolution of Microstructure between temperature range 700 – 1400°C:

Isothermal sections were developed using PANDAT™ to show the variations in phase formation between a temperature ranges of 700 – 1400°C. Variations in the phases were observed at 700 and 900°C and shown in Figure 4.30. The analyzed phases through SEM and XRD, however were consistent throughout. The phases formed at room temperature were the same until 1300°C. These deviations between the depicted phases and the calculated phased through PANDAT™ are occurred due to the non- equilibrium cooling conditions, which produce a deviation from the calculated phases.

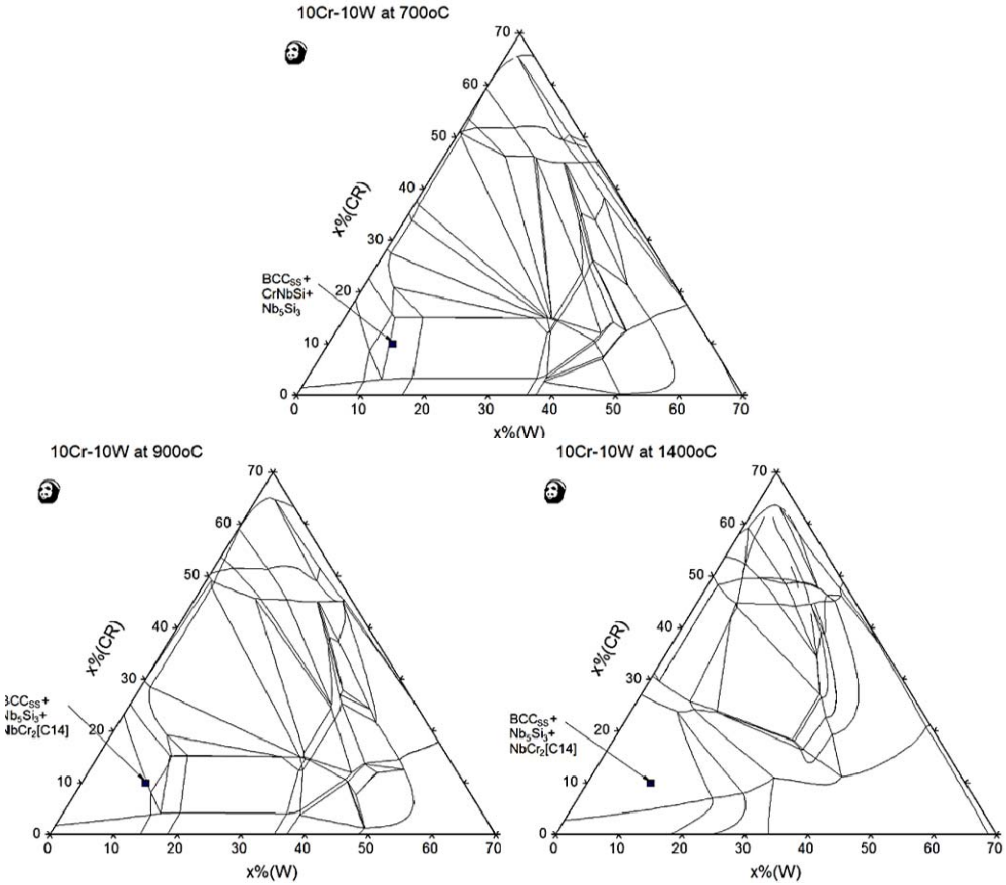

Figure 4.30: Isothermal sections of Nb- Re-Si-Cr-W at 700, 900 and 1400$^{o}$C

The evolved microstructure between 700 – 1000$^{o}$C were same as the as-cast, they are $Cr_2Re_3$ (very bright areas), $Nb_5Si_3$ (very dark areas), $NbCr_2$ (Medium grey areas) and α - solid solution (medium bright areas). Figure 4.31 shows the SEM images of the phase development. It was observed through the microstructures that the amount of porosity was high, at 700 and between 1100 – 1300$^{o}$C. This has enabled the flow of oxygen into the metal and has results in the formation of $Nb_2O_5$, $CrNbO_4$ and $SiO_2$. Starting from 800 -1000$^{o}$C, the porosity was drastically decreased, and the phased formed were same. The SEM images between 700 – 1000$^{o}$C are shown in 4.31.

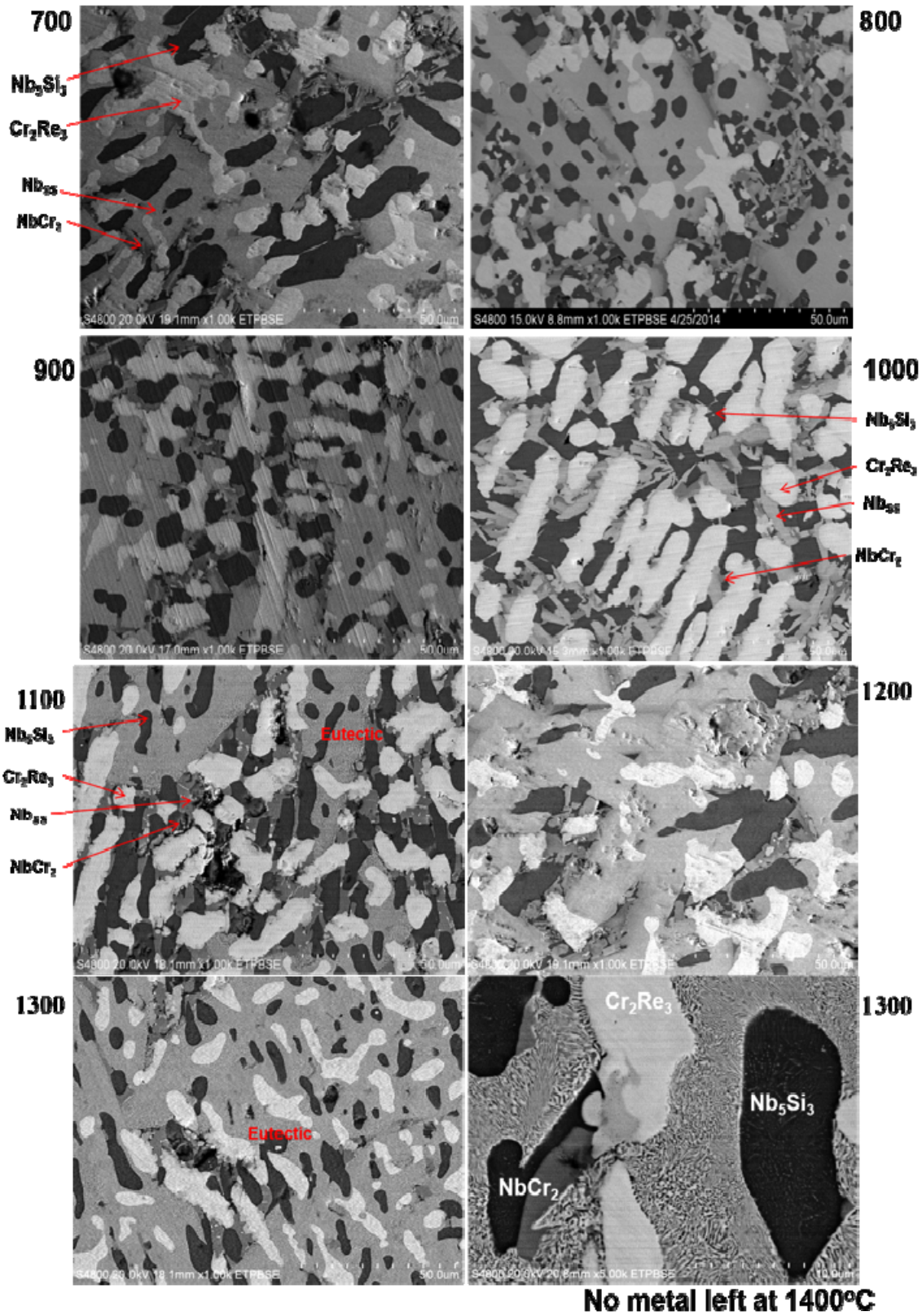


Figure 4.31: Micro structures of remaining metal between 700 – 1300°C

Starting at 1100°C, the microstructure reveals a eutectic between the solid solution and $Nb_5Si_3$. Therefore now, the phase constituents form to be $Nb_{SS}$ (α), eutectic (α), $Nb_5Si_3$, $Cr_2Re_3$, and $NbCr_2$. Also observed was the increased amounts of porosity, leading to the oxide spalling at 1300°C. The microstructures reveal the existence of porosity. A high magnification BS image is presented in 4.31, to show the formation of the eutectic. There was no metal left at 1400°C. The metal was completely converted to an oxide, but was found without any spalling.

### 4.5.3 Oxide Surface analysis

Figures 4.32 show the appearance of the oxide layer after isothermal oxidation for 24 hours at different temperatures. The presence of W addition sin this alloys has caused to the formation of $Nb_2WO_5$. This alloys forms a phase in the oxide layer as shown in the image, in bright areas. At 900 the oxides formed were $Nb_2O_5$, $Nb_2WO_5$, $CrNbO_4$ and $SiO_2$, $WO_3$. Porosity was observed at all temperatures in the oxide layer.

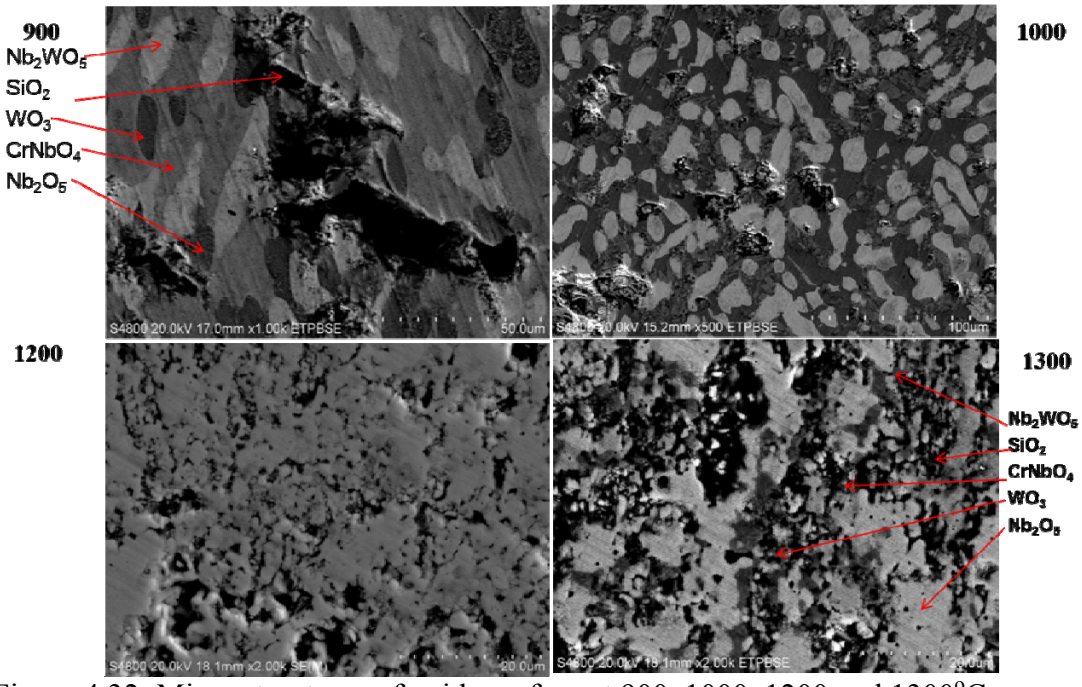

Figure 4.32: Micro structures of oxide surface at 900, 1000, 1200 and 1300°C

A magnified image of the oxide layer at 1100°C, show the formation of $Nb_2WO_5$, $CrNbO_4$, $WO_3$, $Nb_2O_5$ and $SiO_2$, shown in Figure 4.33. The oxides are shown clearly are distinguished, shows the oxygen diffusion along the porosity. The microstructure reveals the combination of $CrNbO_4$ and $NbWO_5$ to form a series of alternating wavy structure. Also the $WO_3$ is formed at localized regions, looking like bands in the midst of $Nb_2O_5$. $SiO_2$ is formed along the pore regions. X-ray mapping was scanned to determine the formation of these oxides, in Figure 4.34. Also noticed was that as the temperature increased the oxide surfaces were smoother.

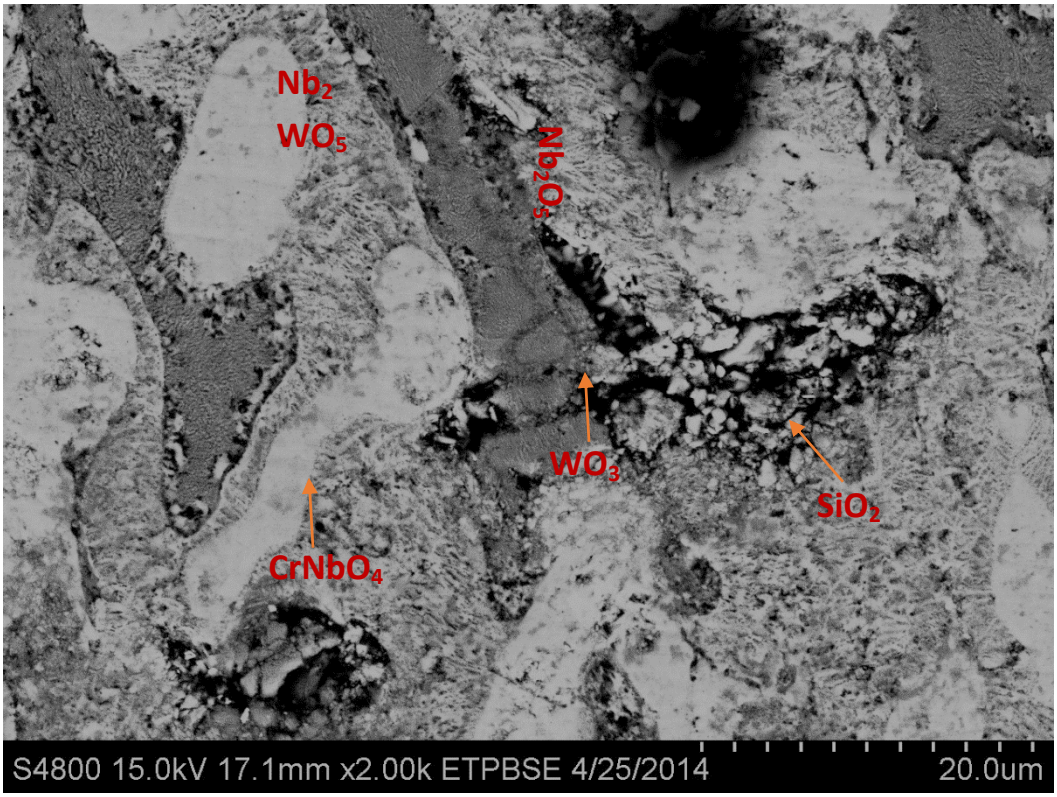


Figure 4.33: SEM image of the oxide layer at 1100°C

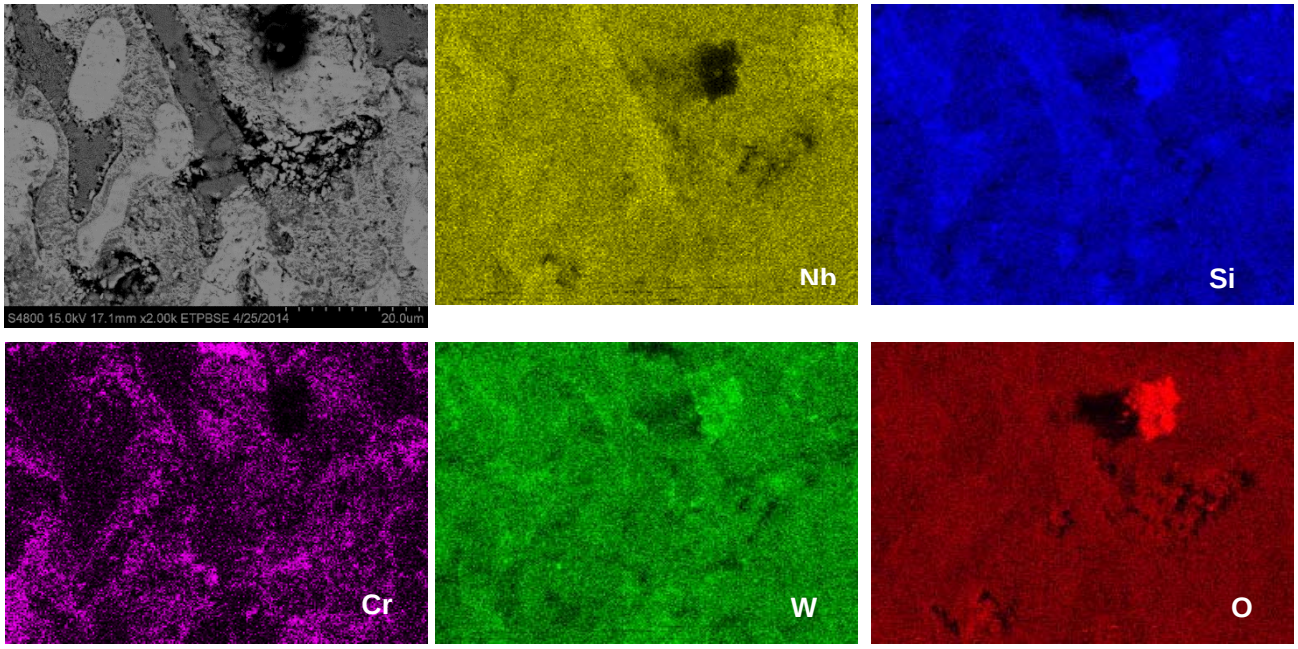


Figure 4.34: SEM image of the oxide layer at 1100$^{o}$C

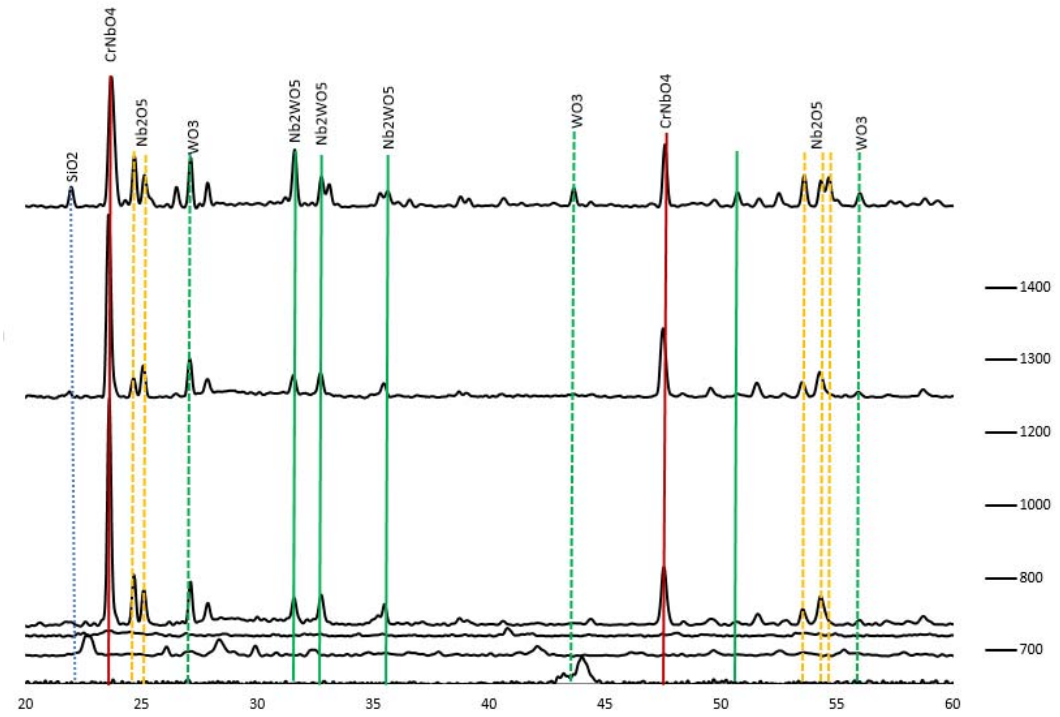


Figure 4.35: XRD pattern of the oxidation products obtained from the alloy after 24 hours of exposure

### 4.6.4 Metal – Oxide Interfaces Regions

The oxide-metal interfaces were studied for the alloy at all temperatures. Figure 4.36 shows the microscopic images at 900$^{o}$C, 1000$^{o}$C and 1200$^{o}$C. The formation of allotropes of $Nb_2O_5$ has been observed depending on the oxidation temperature. The oxide converts from orthorhombic to monoclinic form at 1000$^{o}$C, and remains the same until 1400$^{o}$C. The formation of orthorhombic form of $Nb_2O_5$ at all the temperatures can be attributed to the presence of relatively large amounts of solid solution in the alloy.

The oxide at 700$^{o}$C consists of $Nb_2WO_5$, $Nb_2O_5$, $CrNbO_4$, $WO_3$ and SiO2. Although the formation of WO3 and $Nb_2WO_5$ is observed in the microstructures, these phases were not very dominant in the XRD data. As the temperature increases, the formation of these oxides become more evident. At 800$^{o}$C, CrNbO4 begins to form in minimal amounts along with $Nb_2WO_5$, $WO_3$ and $SiO_2$. The same oxides are formed until 1400oC.

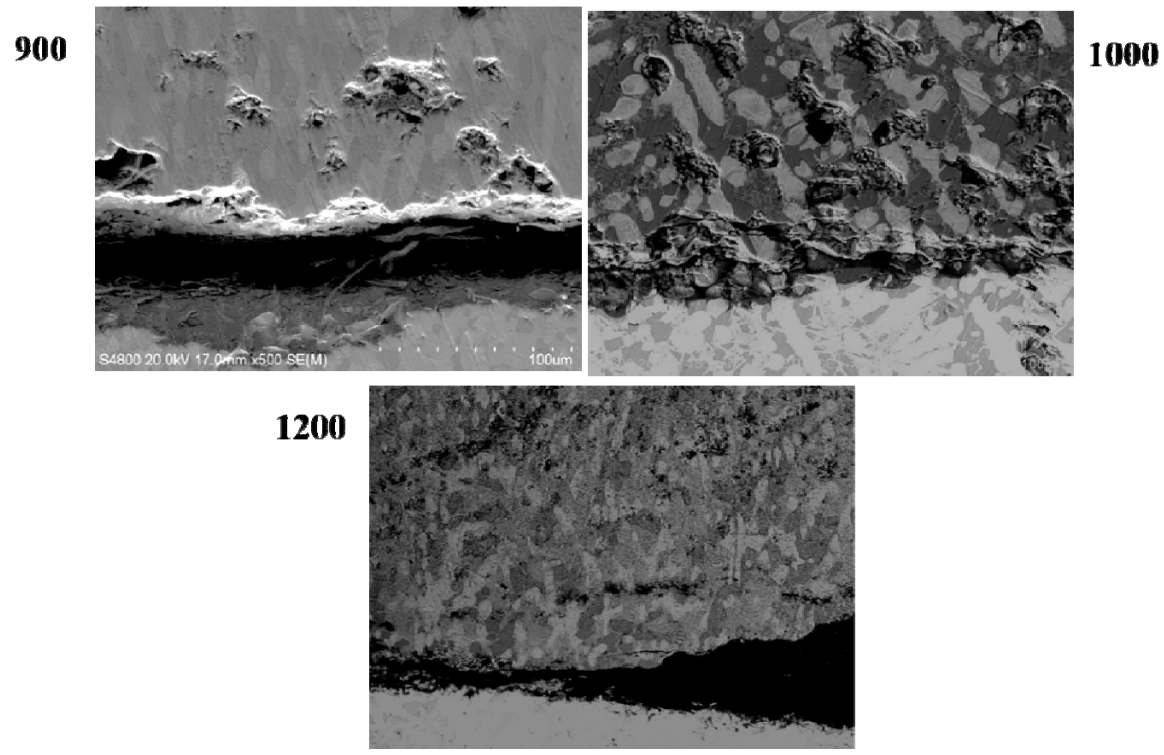


Figure 4.36: Interfaces at 900, 1000 and 1200$^{o}$C

Formation of these oxides along the interface was noticed to see any Cr – depletion layer. However this was not observed. To confirm this the X-ray mapping was performed as shown in Figure 4.37, where Yellow represents Nb, Green – Silicon, Purple – Cr, Blue W and Red – O. The cracks formed between the oxide and the metal has been observed at all temperatures. This effect is usually the result of the mismatch of specific volumes and stresses brought on by the differences in the coefficients of thermal expansion of oxides.

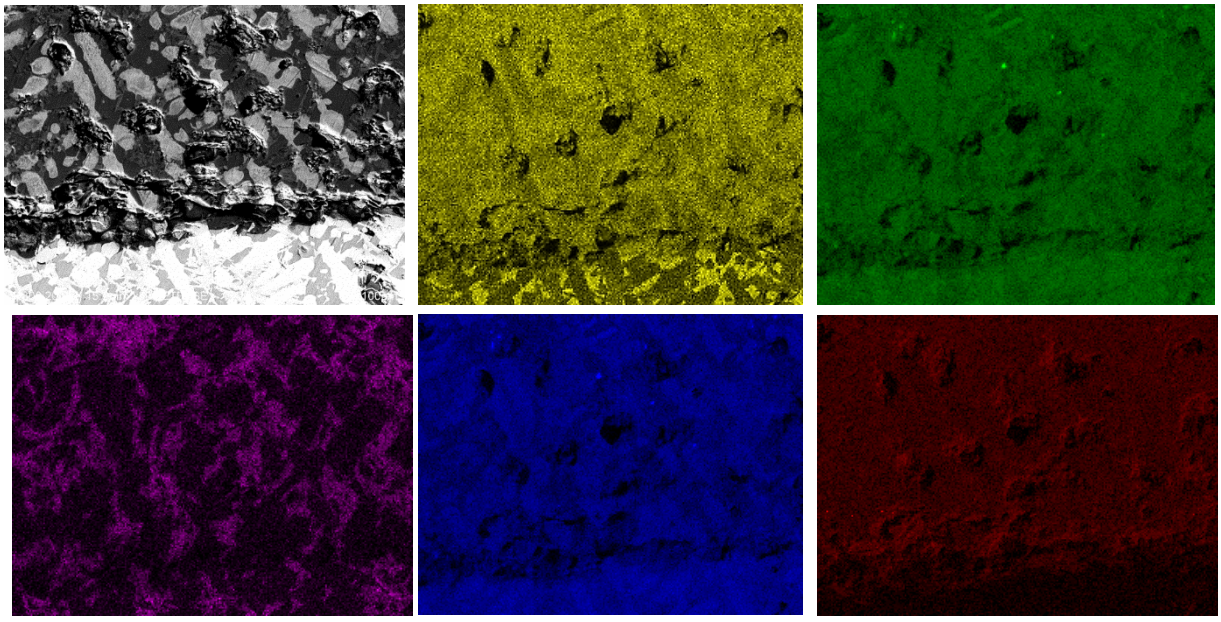

Figure 4.37: X- Ray mapping of interface at 1200$^{o}$C

### 4.6.5 Alloy Oxidation Measurements as a function of time

The curve in Figure 4.38 shows the weight gain per unit area as a function oxidation temperature. This curve shows that there has been a weight loss through the temperature range from 900°C -1400°C except at 1300°C. The constant weight loss observed is due the formation of volatile rhenium and chromium oxides. Noticeable evidence from the crucibles was also detected, as the alumina crucibles changed their color to a bluish brown, suggesting the escape of

the oxide. The mass-gain at 800 and 900°C may be due to the formation of the bulky oxide which includes Nb2WO5, $Nb_2O_5$, CrNbO4, $WO_3$ and SiO2. An estimated 45-70% of the metal was remaining after the samples were subjected to oxidation procedure, excluding at 1400°C. The metal-oxide interface was fairly intact at all temperatures, indicating good oxidation resistance.

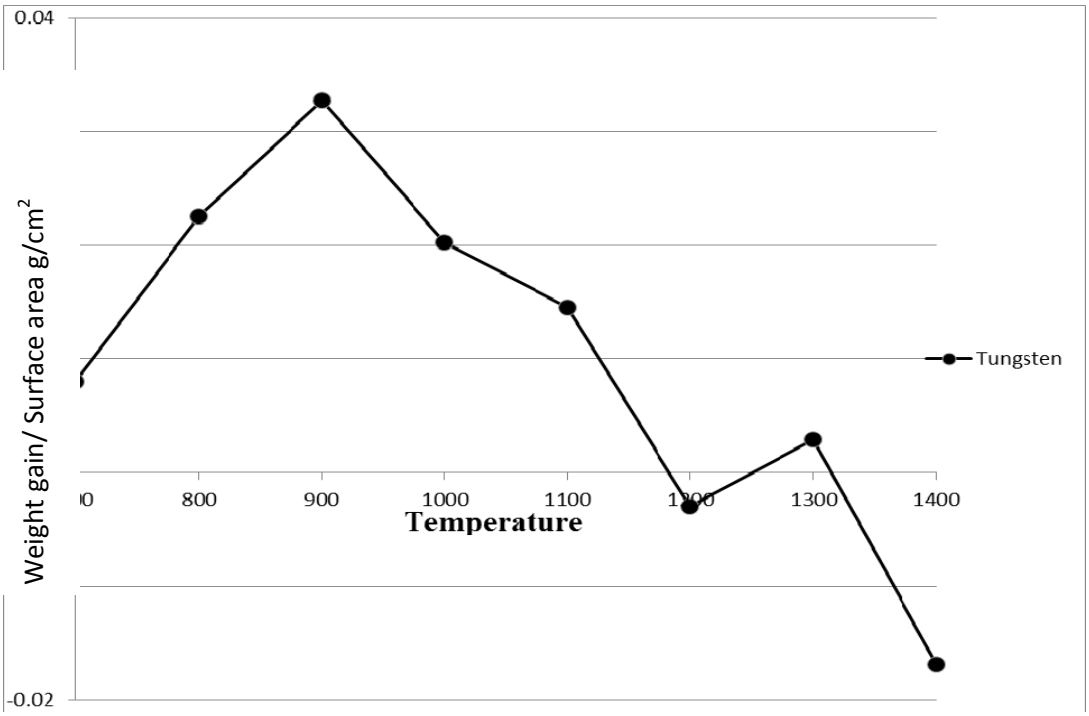


Figure 4.38: Short term oxidation weight gain/loss curves

## 4.7 Nb-15Re-15Si-10Cr-10B

### 4.7.1 As-cast Microstructure:

Isothermal sections from the Nb-15Re-15Si-10Cr-10B system were calculated by holding rhenium constant at 15 at. pct using a thermodynamic modeling software, Pandat, developed by CompuTherm LLC for the entire temperature range of this alloy in an effort to determine phase transformations. Also, to note that as the software does not have the

Boron elemental additions, makes it incapable to add this element in this study. The presence of stable phases as solid solution (BCC), $Nb_5Si_3$, NbCrSi and $Nb_9Si_2Cr_3$ phase were predicted at room temperature. Shown in Figure 4.39 are the calculated phase information from Pandat.

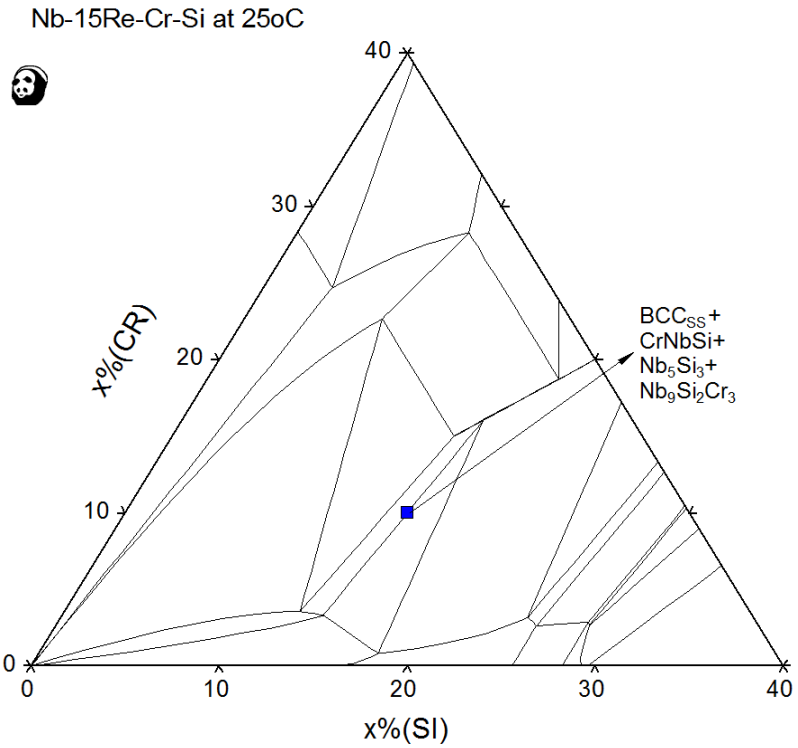


Figure 4.39 Isothermal section of Nb- Re-Si-Cr

The as-cast microstructure of the alloy as shown in Figure 4.40 depicts the presence of $Nb_5Si_3$, $NbCr_2$ and Nb solid solution. Laves phase was formed, and was found to be in dark blotchy patches, which was found to be in very limited concentrations when compared to the concentrations found at other higher temperatures.

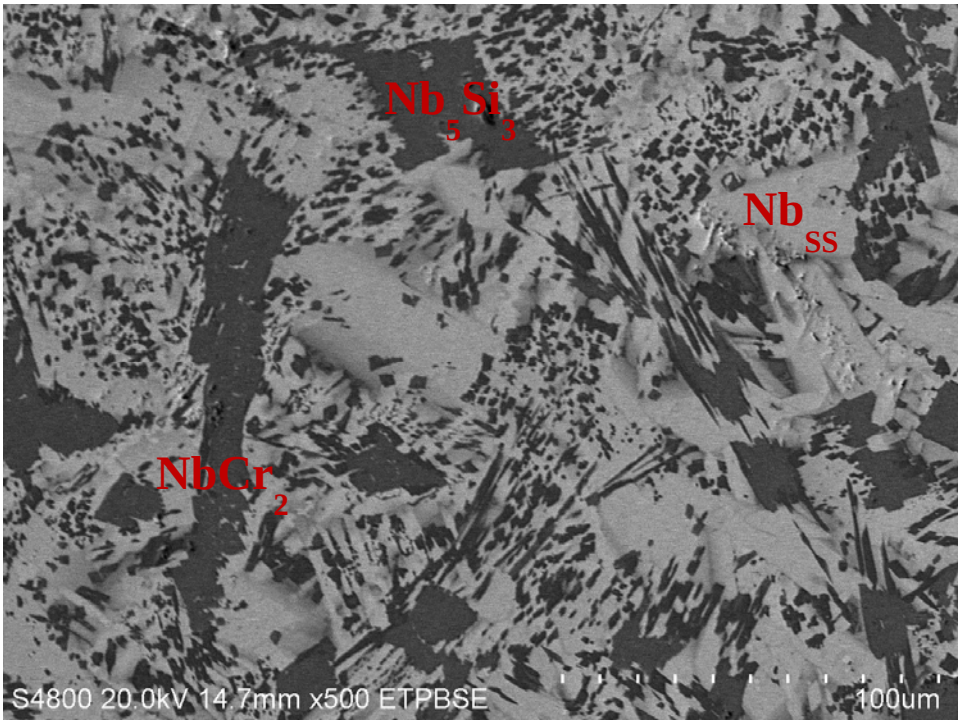


Figure 4.40: As cast micrograph of the alloy Nb 15Re 15Si 10Cr 10B

### 4.7.2 Evolution of Microstructure between temperature range 700 – 1400°C:

A series of isothermal sections were developed using PANDAT™ to show the variation in phase formation between a temperature ranges of 700 – 1400°C, Figure 4.41 shows section at 700 and 1400°C as there was no phase change occurred in between. Any deviations between the depicted phases and the calculated phased through PANDAT™ are explained as due to the non-equilibrium cooling conditions which produce a deviation from the calculated phases.

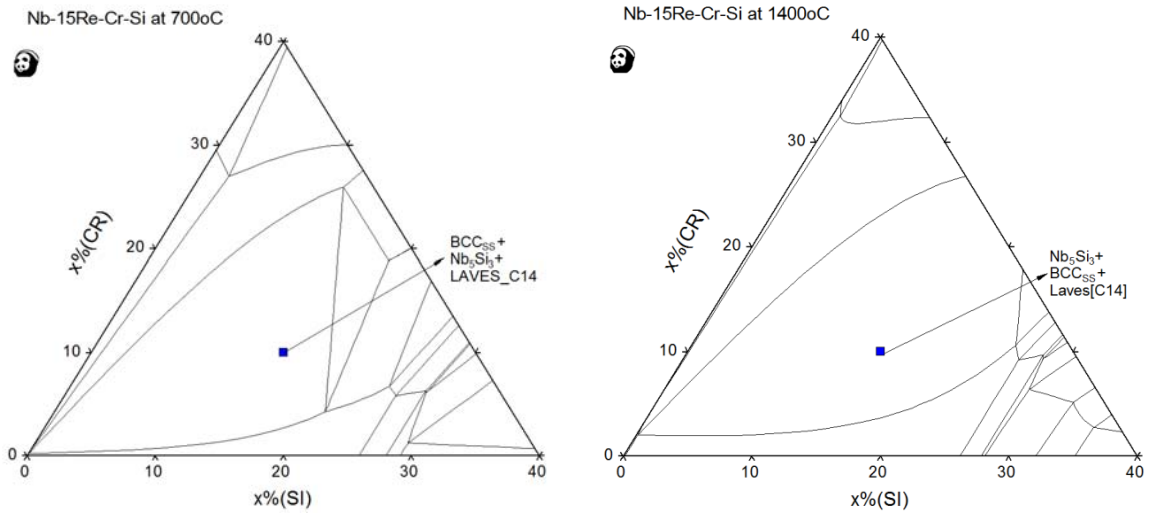


Figure 4.41 Isothermal sections of Nb- Re-Si-Cr at 700 and 1400$^{o}$C

The metal remaining was collected after the oxidation procedure and was subjected to microstructural characterization. At 700$^{o}$C the phases formed were $Nb_5Si_3$, Nb solid solution and Laves phase, shown in Figure 4.42. A special feature has been observed from 700-900$^{o}$C. At these temperatures eutectic like microstructure is developed, along with needle like structures have been developed, leaving very little $Nb_5Si_3$. This eutectic like structure and needle like structure was an integration of the solid solution and the 3,5 silicide. At 1000$^{0}$C, $Nb_{22}Re_7$ has become a more dominated phase also an increased amount of $NbCr_2$ was observed. The formations of two intermetallics have contributed to a large extent, in decreasing/altering the kinetics of the formation of oxides. This was the reason to include the specific alloy composition for this alloy. $Nb_{22}Re_7$ is a high temperature phase in the Nb-Re phase diagram. This phase usually is preferred for varied high temperature uses. A X-ray elemental mapping of alloy at 1000$^{o}$C is shown in Figure 4.43.

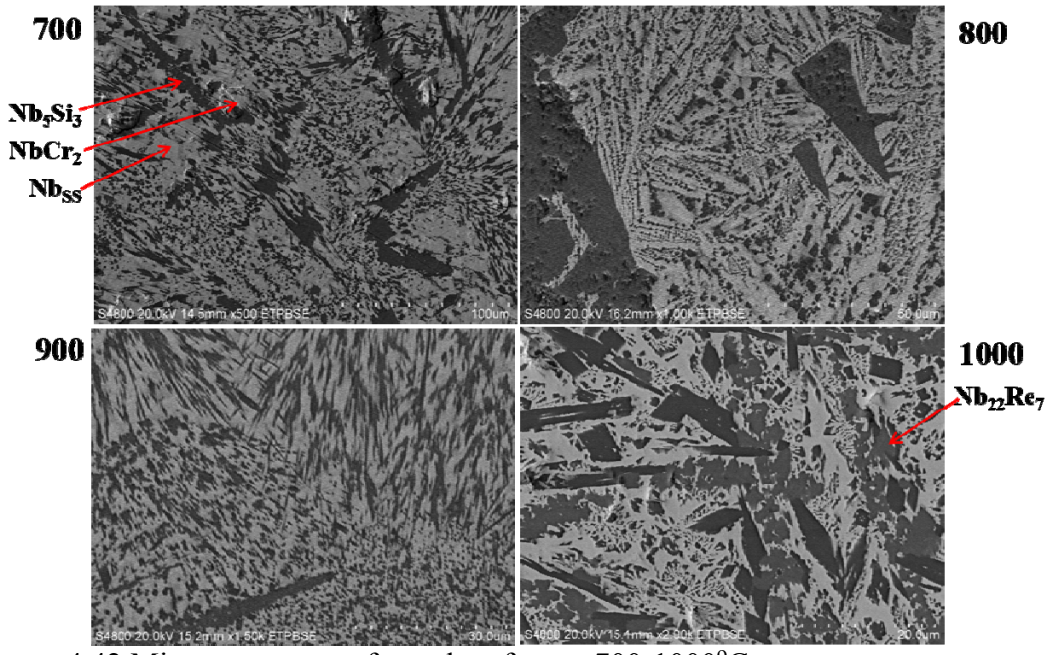


Figure 4.42 Micro structures of metal surface at 700-1000°C

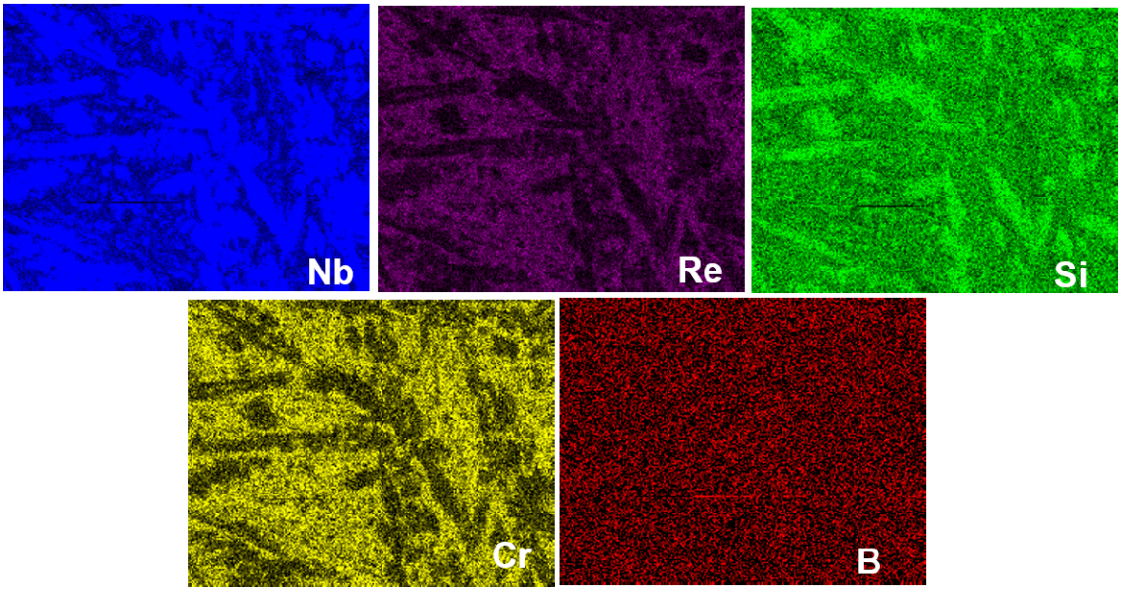


Figure 4.43: Elemental X-Ray mapping of the alloy at 1000°C

Figure 4.44 shows the evolved microstructures in the temperature range from 1100°C to 1400°C. At 1100°C, the formation of same phases ($Nb_5Si_3$, Nb solid solution and Laves phase) were continued. However, the microstructures changes to small box like structure of 3,5 silicide.

Also at this temperature $Nb_{22}Re_7$ was not found. Again at 1200$^{o}$C, a eutectic like microstructure and also needle like structure was observed. At 1300$^{o}$C, the structure continues and it is understood that $Nb_{22}Re_7$ is formed at 1300$^{o}$C also. A magnified view of the alloy is also shown in Figure 4.44. There was no metal left at 1400$^{o}$C.

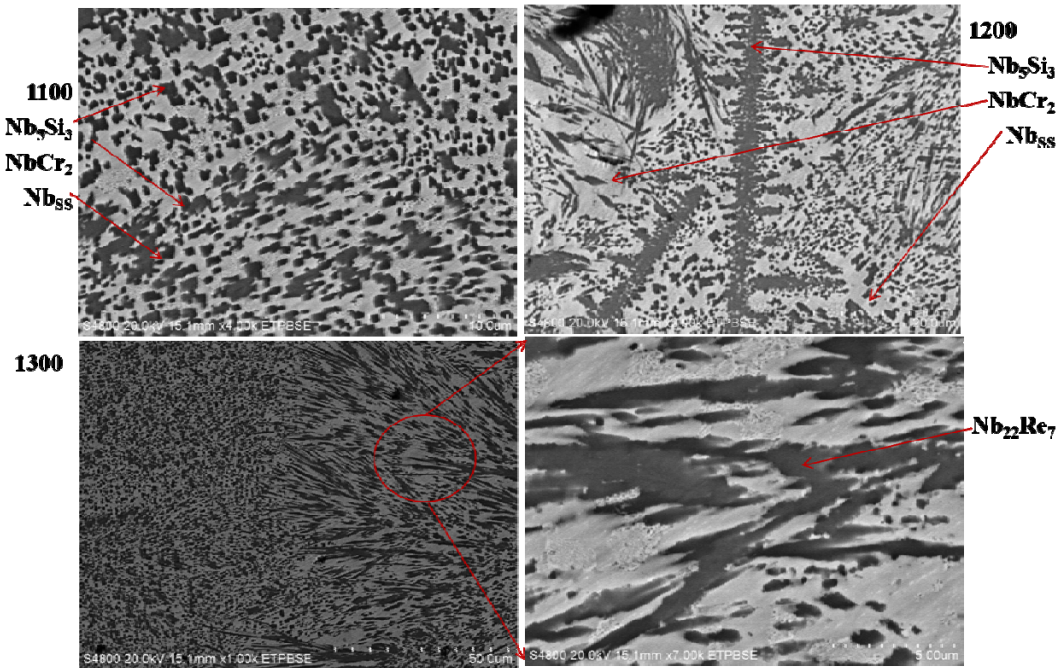


Figure 4.54 Micro structures of metal surface at 1100-1300$^{o}$C

### 4.7.3 Oxide Surface analysis

$Nb_2O_5$ (light grey regions), $CrNbO_4$ (dark grey regions) and very limited amounts of $SiO_2$ along with a large amounts of porosity was formed at 700$^{o}$C as shown in Figure 4.45. $CrNbO_4$ is usually formed, as Cr diffuses outward and oxygen diffuses inward. $Cr_2O_3$ is deduced by EDS data, but XRD does not reflect the same. The reason could be the fact that the amount of $Cr_2O_3$ is not only very small but also localized. It is understood that the combination of $Nb_2O_5$ with $Cr_2O_3$ may results in the formation of $CrNbO_4$ in this alloy.

The samples subjected to temperatures between 700 – 1400$^{o}$C, the large amount of porosity was filled with $SiO_2$. There was no noticeable deviation with regards to the oxides formed or the amount of porosity. As the viscosity of $SiO_2$ is low, it causes the viscous oxide flow and fill the surrounding pores. A clear distinction between a pore and $SiO_2$ cannot be made due to their similar contrast. But $SiO_2$ may look like a concentrated phase with a concave shape. On the contrary, a pore may visibly seem like a little pit with depth.

The combination of the oxides ($CrNbO_4$ and $SiO_2$) is considered to be advantageous, when compared to $Nb_2O_5$ formed alone in the oxide layer. It has been reported that the combination of $CrNbO_4$ and $SiO_2$ prevent the inward flow of the oxygen and therefore the kinetics of the oxidation is highly decreased. $Nb_2O_5$ often tends to form bulky form of oxides, with porosity increasing the flow of oxygen, which has resulted in spalling at higher temperatures for this alloy at 1200 and 1300$^{o}$C. The cracks formed between the oxide and the metal has been observed starting from 700$^{o}$C.

The oxide products were subjected to X-ray diffraction to characterize the oxide products formed as shown in Figure 4.46. The formation of oxides at all temperatures was found to be very similar to EDS data. Except very small peaks for $B_2O_3$. Although XRD analysis does reflect the formation of $Cr_2NbO_4$, the EDS data could not identify this oxide formation at 700$^{o}$C. However this phases becomes more predominant between 900 – 1400$^{o}$C.

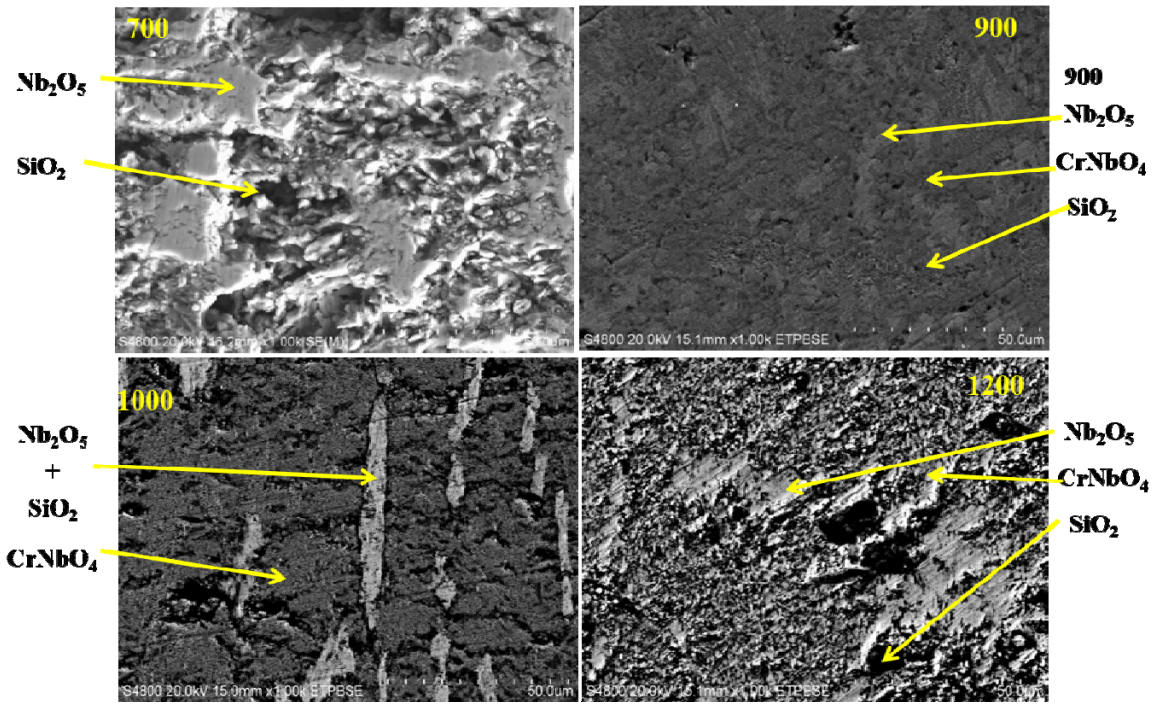


Figure 4.45: Micro structures of oxide surface at 700, 900, 1000 and 1200°C

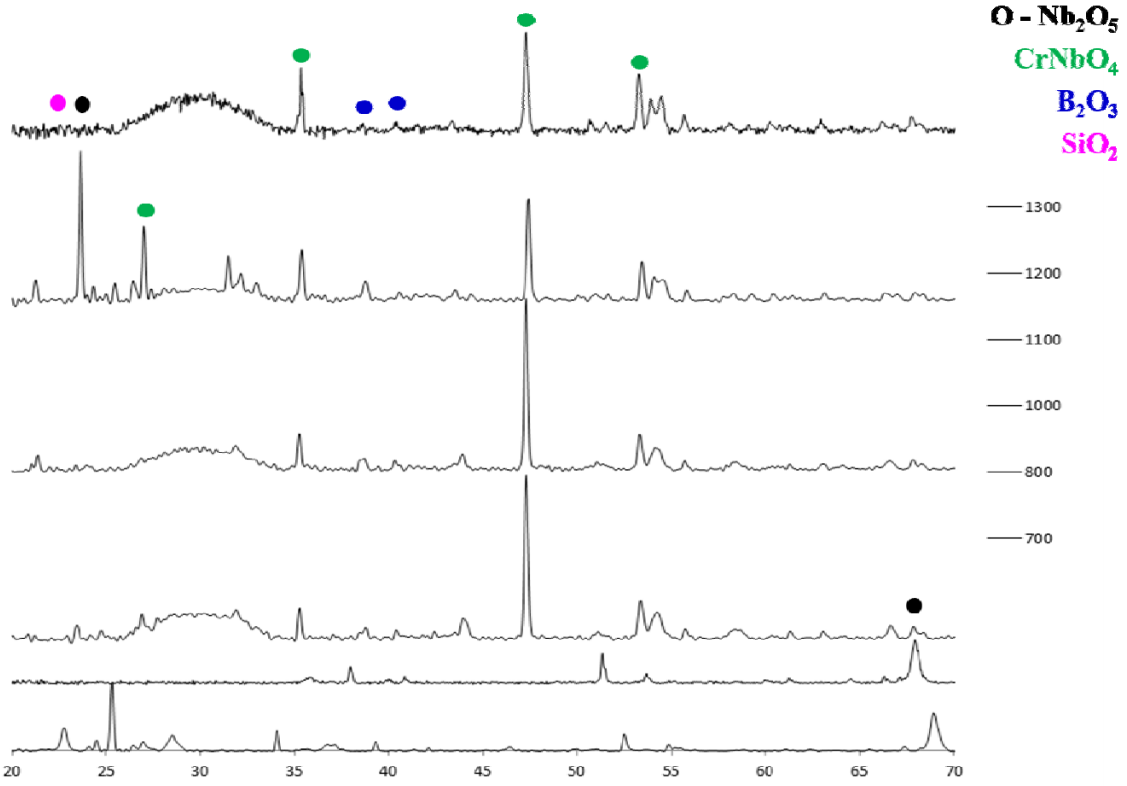


Figure 4.46: XRD pattern of the oxidation products obtained from the alloy after 24 hours of exposure

### 4.7.4 Metal/Oxide Interfaces Regions

The oxide-metal interfaces were studied for the alloy at all temperatures. Figure 4.47 shows the microscopic images at 800°C, 900°C, 1000°C, and 1200°C. All three oxides $Nb_2O_5$, $CrNbO_4$ and $SiO_2$ were formed at all temperatures; however the amounts vary with respect to temperatures. Although $CrNbO_4$ was formed at all temperatures, it was barely found at 700°C. However, at higher temperatures this oxide becomes more dominant. The cracks are a result of a mismatch of their specific volumes and stresses developed due to the differences in the coefficients of thermal expansion of oxides. In Figure 4.58, an elemental X-Ray mapping of the interface at 800°C is shown.

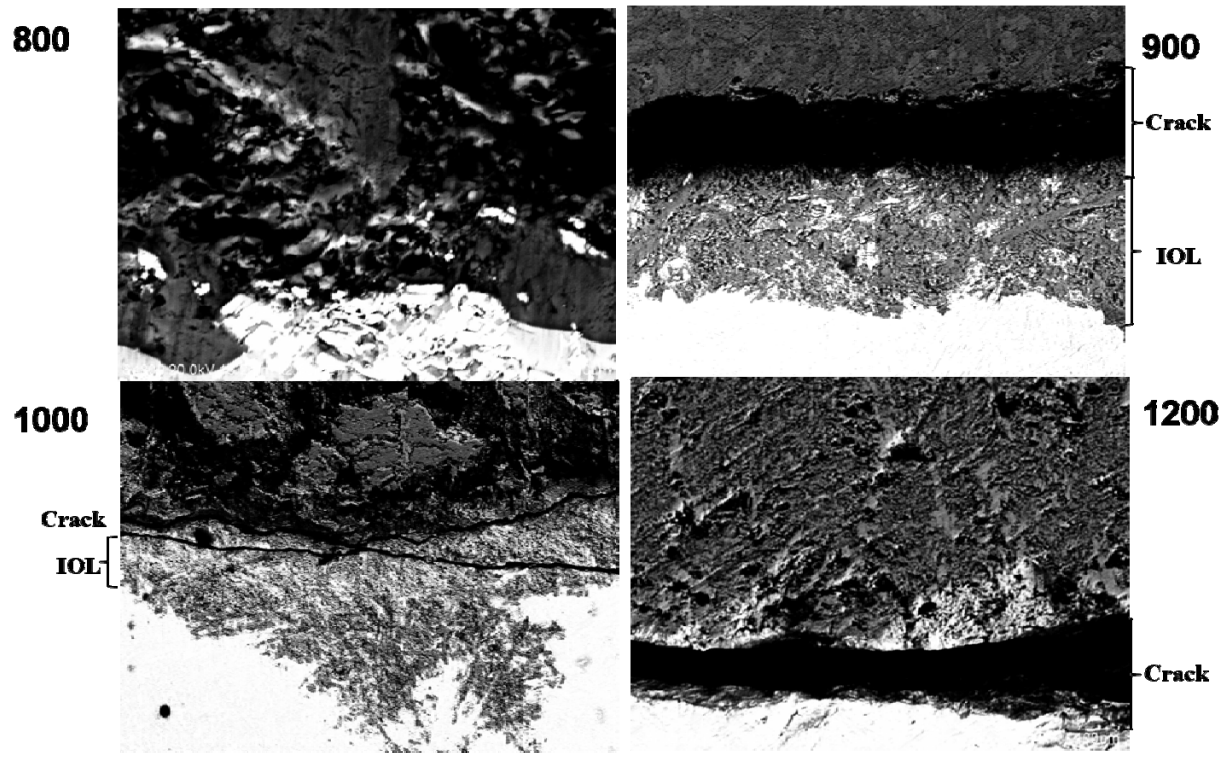


Figure 4.47: Interfaces at 800, 900, 1000 and 1200°C showing Intermediate oxide layer and Oxide layer.

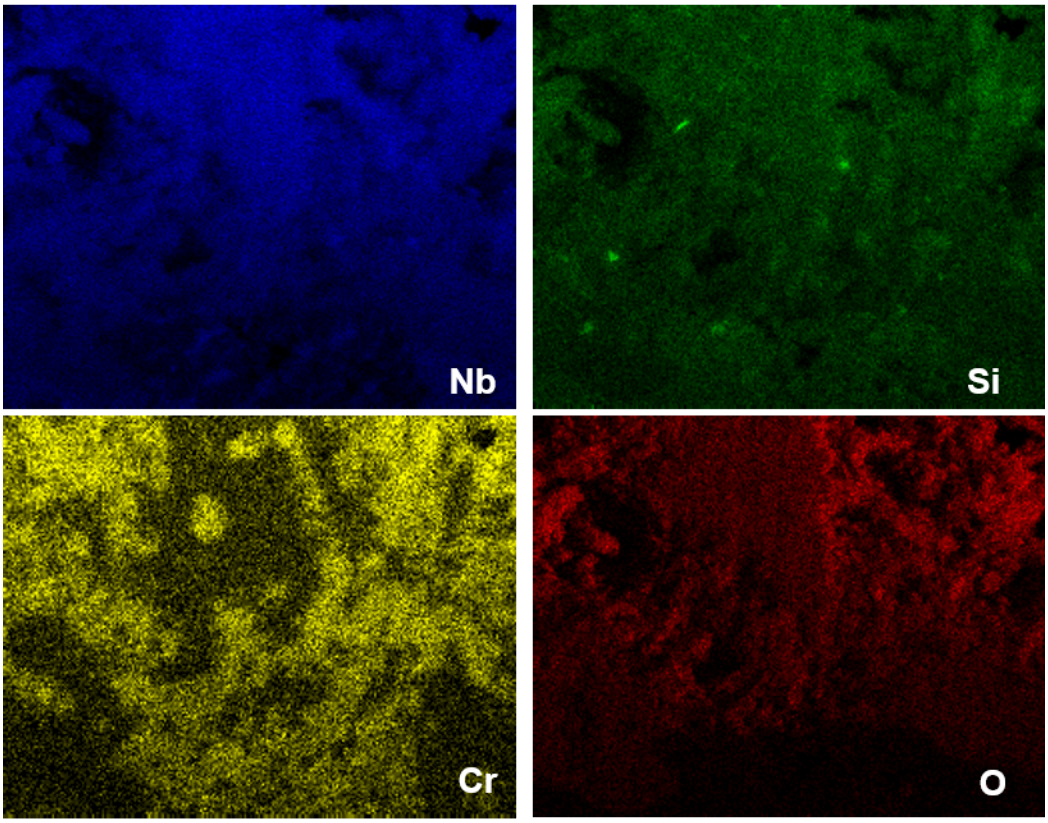


Figure 4.48: X- Ray elemental mapping of Interfaces at 800$^{o}$C showing Intermediate oxide layer and Oxide layer.

### 4.7.5 Alloy Oxidation Measurements as a function of time

The weight gain per unit area as a function oxidation temperature is shown in Figure 4.49. This curve shows that there has been a negative weight gain only at 800 and 900°C, and a steady weight loss occurs from 1000 – 1400$^{o}$C. It can be interpreted that the weight loss observed is due the formation of the phase $Nb_{22}Re_7$ exposed in the oxidation procedure results in the formation of chromium oxide ($Nb_2O_5$) and rhenium oxide ($Re_2O_7$, $Re_3O_{10}$) and $Cr_2O_3$. Oxides being volatile, contributes to the weight loss. Also the presence of Nb & Cr involved phases promotes the evidence of formation of $CrNbO_4$. From this we can prove the presence of $Cr_2O_3$. The mass-gain at other temperatures can be explained as the increased amounts of $CrNbO_4$,

along with $Nb_2O_5$. An estimated 70-45% of the metal was remaining until 1300°C, for all the samples after they were subjected to oxidation procedure. The metal-oxide interface was fairly intact from 700 – 1200°C indicating good oxidation resistance when compared to initial studies of the alloys.

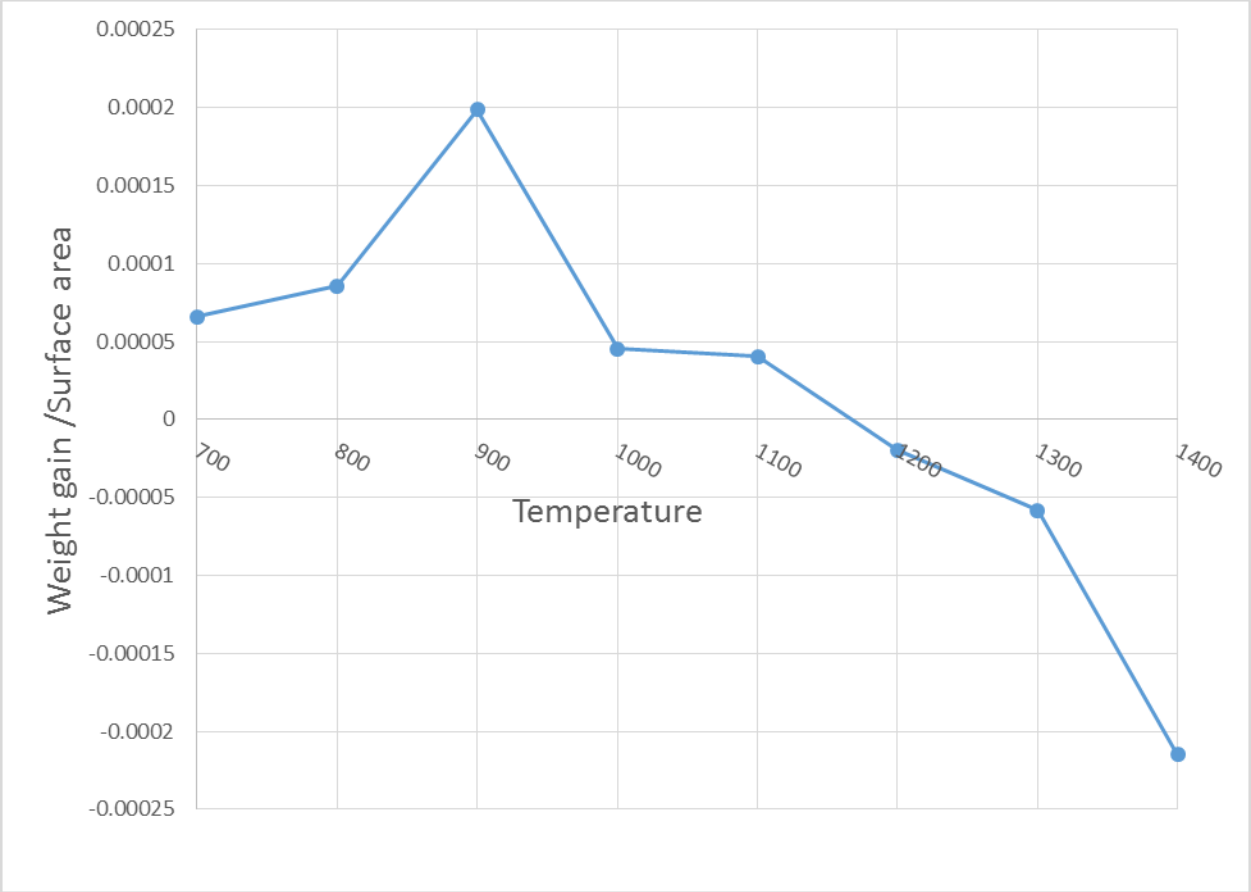


Figure 4.49: Short term oxidation weight gain/loss curves

## Chapter 5 - Conclusions

### 5.1 – Binary, Ternary, Quaternary Alloys:

1. The computational information from phase diagrams and isothermal sections seems to deviate from the experimental values, due to the fact that all phase diagrams and isothermal sections are constructed under equilibrium conditions.
2. The microconstituents observed in as cast binary alloy were $Nb_{ss}$ in Nb-5Re alloy, $Nb_3Si$ and $Nb_{SS}$ in Nb-5Si alloy and in Nb-5Cralloy, $Nb_{SS}$ and $NbCr_2$. In ternary alloy Nb-5Re-5Si, $Nb_5Si_3$ and $Nb_{SS}$ were observed, and in Nb 5Re5Cr alloy $NbCr_2$, $ReCr_2$ and $Nb_{SS}$ were formed. In the quaternary alloy, NbSS, $Nb_5Si_3$ and $NbCr_2$ were formed.
3. Rhenium enhances the formation of 3,5 silicide in the Nb-5Re-5Si alloy. Whereas in the binary alloy, it was observed that 1,3 silicides were formed. 3,5 silicides are preferred because of their high temperature and better creep resistance.
4. The deviations are explained as insufficient amount of Re percentages to form any significant Re-rich phase, such as $Re_2Si$ or $Re_2Cr_3$. Phase fraction vs temperature graphs, have helped to understand the deviations.
5. Oxidation resulted in pesting at all temperatures (700-1000$^{o}$C). Large amount of niobium solid solution has led to form Nb based oxides resulting in powdered oxidation products.
6. Mass loss for alloys is due to the volatile rhenium and chromium oxides, and the weight gain at for alloys is due to the formation of $Nb_2O_5$ bulky oxides. XRD confirms these observations

**5.2 Nb-15Re-15Si-10Cr-20Al:**

**1.** The microconstituents observed in the as-cast structure were Nbss, $Al_3Nb$, and $NbCr_2$. The Pandat$^{TM}$ predicts the formation of $BCC_{SS,}$ $Nb_5Si_{3,}$ CrNbSi, $Al_3$ (Do22) and $Al_{11}Re_4$. The difference in the microconstituents was observed. $Al_3Nb$ provides a very good oxidation resistance except at 1300$^o$C.

**2.** The morphology of the phases for oxidized samples from 700 – 1400$^o$C does not appear to change drastically. However at 900, the oxide was complete consumed by pest oxidation, leaving no metal. The powdered oxide was analyzed through XRD.

**3.** The oxide converts from Tetragonal to Orthorhombic at 900$^o$C, which usually is responsible for pesting and finally at 1400$^o$C, depicts monoclinic form of $Nb_2O_5$.

**4.** The improved oxidation resistance of the alloy can be attributed to the formation of CrNbO4, along with a discontinuous layer of $Al_2O_3$ + $SiO_2$, which starts to form at 1000$^o$C.

**5.** Mass loss at temperatures from 800, 1000 -1300$^o$C and 1200 – 1400oC can attributed to the formation of rhenium and chromium volatile oxide (temperature >1000$^o$C), and the weight gain at 900$^o$C is due to the formation of $Nb_2O_5$, $Al_2O_3$, $SiO_2$ and $CrNbO_4$. XRD and X- Ray mapping confirm these observations.

6. Improvements were found when compared to the Binary, ternary and quaternary alloys.

### 5.3 Nb-15Re-15Si-10Cr-10W:

**1.** The microconstituents observed in the as-cast structure $Nb_{SS}$, $Cr_2Re_3$, $Nb_5Si_3$, $NbCr_2$. The Pandat$^{TM}$ predicts the formation of $BCC_{SS}$, $Nb_5Si_3$, CrNbSi, and sigma phase. The difference in the microconstituents was observed. For this alloy, $Cr_2Re_3$ provides a very good oxidation resistance up to 1300$^{o}$C.

**2**. The morphology of the phases for oxidized samples from 700 – 1400$^{o}$C does not appear to change drastically. However at 1400, the oxide was complete consumed, leaving no metal. The bulky oxide was analyzed through XRD.

**3.** The oxide converts from orthorhombic to monoclinic at 1000$^{o}$C, depicts monoclinic form of $Nb_2O_5$. $Nb_2WO_5$ and $WO_3$ were also found through the temperature range. The improved oxidation resistance of the alloy can be attributed to the formation of $CrNbO_4$.

4. Mass loss is consistent from 900 – 1200$^{o}$C, and again at 1400$^{o}$, can attributed to the formation of rhenium and chromium volatile oxide (temperature >1000$^{o}$C), and the weight gain at 800, 900, 1300$^{o}$C is due to the formation of $Nb_2O_5$, $Nb_2WO_5$, $CrNbO_4$, $WO_3$, and $SiO_2$. XRD and X- Ray mapping confirm these observations.

5. Improvements were found when compared to the Binary, ternary and quaternary alloys.

### 5.3 Nb-15Re-15Si-10Cr-10B:

**1.** The microconstituents observed in the as-cast structure $Nb_{SS}$, $Nb_5Si_3$, $NbCr_2$ and $Nb_{22}Re_7$. The Pandat$^{TM}$ predicts the formation of $BCC_{SS,}$ $Nb_5Si_{3,}$ CrNbSi, and 932 Silicide. The difference in the microconstituents was observed.

**2**. The morphology of the phases for oxidized samples from 700 – 1400$^{o}$C does not appear to change drastically. However at 1400, the oxide was complete consumed, leaving no metal. The bulky oxide at was analyzed through XRD.

**3.** The oxide converts from tetragonal to monoclinic at 1000$^{o}$C, and remains monoclinic upto 1400$^{o}$C. The improved oxidation resistance of the alloy can be attributed to the formation of $CrNbO_4 + SiO_2$.

4. Mass loss is consistent from 900 – 1400$^{o}$C, can attributed to the formation of rhenium and chromium volatile oxide (temperature >1000$^{o}$C), and the weight gain at 900$^{o}$C is due to the formation of $Nb_2O_{5,}$ $CrNbO_4$ and $SiO_2$. XRD and X- Ray mapping confirm these observations.

5. Improvements were found when compared to the Binary, ternary and quaternary alloys.

## References


1. Perepezko, John H. 2009, Science, Vol. 326, pp. 1068-1069.
2. Bewlay, B. P., et al. 2003, Metal. Mater. Trans. A, Vol. 34A, pp. 2043-2051.
3. Bewlay, B. P., Lewandowski, J. J. and Jackson, M. R. 1997, Journal of Materials, pp. 44-45,67
4. Wahl, G. 4, s.l. : Elsevier B.V., 1983, Thin Sold Films, Vol. 107, pp. 417-426.
5. Wang, Ge, Gleeson, B. and Douglass, D. L. 5/6, 1991, Oxidation of Metals, Vol. 35, pp. 333-348.
6. Wang, Ge, Gleeson, B. and Douglass, D. L. 3/4, 1991, Vol. 35, pp. 317-332.
7. Gesmundo, F. and Gleeson, B. 1/2, 1995, Oxidation of Metals, Vol. 44.
8. B.P. Bewlay, M.R. Jackson, J.C. Zhao, P.R. Subramanian, M.G. Mendiratta, J.J. Lewandowski, *MRS Bulletin*, September 2003, 646-653.
9. B.P. Bewlay, M.R. Jackson, J.C. Zhao, P.R. Subramanian *Metall. Trans. A*, 34A (2003), 2043-2052.
10. P.R. Subramanian, M.G. Mendiratta, D.M. Dimiduk, M.A. Stucke, *Mat. Sci. Eng.*, A239 (1997), 1-13.
11. V. Behrani, A.J. Thom, M. J. Kramer, M. Akinc, *Intermetallics*, 14 (2006), 24-32.
12. J. Geng, P. Tsakiropoulos, *Intermetallics*, 15 (2007), 382-395.
13. B. Bewlay, M. Jackson, H.Lipsitt, , *Metall. Trans* A, 27A (1996), 3801-3808
14. J. Geng, P. Tsakiropoulos, G. Shao,", *Mat. Sci. Eng.*, A441 (2006), 26-38.
15. Jan C Carlen, Elyria, Ohio ,United States patent. Patent No: 5437744. Aug 1, 1995.
16. J. Geng, P. Tsakiropoulos, *Intermetallics*, 15 (2007), 382-395.
17. B. Bewlay, M. Jackson, H. Lipsitt*Metall. Trans* A, 27A (1996), 3801-3808
18. J. Geng, P. Tsakiropoulos, G. Shao,", *Mat. Sci. Eng.*, A441 (2006), 26-38.
19. K.S Chan, *Metall. Mater. Trans. A*, 35A (2004), 589.
20. C.L. Ma, J.G. Li, Y. Tan, R. Tnaka, S. Hanada, , *Mat. Sci. Eng. A*, 384, (2004), 377-384.
21. I. V. Kud', L. I. Eremenko, and L. S. Likhoded Powder Metallurgy and Metal Ceramics, Vol. 43, Nos. 7-8, 2004
22. R.L. Fleischer, R.J. Zabala, Metallurgical Transactions A August 1990, Volume 21, Issue 8, pp 2149-2154
23. R. L. Fleischer and R. J. Zabala:*Metall. Trans*., 1990, vol. 21A, pp. 1951–57
24. R. A. Amato, C. M. Austin, J. C. Chesnutt, R. L. Fleischer, S. C. Huang, M. F. X. Gigliotti, A. M. Johnson, M. Y. Lee, R. G. Rowe, and G. E. Wasielewski: U.S. Air Force Base, Contract No. F33615-86-C-5073, Interim Report No. 1, G. E. Aircraft Engineering Report R-86-AEB-572, Oct. 31, 1986.
25. Behrani, V., et al. 2006, Intermetallics, Vol. 14, pp. 24-32.
26. K. Chattopadhyay, R. Mitra, and K.K. Ray. 2008, Metall. Mater. Trans. A, Vol. 39A, pp. 577-592.
27. Martin, John Wilson. Intermetallics: Laves Phase. s.l. : Elsevier, 2006, pp. 239-246.
28. Kazantzis, A. V., et al. 2007, Acta Materialia, Vol. 55, pp. 1873-1884.
29. Liu, C. T., et al. 2000, Intermetallics, Vol. 8, pp. 1119-1129.
30. Yoshida, M. and Takasugi, T. 1997, Materials Science & Engineering A, Vols. A234-236, pp. 873-876.
31. Zhao, J. C., Jackson, M. R. and Peluso, L. A. 2003, Acta Materialia, Vol. 51, pp. 6395-6405.

32. F. Gesmundo, B. Gleeson, *Oxidation of Metals*, 44 (1/2) (1995), 211-237.
33. E. A. Gulbransen and F. A. Brassart, *J. Less-Common Met*. 14, 217 (1968).
34. D. E. Rosner and H. D. Allendorf, *J. Chem. Phys*. 49, 5553 (1968).
35. Joseph R. Davis, Heat-resistant Materials, ASM International, Jan 1, 1997 - Technology & Engineering
36. C.A. Barrett, J.L. Corey, *NASA Technical Note D-283*, Washington November 1960.
37. S.D. Cramer, B.S. Covino, eds.,*ASM Handbook Vol 13*, (Materials Park, Ohio, 1987), 61.
38. N. Birks, G.H. Meier, F.S. Pettit, 2nd ed, Cambridge University Press, 2006, 98.
39. C.L. Ma, J.G. Li, Y. Tan, R. Tnaka, S. Hanada, *Mat. Sci. Eng. A*, 384, (2004), 377-384
40. A. Misra, (Ph.D. thesis, Northwest University, Evanston Illinois, 2005).
41. T. Hurlen, , *Journal of the Institute of Metals*, 89 (1960-61), 273- 280
42. O. Kubaschewski and B.E. Hopkins, *Journal of Less-Common Metals*, 2 (1960), 172-180
43. G. Brauer, "Die Oxyde des Niobs", *Z. Anorg. Allg. Chem*., 248 (1) (1941).
44. A.U. Seybolt, *Trans. AIME*, 200 (1954), 770.
45. R.T. Bryant, *Journal of Less-Common Metals*, 4 (1) (1962), 62-68.
46. R. P. Elliot, *Trans. Am. Soc. Metals*, 52 (1960), 990.
47. T.P. Hennessey, J.E. Morral, *Oxidation of Metals*, 38 (1) (1992), 163-187.
48. C. K. Gupta, A. K. Suri, CRC Press, 1994, 142.
49. P. Franke, Vol. 19B4. *Landolt-Börnstein-Group IV Physical Chemistry, Chapter Fe-O,* Springer Berlin, Heidelberg, (2006), 1-2.
50. H. Goldschmidt, *J. Inst. Metals*, 87 (1959), 235-239.
51. H. Schäfer, R. Gruehn, F. Schulte, , *Angew.Chem. Int. Edit. Eng.*, 5 (1) (1966), 40-52.
52. N. S. Jacobson, D. L. Myers, D. Zhu, and D. L. Humphrey, *Oxidation of Metals, Vol. 55, Nos. 5/6, 2001*
53. V. O. Lavrenko, *Dopo. Akad. Nauk RSR*, p. 1216 (1958).
54. E. A. Gulbransen and F. A. Brassart, *J. Less-Common Met*. 14, 217 (1968).
55. D. E. Rosner and H. D. Allendorf, *J. Chem. Phys*. 49, 5553 (1968).
56. Earl A. Gulbransen, Fred A. Brassart, Kenneth F. Andrew, Vacuum Microbalance Techniques, 1970, pp 121-133
57. C.A. Barrett, J.L. Corey, *NASA Technical Note D-283*, Washington November 1960.
58. J.F. Stringer, (AGARD-AG200), Advisory Group of Aerospace Research and Development, NATO, August 1975).
59. J. Doychak and M.G Hebsur, *Oxidation of Metals*, 36(1) (1991), 113-141.
60. M.G. Hebsur, J.R. Stephens, J.L. Smialek, C.A. Barrett, D.S. Fox, T. Grobstein and J. Doychak, eds. (TMS, Warrendale, 1989), 171-184.
61. H. J. Grabke, M. Steinhorst, M. Brumm, D. Wiemer, *Oxidation of Metals*, 35 (3/4) (1991), 199-222.
62. A. Misra, (Ph.D. thesis, Northwest University, Evanston Illinois, 2005).
63. Y. Niu, F. Gesmundo, F. Viani, *Oxidation of Metals*, 46 (3/4) (1996), 287-297.
64. M.G. Hebsur, J.R. Stephens, U.S. Patent 4, 983, 358, (Jan 8, 1991).
65. R.A. Rapp, *Metall. Trans. B*, 15B, (1984), 195-212
66. J. Geng, P. Tsakiropoulos, G.Shao, *Intermetallics*, 15, (2007), 270-281.
67. D.M. Dimiduk, M.G. Mendiratta, P.R. Subramanian, *Structural Intermetallics*, 1993, 619-629.
68. E.S.K. Menon, M.G. Mendiratta and D.M. Dimiduk, *Structural Intermetallics*, TMS, The Minerals, Metals and Materials Society (2001), 591

69. T. Murakami, C. Xu, A. Kithara, M. Kawahara, Y. Takahashi, H. Inui, M. Yamaguchi *Intermetallics*, 7 (1999), 1043-1048.
70. B.P. Bewlay, J.J. Lewandowksi, M.R. Jackson, *JOM*, (1997), 44-45
71. Thomas, Kathryn S. and Varma, S. K. 2012, MMTA, March 2014, Vol 45, Issue 3, pp 1124-1135.
72. Benedict Portollio, The University of Texas at El Paso. 2009. PhD Dissertation
73. Y. Liu, M. J. Kramer, A. J. Thom, M. Akinc, Metallurgical and Materials Transactions A, March 2005, Volume 36, Issue 3, pp 601-607
74. Maria del Pilar Moricca, The University of Texas at El Paso. 2009. PhD Dissertation
75. Maria del Pilar Moricca, S.K.Varma, JOM, Volume 60, Issue 7, pp 66-69, July 2008.
76. Accepted: Ruth M. Dasary, S.K, Varma, Ruth M. Dasary, S.K, Varma, Metallography, Microstructure, and Analysis.
77. Ruth Melody Dasary, S.K. Varma, Journal of Materials Research and Technology, Volume 3, Issue 1, January–March 2014, Pages 25–34
78. A.E.Carlsson, Journal of Materials Research / Volume 5 / Issue 12 / 1990, pp 2813-2818

## Curriculum Vita

Ruth M Dasary-Sierra was born in Hyderabad, India. Graduated from Jawaharlal Nehru Technological University with a Bachelors in Technology in 2005. Followed by graduating with M.Phil. with Materials Science major from University of Wales of Swansea. In Fall 2011 she joined the Materials Science and Engineering doctoral program.

While perusing her degree, she worked on research associated with the Office of Naval Research while at the University of Texas at El Paso. Her work was presented in The Minerals, Metals & Materials Society in year 2013 and 2014. Her work was also published in two different journals, titled “Short term Oxidation response of Nb-15Re-15Si-10Cr-20Mo Alloy” and “Short term Oxidation response of Nb-15Re-15Si-20Cr-15Ti Alloy”. During this duration she has also been a Research Assistant and a Teaching Assistant for Dr. Varma.

**Permanent Address:**

351Thunderbird, Apt #12
El Paso TX 79912